

CHEMICAL SYNTHESIS AND ELECTRICAL CHARACTERIZATION
OF N=3 AURIVILLIUS PHASES

BY

STEVEN P. HARVEY

A THESIS
SUBMITTED TO THE FACULTY OF

ALFRED UNIVERSITY

IN PARTIAL FULFILLMENT OF THE REQUIREMENTS
FOR THE DEGREE OF

MASTER OF SCIENCE

IN

CERAMIC ENGINEERING

ALFRED, NEW YORK

FEBRUARY, 2004

Alfred University theses are copyright protected and may be used for education or personal research only. Reproduction or distribution in part or whole is prohibited without written permission from the author.

CHEMICAL SYNTHESIS AND ELECTRICAL CHARACTERIZATION
OF N=3 AURIVILLIUS PHASES

BY

STEVEN P. HARVEY

B.S. ALFRED UNIVERSITY (2002)

SIGNATURE OF AUTHOR _____ (Signature on file)

APPROVED BY _____ (Signature on file)
SCOTT MISTURE, ADVISOR

STEVE M. PILGRIM, ADVISORY COMMITTEE

DOREEN EDWARDS, ADVISORY COMMITTEE

MATTHEW HALL, CHAIR, ORAL THESIS DEFENSE

ACCEPTED BY _____ (Signature on file)
ALASTAIR CORMACK, DEAN,
SCHOOL OF ENGINEERING

ACKNOWLEDGEMENTS

I would like to thank Dr. Misture for all his help and guidance, not only during this project, but during my undergraduate career as well. Thanks to my committee members Dr. Edwards and Pilgrim for their assistance throughout my degree. Thanks to Swavek Zdzieszynski for keeping all of the instruments in tip top shape, without you around this lab would not be the same. Thanks to Fran Williams for all his help with the electrical characterization equipment. I would like to thank the x-ray gang, who were always willing to share their knowledge, which made my transition into graduate school much easier. I would also like to thank Dr. Weitung Wang and all my associates at Praxair Inc, where I first learned the excitement of working in a laboratory, and the doors that are opened to you when you pursue an advanced degree.

Thanks to Dr. Mike Haluska for teaching me how to be my own mechanic, and for being an unspoken mentor during my tenure here. Thanks to Brian Luisi for getting me into the sport of triathlon, and the x-ray guys for introducing me to cycling. Thanks to Dr. Michael Dolan for all the good times cycling the southern tier together this summer. Thanks to Justin for being such a good roommate and thanks to Nate for giving me a place to stay this past month.

I would like to thank my parents for always encouraging me and being supportive of anything that I do. Because of you I know the value of hard work, and without your guidance and encouragement I would not be half the person I am today. Anne, thanks for being my biggest supporter and biggest fan the last six years. Without you I would not be the confident, successful, and happy person that I am today.

TABLE OF CONTENTS

	Page
Acknowledgements.....	iii
List of Tables	vii
List of Figures.....	viii
Abstract.....	xiv
1 Introduction	1
1.1 Solid Oxide Fuel Cells	1
1.1.1 A Typical SOFC	1
1.2 Aurivillius Materials	2
1.3 Impedance Spectroscopy.....	4
1.3.1 Experimental Aspects of Impedance.....	6
1.3.2 Impedance of Ceramics.....	6
1.4 Ionic Conductivity.....	8
1.4.1 Ionic Conductivity in Ceramics	10
1.5 Polymerized Complex Synthesis	12
2 Experimental Procedure	14
2.1.1 Compositions Attempted and Strategy.....	14
2.1.2 Synthesis	17
2.1.3 Density Measurements.....	19
2.1.4 Phase Analysis Via X-ray Diffraction.....	19
2.1.5 Use of Jade 6.0 for XRD Analysis	20
2.1.6 Scanning Electron Microscopy	20
2.1.7 Electrical Characterization	21
2.1.7.1 Impedance Spectroscopy	21
2.1.7.2 Controlled Atmosphere DC Conductivity	21
3 Results and Discussion.....	22
3.1 Characterization of $\text{Bi}_2\text{Sr}_2\text{Nb}_2\text{TiO}_{12}$	22
3.1.1 Synthesis of $\text{Bi}_2\text{Sr}_2\text{Nb}_2\text{TiO}_{12}$	22
3.1.2 Electrical Characterization of $\text{Bi}_2\text{Sr}_2\text{Nb}_2\text{TiO}_{12}$	22
3.1.3 Microstructure of $\text{Bi}_2\text{Sr}_2\text{Nb}_2\text{TiO}_{12}$	24

3.1.4	Sintering and Density of $\text{Bi}_2\text{Sr}_2\text{Nb}_2\text{TiO}_{12}$	25
3.2	Characterization of $\text{Bi}_2\text{Sr}_2\text{Nb}_2\text{Ti}_{(1-x)}\text{M}_x\text{O}_{12-\delta}$ ($x=0-1$, $M=\text{Co, Cr, Fe, Mn}$).....	28
3.2.1	Synthesis of $\text{Bi}_2\text{Sr}_2\text{Nb}_2\text{Ti}_{(1-x)}\text{M}_x\text{O}_{12-\delta}$	28
3.2.2	X-Ray Diffraction of $\text{Bi}_2\text{Sr}_2\text{Nb}_2\text{Ti}_{(1-x)}\text{M}_x\text{O}_{12-\delta}$	30
3.2.3	Electrical Characterization of $\text{Bi}_2\text{Sr}_2\text{Nb}_2\text{Ti}_{(1-x)}\text{M}_x\text{O}_{12-\delta}$ ($x=0-1$, $M=\text{Co, Cr, Fe}$).....	37
3.2.3.1	AC Conductivity of $\text{Bi}_2\text{Sr}_2\text{Nb}_2\text{Ti}_{(1-x)}\text{Fe}_x\text{O}_{12-\delta}$	37
3.2.3.2	AC Conductivity of $\text{Bi}_2\text{Sr}_2\text{Nb}_2\text{Ti}_{(1-x)}\text{Cr}_x\text{O}_{12-\delta}$	40
3.2.3.3	AC Conductivity of $\text{Bi}_2\text{Sr}_2\text{Nb}_2\text{Ti}_{0.95}\text{Co}_{0.05}\text{O}_{12-\delta}$	41
3.2.4	Microstructural characterization of $\text{Bi}_2\text{Sr}_2\text{Nb}_2\text{Ti}_{(1-x)}\text{M}_x\text{O}_{12-\delta}$ ($M=\text{Fe, Cr}$).....	43
3.2.4.1	Microstructure of $\text{Bi}_2\text{Sr}_2\text{Nb}_2\text{Ti}_{0.95}\text{Fe}_{0.05}\text{O}_{12-\delta}$	45
3.2.4.2	Microstructure of $\text{Bi}_2\text{Sr}_2\text{Nb}_2\text{Ti}_{0.50}\text{Fe}_{0.50}\text{O}_{12-\delta}$	47
3.2.4.3	Microstructure of $\text{Bi}_2\text{Sr}_2\text{Nb}_2\text{Ti}_{0.8}\text{Cr}_{0.2}\text{O}_{12-\delta}$	47
3.3	Characterization of $\text{Bi}_2\text{Sr}_{(2-x)}\text{Fe}_x\text{Nb}_2\text{Ti}_{0.5}\text{Fe}_{0.5}\text{O}_{12-\delta}$ ($x=0.5, 1$).....	50
3.4	Characterization of $\text{Bi}_{(2-y)}\text{Pb}_y\text{Nb}_2\text{Ti}_{(1-z)}\text{Al}_z\text{O}_{12-\delta}$ ($y=0-1.2$, $z=0.2, 0.25, 1$).....	51
3.4.1	Synthesis of $\text{Bi}_{(2-y)}\text{Pb}_y\text{Sr}_2\text{Nb}_2\text{Ti}_{(1-z)}\text{Al}_z\text{O}_{12-\delta}$ ($y=0-1.2$).....	51
3.4.2	X-ray diffraction of $\text{Bi}_{(2-y)}\text{Pb}_y\text{Sr}_2\text{Nb}_2\text{TiO}_{12-\delta}$ ($y=0-1$).....	52
3.4.2.1	Anomalous Diffraction Behavior in $\text{Bi}_{(2-y)}\text{Pb}_y\text{Sr}_2\text{Nb}_2\text{TiO}_{12-\delta}$ ($y=0-1$).....	54
3.4.2.2	Stacking Faults in Layered Structures.....	54
3.4.2.3	Williamson-Hall plots.....	55
3.4.2.4	Separating Size and Strain Effects.....	56
3.4.2.5	Crystallite Size Effect.....	60
3.4.3	Possible Impurity Phase in $\text{Bi}_{(2-y)}\text{Pb}_y\text{Sr}_2\text{Nb}_2\text{TiO}_{12-\delta}$ ($y=0.4-1$).....	63
3.4.4	Microstructure of $\text{Bi}_{(2-y)}\text{Pb}_y\text{Sr}_2\text{Nb}_2\text{TiO}_{12-\delta}$ ($y=0-1$).....	65
3.4.5	AC Conductivity of $\text{Bi}_{(2-y)}\text{Pb}_y\text{Sr}_2\text{Nb}_2\text{TiO}_{12-\delta}$ ($y=0-1$).....	69
3.4.6	X-ray Diffraction of $\text{Bi}_{0.8}\text{Pb}_{1.2}\text{Sr}_2\text{Nb}_2\text{TiO}_{12-\delta}$	72
3.4.7	Synthesis of $\text{Bi}_{(2-y)}\text{Pb}_y\text{Sr}_2\text{Nb}_2\text{Ti}_{(1-z)}\text{Al}_z\text{O}_{12-\delta}$ ($y=0.4$, $z=0.02, 0.25, 1$).....	73
3.4.7.1	X-ray Diffraction of $\text{Bi}_{(2-y)}\text{Pb}_y\text{Sr}_2\text{Nb}_2\text{Ti}_{(1-z)}\text{Al}_z\text{O}_{12-\delta}$ ($y=0.4$, $z=0.025, 0.4, 1$).....	74
3.4.7.2	AC Conductivity of $\text{Bi}_{1.6}\text{Pb}_{0.4}\text{Sr}_2\text{Nb}_2\text{Ti}_{0.8}\text{Al}_{0.2}\text{O}_{12-\delta}$	76
3.5	Controlled Atmosphere Conductivity.....	78
3.5.1	$\text{Bi}_2\text{Sr}_2\text{Nb}_2\text{TiO}_{12}$	78
3.5.2	$\text{Bi}_2\text{Sr}_2\text{Nb}_2\text{Ti}_{0.8}\text{Fe}_{0.2}\text{O}_{12-\delta}$	81
4	Summary and Conclusions.....	84
5	Future Work.....	86

References.....	87
Appendix.....	93

LIST OF TABLES

	Page
Table I: List of Compositions Whose Synthesis was Attempted.	15
Table II: Ionic Radii of Transition Metals Substituted for Titanium.....	16
Table III: List of Polymerized Complex Precursor Materials.....	18
Table IV: Batch Constituents for a four gram batch of $\text{Bi}_{1.9}\text{Pb}_{0.1}\text{Sr}_2\text{Nb}_2\text{TiO}_{12-\delta}$	19
Table V: Phase Purity Results Obtained for Transition Metal Series.....	29
Table VI: Conductivity and Activation Energies for $\text{Bi}_2\text{Sr}_2\text{Nb}_2\text{Ti}_{(1-x)}\text{Fe}_x\text{O}_{12-\delta}$	38
Table VII: Conductivity and Activation Energies for $\text{Bi}_2\text{Sr}_2\text{Nb}_2\text{Ti}_{(1-x)}\text{Cr}_x\text{O}_{12-\delta}$	40
Table VIII: Conductivity and Activation Energies for $\text{Bi}_2\text{Sr}_2\text{Nb}_2\text{Ti}_{0.95}\text{Co}_{0.05}\text{O}_{12-\delta}$	42
Table IX: Phase Purity Results Obtained for Lead Substitution Series.	52
Table X: Conductivity Data for $\text{Bi}_{(2-y)}\text{Pb}_y\text{Sr}_2\text{Nb}_2\text{TiO}_{12-\delta}$ ($y=0-1$).....	69
Table XI: Phase Purity Results for Lead and Aluminum Substitution	74
Table XII: Conductivity Data for $\text{Bi}_{1.6}\text{Pb}_{0.4}\text{Sr}_2\text{Nb}_2\text{Ti}_{0.8}\text{Al}_{0.2}\text{O}_{12-\delta}$ and Similar Samples.....	76

LIST OF FIGURES

	Page
Figure 1.1. Schematic diagram of an SOFC and the typical composition of each major component.	1
Figure 1.2. Schematic representations of the (a) $n=2$ (b) $n=3$ (c) $n=4$ Aurivillius materials. (From Reference 23).	3
Figure 1.3. Impedance response showing real and imaginary components.....	5
Figure 1.4. Possible impedance response plot of a polycrystalline ceramic and the corresponding RC equivalent circuit.....	7
Figure 1.5. Arrhenius conductivity plot exhibiting single and dual activation energy materials.	10
Figure 1.6. Graphical illustration of activation energy required for conduction.	11
Figure 1.7. Graphical illustration of varying potential energy along the oxygen diffusion path (diffusion path is considered left to right on the page).	11
Figure 1.8. Flow chart for the polymerized complex synthesis method. (From Reference 45).	13
Figure 3.1. XRD patterns for $\text{Bi}_2\text{Sr}_2\text{Nb}_2\text{TiO}_{12}$ after calcination ($900^\circ\text{C}/10\text{hrs}$) and sintering ($1050^\circ\text{C}/30\text{hrs}$). The sticks in the bottom of the figure represent the peak placement of the corresponding PDF cards.	22
Figure 3.2. Typical Cole-Cole plot of $\text{Bi}_2\text{Sr}_2\text{Nb}_2\text{TiO}_{12}$ (600°C).	23
Figure 3.3. Conductivity of $\text{Bi}_2\text{Sr}_2\text{Nb}_2\text{TiO}_{12}$ from 2-point AC impedance spectroscopy.	24
Figure 3.4. SEM images of $\text{Bi}_2\text{Sr}_2\text{Nb}_2\text{TiO}_{12}$ pellet face polished to 1000grit A, C are SE images, and B, D are the corresponding BSE images.....	25
Figure 3.5. SEM micrographs of $\text{Bi}_2\text{Sr}_2\text{Nb}_2\text{TiO}_{12}$, polished face of hot pressed sample A) SE image B) SE image of cracking caused by hot pressing C) SE image D) BSE image of image C.....	27
Figure 3.6. SEM micrographs of $\text{Bi}_2\text{Sr}_2\text{Nb}_2\text{TiO}_{12}$ fractured face of hot pressed sample. Both images are SE images.	28

Figure 3.7. XRD pattern for $\text{Bi}_2\text{Sr}_2\text{Nb}_2\text{Ti}_{(1-x)}\text{Fe}_x\text{O}_{12}$ series post $900^\circ\text{C}/10\text{hrs}$, i A) $x=0.05$, B) $x=0.1$, C) $x=0.2$, D) $x=0.5$. The sticks in the bottom of the figure represent the peak placement of the corresponding PDF cards.....	31
Figure 3.8. XRD pattern for $\text{Bi}_2\text{Sr}_2\text{Nb}_2\text{Ti}_{(1-x)}\text{Fe}_x\text{O}_{12}$ post $1050^\circ\text{C}/30\text{hrs}$, A) $x=0.05$, B) $x=0.1$, C) $x=0.2$, D) $x=0.5$. The sticks in the bottom of the figure represent the peak placement of the corresponding PDF cards.....	31
Figure 3.9. XRD patterns for $\text{Bi}_2\text{Sr}_2\text{Nb}_2\text{Ti}_{0.25}\text{Fe}_{0.75}\text{O}_{12-\delta}$ post $900^\circ\text{C}/10\text{hrs}$ and $1050^\circ\text{C}/30\text{hrs}$. The sticks in the bottom of the figure represent the peak placement of the corresponding PDF cards.....	32
Figure 3.10. XRD patterns for $\text{Bi}_2\text{Sr}_2\text{Nb}_2\text{FeO}_{11.5}$ post $900^\circ\text{C}/10\text{hrs}$ and $1050^\circ\text{C}/30\text{hrs}$. The sticks in the bottom of the figure represent the peak placement of the corresponding PDF cards.....	33
Figure 3.11. XRD patterns for $\text{Bi}_2\text{Sr}_2\text{Nb}_2\text{Ti}_{(1-x)}\text{Cr}_x\text{O}_{12-\delta}$ post $900^\circ\text{C}/10\text{hrs}$ A) $x=0.05$, B) $x=0.1$, C) $x=0.2$. The sticks in the bottom of the figure represent the peak placement of the corresponding PDF cards.....	33
Figure 3.12. XRD patterns for $\text{Bi}_2\text{Sr}_2\text{Nb}_2\text{Ti}_{(1-x)}\text{Cr}_x\text{O}_{12-\delta}$ post $1050^\circ\text{C}/30\text{hrs}$ the amorphous hump seen below $10^\circ 2\theta$ is from the sample holder. A) $x=0.05$, B) $x=0.1$, C) $x=0.2$. The sticks in the bottom of the figure represent the peak placement of the corresponding PDF cards.....	34
Figure 3.13. XRD pattern for $\text{Bi}_2\text{Sr}_2\text{Nb}_2\text{Ti}_{0.5}\text{Cr}_{0.5}\text{O}_{11.75}$ post $900^\circ\text{C}/10\text{hrs}$. The sticks in the bottom of the figure represent the peak placement of the corresponding PDF cards.....	35
Figure 3.14. XRD patterns for $\text{Bi}_2\text{Sr}_2\text{Nb}_2\text{Ti}_{0.95}\text{Co}_{0.05}\text{O}_{11.975}$ post calcination and sintering. The sticks in the bottom of the figure represent the peak placement of the corresponding PDF cards.....	35
Figure 3.15. XRD pattern for $\text{Bi}_2\text{Sr}_2\text{Nb}_2\text{Ti}_{0.8}\text{Co}_{0.2}\text{O}_{11.9}$ post calcination and sintering. The sticks in the bottom of the figure represent the peak placement of the corresponding PDF cards.....	36
Figure 3.16. XRD pattern for $\text{Bi}_2\text{Sr}_2\text{Nb}_2\text{MnO}_{11.5}$ post $900/10\text{hrs}$. The sticks in the bottom of the figure represent the peak placement of the corresponding PDF cards.....	37
Figure 3.17. Conductivity data for from $\text{Bi}_2\text{Sr}_2\text{Nb}_2\text{Ti}_{(1-x)}\text{Fe}_x\text{O}_{12-\delta}$ $200\text{-}1000^\circ\text{C}$	38
Figure 3.18. Cole-Cole plots for $\text{Bi}_2\text{Sr}_2\text{Nb}_2\text{Ti}_{(1-x)}\text{Fe}_x\text{O}_{12-\delta}$, at 600°C , with iron substitution levels listed in the plot window.....	39

Figure 3.19. Conductivity data for $\text{Bi}_2\text{Sr}_2\text{Nb}_2\text{Ti}_{(1-x)}\text{Cr}_x\text{O}_{12-\delta}$ from 200-1000°C.....	41
Figure 3.20. Conductivity for $\text{Bi}_2\text{Sr}_2\text{Nb}_2\text{Ti}_{0.95}\text{Co}_{0.05}\text{O}_{12-\delta}$ from 200-1000°C.	42
Figure 3.21. Percent of theoretical density of conductivity disks from series $\text{Bi}_2\text{Sr}_2\text{Nb}_2\text{Ti}_{(1-x)}\text{Fe}_x\text{O}_{12-\delta}$ ($x=0, 0.5, 0.1, 0.2, 0.5$) as a function of added iron. The data has been fit to a Spline curve.	44
Figure 3.22. SE SEM images for both A) $\text{Bi}_2\text{Sr}_2\text{Nb}_2\text{Ti}_{0.80}\text{Fe}_{0.20}\text{O}_{12-\delta}$ and B) $\text{Bi}_2\text{Sr}_2\text{Nb}_2\text{Ti}_{0.50}\text{Fe}_{0.50}\text{O}_{12-\delta}$	44
Figure 3.23. SEM images of $\text{Bi}_2\text{Sr}_2\text{Nb}_2\text{Ti}_{0.95}\text{Fe}_{0.05}\text{O}_{11.975}$ A and C are SE images; B and D are the corresponding BSE images.	46
Figure 3.26. SEM images of $\text{Bi}_2\text{Sr}_2\text{Nb}_2\text{Ti}_{0.50}\text{Fe}_{0.50}\text{O}_{12-\delta}$ A and C are SE images; B and D are BSE images.....	47
Figure 3.27. Percent of theoretical density of conductivity disks from series $\text{Bi}_2\text{Sr}_2\text{Nb}_2\text{Ti}_{(1-x)}\text{Cr}_x\text{O}_{12-\delta}$ ($x=0,0.5,0.1,0.2$). The data is fit with a spline curve.	48
Figure 3.28. SEM images of $\text{Bi}_2\text{Sr}_2\text{Nb}_2\text{Ti}_{0.8}\text{Cr}_{0.2}\text{O}_{12-\delta}$ A,B, C,E are SE images, D and F are BSE images of C and D, respectively.	49
Figure 3.29. XRD pattern of $\text{Bi}_2\text{Sr}_{1.5}\text{Fe}_{0.5}\text{Nb}_2\text{Ti}_{0.50}\text{Fe}_{0.50}\text{O}_{12-\delta}$ post 900/10hrs. The sticks in the bottom of the figure represent the peak placement of the corresponding PDF cards.....	50
Figure 3.30. XRD pattern of $\text{Bi}_2\text{Sr}_1\text{Fe}_1\text{Nb}_2\text{Ti}_{0.50}\text{Fe}_{0.50}\text{O}_{12-\delta}$ post 900/10hrs. The sticks in the bottom of the figure represent the peak placement of the corresponding PDF cards.	51
Figure 3.31. XRD patterns of $\text{Bi}_{(2-y)}\text{Pb}_y\text{Sr}_2\text{Nb}_2\text{TiO}_{12-\delta}$ post 900/10hours calcination A) $Y=0.1$ B) $Y=0.2$, C) $Y=0.3$, D) $Y=0.4$, E) $Y=0.5$, F) $Y=0.6$, G) $Y=1$	53
Figure 3.32. XRD patterns of $\text{Bi}_{(2-y)}\text{Pb}_y\text{Sr}_2\text{Nb}_2\text{TiO}_{12-\delta}$ ($Y=0-1$) pellet faces post 1050/30hrs sintering A) $Y=0.2$ B) $Y=0.3$, C) $Y=0.4$, D) $Y=0.5$, E) $Y=0.6$, F) $Y=1$. The hump below $15^\circ 2\theta$ is from the sample holder.	53
Figure 3.33. Example of a Williamson-Hall plot.....	55
Figure 3.34. Williamson-Hall plot of $\text{Bi}_{1.8}\text{Pb}_{0.2}\text{Sr}_2\text{Nb}_2\text{TiO}_{12-\delta}$ post 900°C/10hrs. The data is representative of Williamson-Hall plots of the entire lead series.....	56

Figure 3.35. Full-width and half maximum plotted against a crystallite size correlation.	57
Figure 3.36. Full-width and half maximum plotted against a crystallite strain correlation.	58
Figure 3.37. Crystallite size of $\text{Bi}_{(2-y)}\text{Pb}_y\text{Sr}_2\text{Nb}_2\text{TiO}_{12-\delta}$ ($y=0-1$) calculated from Scherrer equation.	59
Figure 3.38. Crystallite strain of $\text{Bi}_{(2-y)}\text{Pb}_y\text{Sr}_2\text{Nb}_2\text{TiO}_{12-\delta}$ ($y=0-1$).	59
Figure 3.39. Secondary electron SEM images of calcined powder. A and B show platelet nature of particles, A shows square-like nature, an indication of growth along the a-b plane.	61
Figure 3.40. Secondary electron SEM images of calcined powder A) particle platelet of damaged square B) Close up of A C) close up of the particle labeled 1 in B, notice the square nature D) close up of the particle labeled 2 in B.	62
Figure 3.41. All images are secondary electron images of sintered pellets micrograph A is $\text{Bi}_{1.6}\text{Pb}_{0.4}\text{Sr}_2\text{Nb}_2\text{TiO}_{12-\delta}$, B is $\text{Bi}_{1.7}\text{Pb}_{0.3}\text{Sr}_2\text{Nb}_2\text{TiO}_{12-\delta}$, C is $\text{BiPbSr}_2\text{Nb}_2\text{TiO}_{12-\delta}$, and D is $\text{Bi}_{1.4}\text{Pb}_{0.6}\text{Sr}_2\text{Nb}_2\text{TiO}_{12-\delta}$	63
Figure 3.42. XRD patterns for $\text{Bi}_{(2-y)}\text{Pb}_y\text{Sr}_2\text{Nb}_2\text{TiO}_{12-\delta}$ showing possible impurity phase appearing at lead concentrations of $y=0.4$ and higher. A) $\text{Bi}_{1.7}\text{Pb}_{0.3}\text{Sr}_2\text{Nb}_2\text{TiO}_{12-\delta}$ B) $\text{Bi}_{1.6}\text{Pb}_{0.4}\text{Sr}_2\text{Nb}_2\text{TiO}_{12-\delta}$ C) $\text{Bi}_{1.5}\text{Pb}_{0.5}\text{Sr}_2\text{Nb}_2\text{TiO}_{12-\delta}$ D) $\text{Bi}_{1.4}\text{Pb}_{0.6}\text{Sr}_2\text{Nb}_2\text{TiO}_{12-\delta}$ E) $\text{BiPbSr}_2\text{Nb}_2\text{TiO}_{12-\delta}$. All patterns are for calcined powder ($900^\circ\text{C}/10\text{hrs}$). The sticks in the bottom of the figure represent the peak placement of the corresponding PDF cards.	64
Figure 3.43. SEM images of $\text{Bi}_{1.7}\text{Pb}_{0.3}\text{Sr}_2\text{Nb}_2\text{TiO}_{12-\delta}$ after sintering at $1050^\circ\text{C}/30\text{hrs}$. A and B are SE images, C is a BSE image of the same area as B.	66
Figure 3.44. SEM images of $\text{Bi}_{1.6}\text{Pb}_{0.4}\text{Sr}_2\text{Nb}_2\text{TiO}_{12-\delta}$ C, E are BSE images of B,D.	67
Figure 3.45. SEM images of $\text{BiPbSr}_2\text{Nb}_2\text{TiO}_{12-\delta}$ A, B,C, and E are SE images, D and F are the BSE images of C and F, respectively.	68
Figure 3.46. Cole-Cole plots for several compositions within lead series $\text{Bi}_{(2-y)}\text{Pb}_y\text{Sr}_2\text{Nb}_2\text{TiO}_{12-\delta}$ at 600°C	70
Figure 3.47. Conductivity of $\text{Bi}_{(2-y)}\text{Pb}_y\text{Sr}_2\text{Nb}_2\text{TiO}_{12-\delta}$ ($y=0-1$) from AC impedance.	71

Figure 3.48. XRD patterns for $\text{Bi}_{0.8}\text{Pb}_{1.2}\text{Sr}_2\text{Nb}_2\text{TiO}_{12-\delta}$ after calcination and sintering. The sticks in the bottom of the figure represent the peak placement of the corresponding PDF cards.	73
Figure 3.49. XRD patterns for $\text{Bi}_{1.6}\text{Pb}_{0.4}\text{Sr}_2\text{Nb}_2\text{Ti}_{0.8}\text{Al}_{0.2}\text{O}_{12-\delta}$ after calcination and sintering. The sticks in the bottom of the figure represent the peak placement of the corresponding PDF cards.	74
Figure 3.50. XRD pattern for $\text{Bi}_2\text{Sr}_2\text{Nb}_2\text{Ti}_{0.75}\text{Al}_{0.25}\text{O}_{12-\delta}$ after calcination at $900^\circ\text{C}/10\text{hrs}$. The sticks in the bottom of the figure represent the peak placement of the corresponding PDF cards.	75
Figure 3.51. XRD patterns for $\text{Bi}_2\text{Sr}_2\text{Nb}_2\text{AlO}_{12-\delta}$ after calcination and sintering. The sticks in the bottom of the figure represent the peak placement of the corresponding PDF cards.	75
Figure 3.52. AC conductivity for $\text{Bi}_{1.6}\text{Pb}_{0.4}\text{Sr}_2\text{Nb}_2\text{Ti}_{0.8}\text{Al}_{0.2}\text{O}_{12-\delta}$ and related unsubstituted and Pb,Al substituted compositions. The error is approximately 10%.	77
Figure 3.53. Controlled atmosphere 4-point DC conductivity of $\text{Bi}_2\text{Sr}_2\text{Nb}_2\text{TiO}_{12}$ up to 800°C . The open triangles are for oxygen atmosphere, the closed triangles are for air atmosphere, open circles are for 1% oxygen atmosphere, and closed circles are for argon atmosphere.	79
Figure 3.54. Log conductivity (measured using 4 point DC) vs. log PO_2 for $\text{Bi}_2\text{Sr}_2\text{Nb}_2\text{TiO}_{12}$ at 800°C . The dotted line represents a slope of $-1/4$	80
Figure 3.55. Controlled atmosphere conductivity of $\text{Bi}_2\text{Sr}_2\text{Nb}_2\text{Ti}_{0.8}\text{Fe}_{0.2}\text{O}_{12}$ up to 800°C . The closed circles are for oxygen atmosphere, the open circles are for air atmosphere, closed triangles are for 1% oxygen atmosphere, and closed diamonds are for argon atmosphere. All measurements from 4 point DC conductivity.	82
Figure 3.56. Log conductivity vs log PO_2 for $\text{Bi}_2\text{Sr}_2\text{Nb}_2\text{Ti}_{0.8}\text{Fe}_{0.2}\text{O}_{12}$ at 800°C measured using 4 point DC conductivity.	83
Figure 5.1. TEM image of $\text{BiPbSr}_2\text{Nb}_2\text{TiO}_{12-\delta}$ calcined powder. The EDS spectrum of the particle marked with the \$ sign is presented in Figure 5.2. The clear material is the membrane coating.	94
Figure 5.2. EDS spectrum of particle indicated in Figure 5.1 with the dollar-sign. All of the constituents are present, and copper is present from the TEM grid supporting the particles.	95
Figure 5.3 TEM images of $\text{BiPbSr}_2\text{Nb}_2\text{TiO}_{12-\delta}$ A) bright field image at x120k, and B) is the diffraction pattern for the particle marked with the \$ sign in A.	96

Figure 5.4. TEM image of TEM image of $\text{BiPbSr}_2\text{Nb}_2\text{TiO}_{12-\delta}$ calcined powder, the grains A and B are identified for the EDS analysis presented in Figure 5.4. 97

Figure 5.5. EDS spectra of $\text{BiPbSr}_2\text{Nb}_2\text{TiO}_{12-\delta}$ shown in Figure 5.4. The bottom pattern is from grain marked A in Figure 5.4 and the top pattern is for grain marked B in Figure 5.4. Notice slightly different lead to bismuth ratios for the grains. 98

ABSTRACT

The polymerized complex method was utilized to synthesize $n=3$ Aurivillius compounds based on the parent phase $\text{Bi}_2\text{Sr}_2\text{Nb}_2\text{TiO}_{12}$. Results show that this is a viable option to replace solid-state synthesis of these materials because of the good homogeneity of powders and the substantially shorter processing times. The Aurivillius materials studied cannot be prepared to high density without the assistance of hot pressing. Compounds substituting transition metals (Fe, Cr, Co) for titanium remained phase pure up to 50 atom% (dependent on the valence and cation size as expected). Samples prepared substituting lead for bismuth were clearly phase pure up to 15 atom%, and in the 15-50 atom% substitution range XRD patterns indicate that a lead oxide or bismuth oxide impurity phase may be present; however, these impurity phases were not visible in the SEM. Transition metal substitutions did not increase the electrical conductivity of the material, and lead substitutions in high concentration decreased the conductivity. The substitutions did not affect the shape of Cole-Cole impedance plots. An anomalous diffraction behavior was observed in the lead substituted series. Peaks mixed indices peaks having c-axis character broadened as the lead concentration increased. This could correspond to a crystallite size or stain effect; however, attempts to separate the two using XRD analysis were unsuccessful. The charge carrier was studied under four different atmospheres, ranging from pure oxygen to 500ppm of oxygen. The data indicated that the parent phase $\text{Bi}_2\text{Sr}_2\text{Nb}_2\text{TiO}_{12}$ is an electronic conductor. Results for the transition metal substituted sample $\text{Bi}_2\text{Sr}_2\text{Nb}_2\text{Ti}_{0.8}\text{Fe}_{0.2}\text{O}_{12}$ indicate the sample is an ionic conductor. The stability of the Aurivillius phase under reducing conditions at 1050°C was determined: at a PO_2 of 10^{-3} atm a bismuth oxide impurity phase (if present) decomposes and the Aurivillius phase is stable for 30 hours. At a PO_2 of 10^{-8} atm the Aurivillius phase starts to break down after just 10hrs. At a PO_2 of 10^{-12} atm the Aurivillius phase completely breaks down after 10 hours.

1 INTRODUCTION

1.1 Solid Oxide Fuel Cells

The way in which the world gets energy is changing. Fossil fuel supplies are not unlimited, and deriving electrical energy from fossil fuels is typically inefficient and highly polluting. Because of this an emphasis has been placed on finding new, clean and renewable energy sources. One possible alternative to fossil fuels are solid oxide fuel cells (SOFCs). If fully developed SOFCs can offer an efficient, low pollution energy source for the world of tomorrow.¹⁻³

1.1.1 A Typical SOFC

A typical SOFC consists of the following components: anode, electrolyte, and a cathode. The anode is typically the support mechanism for a thin (10-100 μ m) electrolyte layer. A schematic representation of an SOFC is presented in Figure 1.1, which also presents some current standards of the SOFC components.^{2,4,5}

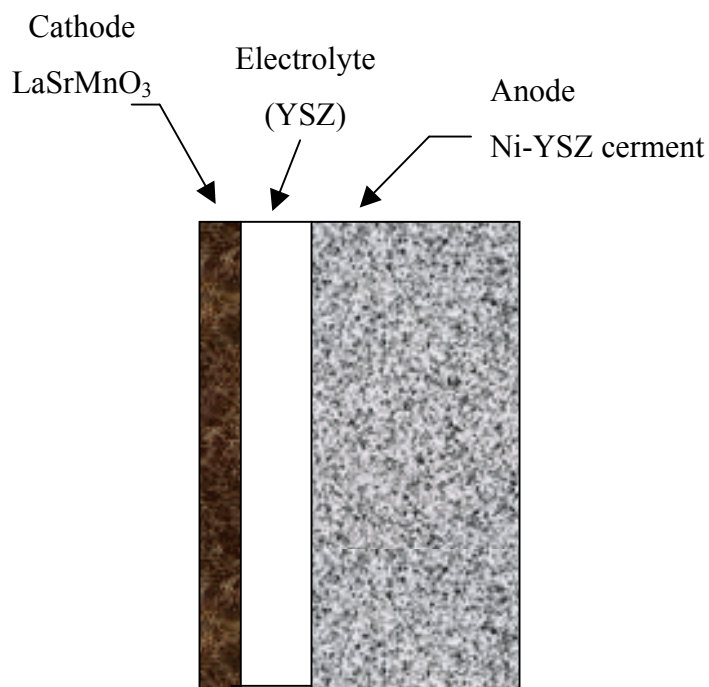


Figure 1.1. Schematic diagram of an SOFC and the typical composition of each major component.

The component of the SOFC that is of interest to this work is the electrolyte. The electrolyte is an oxygen ion conductor, which provides the means for the SOFC to produce electricity. This occurs as oxygen ions are formed at the cathode-electrolyte interface, travel through the electrolyte and form electrons as they recombine with the surrounding atmosphere.

The current standard electrolyte is yttria-stabilized zirconia (YSZ), which has a conductivity of 10^{-1} ($\text{S}\cdot\text{cm}^{-1}$) at 800°C .^{6,7} The current limitation of SOFCs is that conduction within the electrolyte is a thermally activated process. This necessitates high operation temperatures when a YSZ electrolyte is utilized. Consequently significant interest exists for finding an alternative SOFC electrolyte. A new electrolyte needs to operate at lower temperatures without a loss of performance (i.e. higher conductivity at lower temperatures) in order to replace YSZ. Investigating of a possible new electrolyte materials is the goal of this research^{4,5}

1.2 Aurivillius Materials

Aurivillius materials are being investigated for possible use as fuel cell electrolytes because of work done in the mid 1990's by Kendall,⁸⁻¹¹ that showed very high conductivities of several Aurivillius compositions. Therefore, it was concluded that Aurivillius materials were a viable option for an SOFC electrolyte material, meriting further study. This study consists of investigating Aurivillius materials for SOFC applications; however, Aurivillius materials have been heavily investigated for their ferroelectric properties as well. .¹²⁻²¹

Aurivillius phases are comprised of a layered framework of a general composition $\text{Bi}_2\text{A}_{n-1}\text{B}_n\text{O}_{3n+3}$ which is best described as an alternating sequence of puckered $(\text{Bi}_2\text{O}_2)^{2-}$ sheets separated by perovskite blocks of the general composition $(\text{A}_{n-1}\text{B}_n\text{O}_{3n+1})$.^{14,22,23} A is a large atom with 12-fold coordination ($\text{A} = \text{Ba}, \text{Sr}, \text{Ca}, \text{Bi}, \text{Pb}$) and B is a smaller atom with 6-fold coordination ($\text{B} = \text{Ti}, \text{Nb}, \text{Ta}, \text{Mo}, \text{W}, \text{Fe}, \text{Ga}, \text{Al}$).^{10,24-26} The number of perovskite layers (referred to as “ n ”) between the $(\text{Bi}_2\text{O}_2)^{2-}$ sheets is a means of classifying the Aurivillius structures, which can vary from $n=1$ to $n=5$.²⁷ The original work on these materials was completed by Bengt Aurivillius who characterized the $n=2,3$, and 4 phases $\text{CaNb}_2\text{Bi}_2\text{O}_9$, $\text{Bi}_4\text{Ti}_3\text{O}_{12}$ and $\text{BaBi}_4\text{Ti}_4\text{O}_{15}$,

respectively.²⁸⁻³⁰ Later work explored the $n=1$ and $n=5$ structures as well.^{9,13} Figure 1.2 shows the structure of the $n=2, 3,$ and 4 Aurivillius phases.

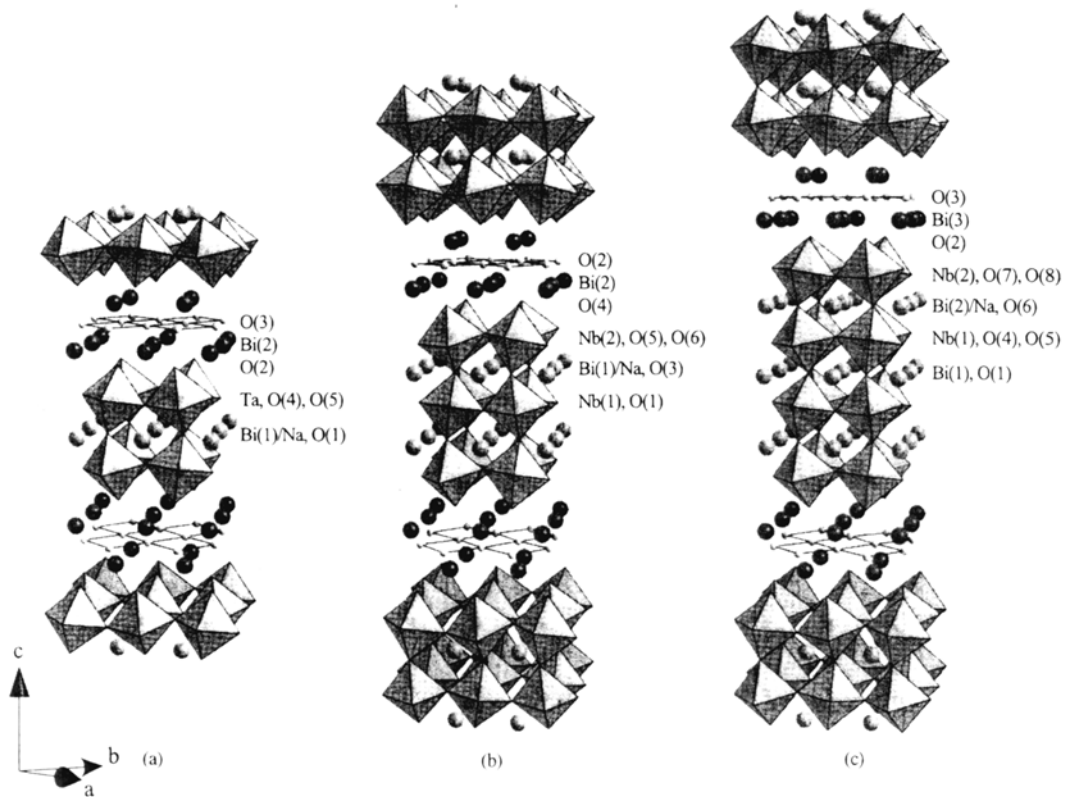


Figure 1.2. Schematic representations of the (a) $n=2$ (b) $n=3$ (c) $n=4$ Aurivillius materials. (From Reference 23).

The early work on oxygen ion conducting Aurivillius phases by Kendall involved incorporation of a brownmillerite-related perovskite layer. The brownmillerite phase is a perovskite that has adopted a structure that has ordered oxygen vacancies. The work of Kendall et al⁸⁻¹¹ showed high conductivity values at low temperatures (800°C) for the Aurivillius materials; however, the materials synthesized were not phase pure,³¹ and contained a secondary bismuth oxide phase. This impurity phase was the high temperature bismuth oxide structure (δ), which had been stabilized to room temperature by one of the many available cations. Bismuth oxide (and its solid solutions) is known to have high oxygen ion conductivity. However bismuth oxide easily reduces to metallic bismuth, making its applications limited.^{32,33} The high

temperature delta bismuth oxide phase can be stabilized at lower temperatures by “pulling” any of the cations of the Aurivillius structure, creating erroneously high conductivity values in the two phase composite. When bismuth oxide is present in multiphase samples it is known to melt in the temperature range (700-800°C), causing a significant increase in conductivity.³²⁻³⁴ Kendall et al. erroneously reported this jump in conductivity as an order/disorder transition.¹⁰

The early work on Aurivillius structures lead to an understanding that they are chemically flexible and readily accept substitutions to create oxygen vacancies. Most of this early work for $n=3$ Aurivillius phases was based off of $\text{Bi}_2\text{A}_2\text{B}'_2\text{B}''_1\text{O}_{11.5}$ where A is Sr or Pb, B' is Nb or Ta, B'' is Al or Ga.^{8-11,14,25,26,32-34} The conductivity values reported for these materials ranged from 10^{-4} S/cm to 1.2×10^{-2} S·cm⁻¹ at 800°C. More recent work has confirmed that many of the materials synthesized by Kendall et al.⁸⁻¹¹ were in fact not phase pure, and that the data reported by Kendall et al. was confounded by δ -bismuth oxide impurities.^{27,31,35,36}

The current understanding is that the Aurivillius materials are much less tolerant of substitutions than originally thought, and the high conductivity values originally reported by Kendall et al.⁸⁻¹¹ most likely cannot be reproduced in phase pure materials.³⁷ The goal of this research is to investigate the true structural limits of the $n=3$ Aurivillius materials and their electrical properties.

1.3 Impedance Spectroscopy

Impedance spectroscopy (IS) has emerged as a reliable means of investigating both bound and mobile charges in bulk or interfacial regions of a variety of materials, including those that are ionic, semiconducting, mixed conducting, and insulative.³⁸ The general approach is to apply a monochromatic (single frequency) voltage to the sample and measure the corresponding response current as the frequency is scanned.

Impedance spectroscopy is unique in its ability to resolve the responses of individual components within a complex system. This resolution is possible because different physical phenomena often relax at different frequencies.³⁹ Equation 1 below represents the monochromatic input voltage and Equation 2 is the complex response

current, where Θ is the phase different between voltage and current,. ω is the frequency ($\nu \equiv \omega/2\pi$), t is time, and the subscript m stands for measured.

$$v(t) = V_m \sin(\omega t) \quad (1)$$

$$i(t) = I_m \sin(\omega t + \theta) \quad (2)$$

Any inductive or capacitive effects of a sample are going to cause a corresponding phase shift of the response current with respect to the voltage. This phase shift is incorporated into the response as the phase angle θ . It is then understood that the impedance of a sample with no inductive or capacitive effects is zero and the response is purely resistive.³⁸ The conventional impedance is therefore defined as in Equation 3, and the magnitude of the impedance is as shown in Equation 4.

$$Z(\omega) = \frac{v(t)}{i(t)} \quad (3)$$

$$|Z(\omega)| = \frac{V_m}{I_m(\omega)} \quad (4)$$

The phase angle θ represents the magnitude and direction of the impedance. This can be determined from the real and imaginary components of impedance, $Z = a + jb$ or $Z(\omega) = Z' + jZ''$ as shown below in Figure 1.3. The response ($|Z(\omega)|$) is represented as a vector having both real and imaginary components that are the projection of the vector onto the corresponding axis³⁸

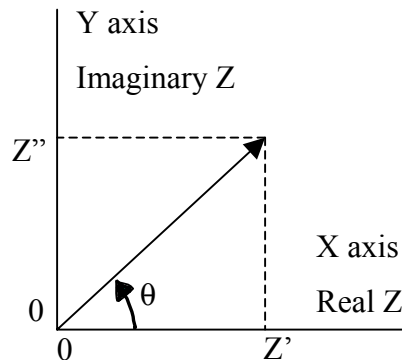


Figure 1.3. Impedance response showing real and imaginary components.

The equations for the components of impedance shown in Figure 1.3 are presented in Equations 6-8 below.

$$Z' = \text{real} = |Z| \cos(\theta) \quad (6)$$

$$Z'' = \text{imaginary} = |Z| \sin(\theta) \quad (7)$$

$$\theta = \tan^{-1} \left(\frac{Z''}{Z'} \right) \quad (8)$$

1.3.1 *Experimental Aspects of Impedance*

Even a state-of-the-art impedance analysis setup will have electrode leads that are long enough to effect the measurement. The inductive and capacitive effects of the electrodes will both play a part in the analysis; however, the magnitude of their effect will depend on the electrode type, length, and instrument quality. These apparatus effects present the need for correction files, which minimize these systematic errors. Edwards⁴⁰ implies that ceramics are especially susceptible to apparatus effects.

Typically, to correct for apparatus effects two measurements are made: one where a material that is the same as the electrode material connects the electrodes. This is known as the “short-circuit” condition. The second measurement is conducted where the test leads are separated by air by the thickness of a typical sample. This is known as the “open-circuit” condition. For each correction measurement it is necessary to take a correction reading at each temperature for temperature variant measurements. Another possibility is to only take a few measurements over the temperature range of interest and fit the data to obtain correction values for all the temperature values needed.⁴⁰

1.3.2 *Impedance of Ceramics*

The impedance response of a polycrystalline ceramic can have separate arcs when plotted as Z' vs. Z'' (Figure 1.4). The different arcs represent different electrical aspects of the sample. The low frequency arc represents grain boundary response, and the high frequency arc represents bulk grain response. In most cases, a small arc is visible in the low frequency domain, which is typically attributed to the electrodes. Also in many case the grain and grain boundary response are not visible as separate arcs. The arcs in the impedance response plot can also be modeled with equivalent

circuits. This can yield numerical values for the different electrical aspects of a material.⁴¹⁻⁴³ An example of a possible impedance response of a ceramic and the corresponding equivalent circuit is presented in Figure 1.4.

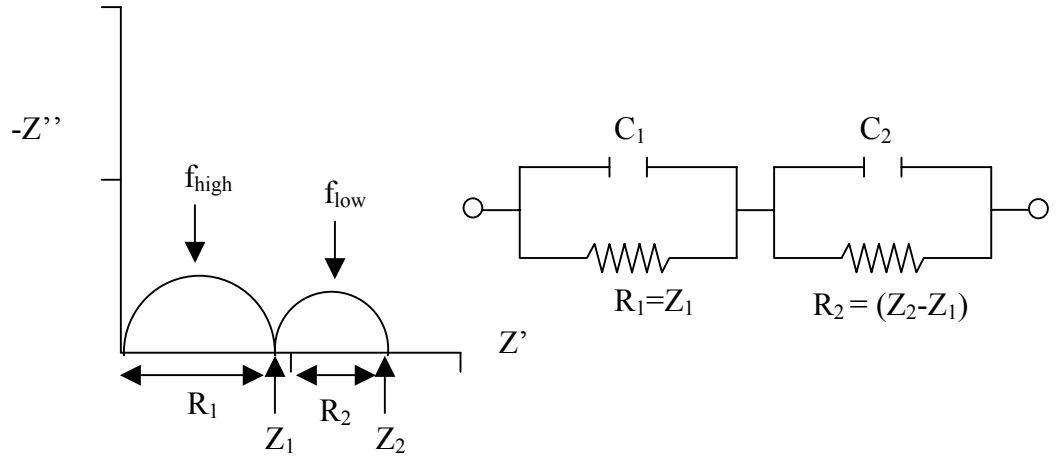


Figure 1.4. Possible impedance response plot of a polycrystalline ceramic and the corresponding RC equivalent circuit.

The resistance values of a given sample can be obtained from the response plots as is evident in Figure 1.4. When the phase angle θ goes to zero the impedance response represents only “real” impedance, and the values R_1 and R_2 in Figure 1.4 can be used to calculate the grain and grain boundary resistances. For the grain resistance this is simply the value Z_1 and for the grain boundary resistance this is the value $(Z_2 - Z_1)$.³⁸ Many times the high-frequency (or left-most) arc does not intersect with the origin of the plot. In such a case, the length of arc on the real axis is taken as the resistance R_1 , similar to obtaining the resistance for the grain boundary arc (R_2).

The corresponding capacitance values can be similarly calculated from the resistance values (see below). The C_1 in Equation 9 corresponds to grain resistance (R_1) and C_2 (Equation 10) corresponds to grain boundary resistance (R_2) f_1 and f_2 are the frequency values for the peak of the corresponding semicircle.³⁸

$$C_1 = \frac{1}{2\pi f_1 (R_1)} \quad (9)$$

$$C_2 = \frac{1}{2\pi f_2 (R_2 - R_1)} \quad (10)$$

IS Measurements are typically made on a 4-5 lead, 2-point impedance spectroscopy (IS) system. In this type of IS opposing sides of the pellet are fully electroded. Four electrode leads are utilized, two on one pellet face and two on the other, while the fifth lead (if present) is a shielding. The effects of poor contacts of the leads must be considered as well. With poor electrode contacts a “spreading resistance” can occur between the electrode and the specimen, which can increase and even dominate the apparent bulk resistance.⁴⁴

1.4 Ionic Conductivity

The conductivity is the proportionality constant relating current density to the electric field as shown below in Equation 11.

$$I = \sigma E \quad (11)$$

Where I = current density = Amps•cm⁻²

σ = conductivity = S•cm⁻¹

E = Electric field = V•cm⁻¹

Once the impedance response of the material under investigation has been determined, the resistance values for the sample can be related to the conductivity using the geometry of the sample and Ohms law, which simplifies Equation 11 into Equation 12.

$$\sigma = \frac{t}{AR} \quad (12)$$

Where t is the thickness of the sample (cm), A is the cross sectional area (cm²), and R is the resistance (Ω). The conductivity (σ) in units (Ωcm)⁻¹ is reported as S•cm⁻¹.

The conductivity (S•cm⁻¹) is proportional to the concentration of charge carriers (c = carriers•cm⁻³), the charge they carry (ze = C•carrier⁻¹) and the mobility (μ = cm²•V⁻¹s⁻¹) of the carrier as in Equation 13.

$$\sigma = cze\mu \quad (13)$$

To find the conductivity the current density (I) in the material needs to be known. This current density will be the sum of current flow with and against the

direction of the applied field, since ionic conductivity is a hopping mechanism the distance and barrier height of jumps must be accounted for as shown in Equation 14.

$$I = c z e a v e^{-h_0/kT} \left(e^{\frac{z e a E}{2kT}} - e^{-\frac{z e a E}{2kT}} \right) \quad (14)$$

Where a is the jump distance (nm•jump⁻¹)

h_0 is the barrier height (eV)

v is the jump frequency (jump•s⁻¹)

Equation 14 can be further simplified by noting that $e^x - e^{-x} = 2\sinh x$, yielding Equation 15.

$$I = 2c z e v e^{-h_0/kT} \sinh \frac{z e a E}{2kT} \quad (15)$$

The hyperbolic sine term can be expanded into a series ($\sinh x = x + x^3/3! + x^5/5!$) and the x value is given by $x = z e a E / 2kT$. If the field is low enough we can approximate that $x \ll 1$, yielding the current density as equation 16, and the conductivity as equation 17. Comparison of Equation 17 with Equation 13 enables the mobility to be defined as Equation 18.

$$I \approx \frac{z^2 e^2 c}{kT} a^2 v e^{-h_0/kT} E \quad (16)$$

$$\sigma \approx \frac{z^2 e^2 c a^2}{kT} v e^{-h_0/kT} \quad (17)$$

$$\mu = \frac{z e a^2}{kT} v e^{-h_0/kT} \quad (18)$$

The conductivity is typically plotted in Arrhenius form, where the log of equation 17 is taken, and a plot such as Figure 1.5 is obtained. The benefit of the Arrhenius conductivity plot is that the activation energy can be easily be obtained as the slope is equal to $-E_a/k$. It must also be noted that the Arrhenius conductivity plot may have two or more regions of different slope. Where each region of different slope correlates to a region of different activation energy. In such a case all regions must be considered and multiple activation energies calculated. This is illustrated graphically below in Figure 1.5.

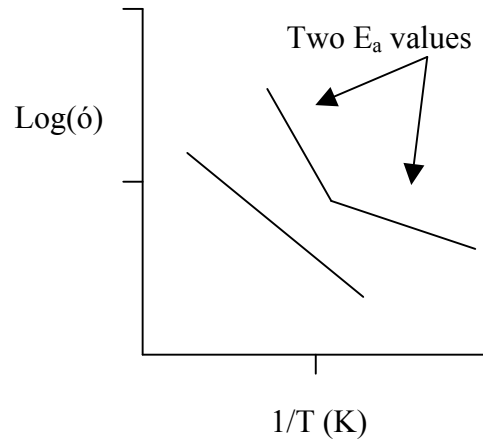


Figure 1.5. Arrhenius conductivity plot exhibiting single and dual activation energy materials.

1.4.1 Ionic Conductivity in Ceramics

Oxygen-ion conductivity in ceramics is a diffusion driven process, where oxygen ions move via a hopping mechanism through the crystal structure of the ceramic. One way for ionic conductivity in ceramics to occur is by substitutions with cations of lower valence (aliovalent substitution). This creates a net positive charge within the structure, which can be compensated for by the creation of an oxygen vacancy. This creates the conduction mechanism; hence the mobile oxygen ions hop from vacant site to vacant site causing ionic conduction, which is schematically shown in Figure 1.6 and Figure 1.7. The driving force for this diffusive process is either a chemical or electrical potential applied across the membrane.⁴⁵

Because this hopping conductivity mechanism is a diffusion driven process, an analogy is often made to potential wells. An oxygen ion sitting in one vacancy is in a low-energy state, and needs to overcome a minimum energy in order to move to a new vacant site. This energy to be overcome is referred to as the activation energy (E_a), which can be obtained from the slope of an Arrhenius conductivity plot. This concept is illustrated schematically in Figure 1.6.

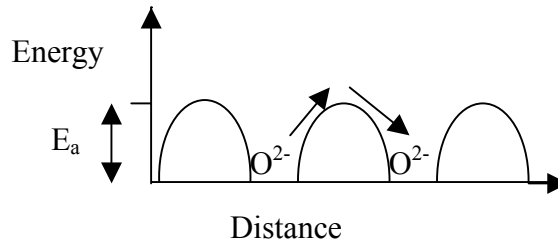


Figure 1.6. Graphical illustration of activation energy required for conduction.

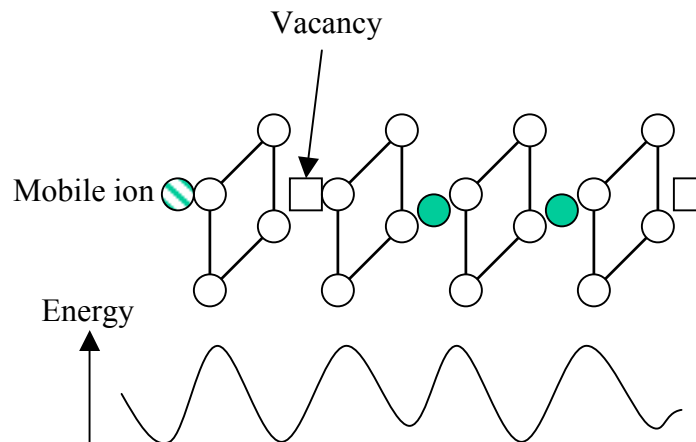


Figure 1.7. Graphical illustration of varying potential energy along the oxygen diffusion path (diffusion path is considered left to right on the page).

Because the oxygen ion conductivity occurs via oxygen ions hopping between oxygen vacancies, the conductivity is proportional to the concentration and mobility of oxygen vacancies within the structure. Higher conductivity can result if there are more vacancies or if the mobility of the vacancies increases.

When transition metals are present in a ceramic, the charge conduction mechanism is often small polaron type conduction. In such a case a cation traps an extra electron, which can hop from cation to cation, conducting the electron through the structure. The ease of conduction is related to the changing valence of the transition metal cation, the easier the cation can change valence state (as the electron interacts with it) the easier it is for the electron to travel through the structure.³⁷

1.5 Polymerized Complex Synthesis

Processing by wet chemical means can drastically reduce processing times by providing mixing on the atomic scale. Wet chemical synthesis also typically yields a highly pure, homogenous product. The drawback of chemical processing has been its complex nature, as many parameters (temperature, pH, solvent) can affect the final product. Conversely, the main advantage of the solid-state synthesis is its simplicity.⁴⁶

A variety of Aurivillius materials have been synthesized by the polymerized complex method,^{16,47,48} the general steps of which are outlined by Luisi.⁴⁶ The polymerized complex method is capable of evenly dispersing cations within a polymer matrix, which can then be calcined into the corresponding oxide.

Cation salts are typically used as the cation sources; which are dissolved in de-ionized water. This solution is then added to citric acid and ethylene glycol. The cation solution is then mixed at 60°C until it is clear, which ensures that no precipitation reactions have occurred. The metal cations then bond (chelates) with the citric acid, as the solution is heated to 100°C. This citric acid-cation pair then bridges with the ethylene glycol, forming the polymer network binding the metal cations, with water as a by-product. The excess water is simultaneously evolved from this solution at this step.⁴⁶ Once the majority of the water has left the network, a viscous mass results, which can be further dried before organic burnoff and calcination. A schematic flow chart of this process is presented in Figure 1.8.

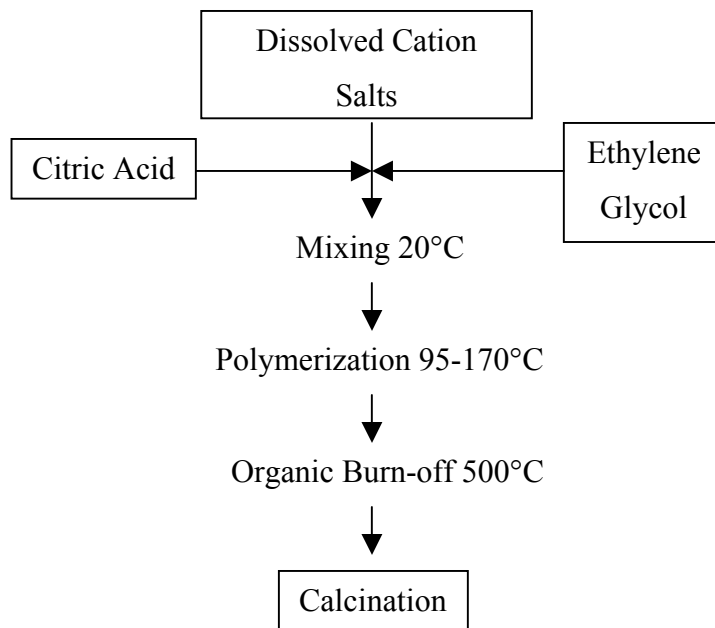


Figure 1.8. Flow chart for the polymerized complex synthesis method. (From Reference 45).

2 EXPERIMENTAL PROCEDURE

2.1.1 *Compositions Attempted and Strategy*

All compositions attempted are listed in Table I. There are two main series of compositions based on the parent phase $\text{Bi}_2\text{Sr}_2\text{Nb}_2\text{TiO}_{12}$. Those substituted on the titanium site with transition metals are referred to as the transition metal series with the general formula $\text{Bi}_2\text{Sr}_2\text{Nb}_2\text{Ti}_{(1-x)}\text{M}_x\text{O}_{12-\delta}$ ($x=0-1$, $\text{M}=\text{Co}, \text{Cr}, \text{Fe}, \text{Mn}$). A series of compositions exchanging lead for bismuth are referred to as the lead series, with the general formula $\text{Bi}_{(2-y)}\text{Pb}_y\text{Sr}_2\text{Nb}_2\text{TiO}_{12-\delta}$ ($y=0.1, 0.2, 0.3, 0.4, 0.5, 0.6, 1$). Also when referring to the amount of substitution on a site, the percent of the substitution on the site it occupies is referred to as the atom%. For example the compositions $\text{Bi}_2\text{Sr}_2\text{Nb}_2\text{Ti}_{1.8}\text{Fe}_{0.2}\text{O}_{12-\delta}$ and $\text{Bi}_{1.8}\text{Pb}_{0.2}\text{Sr}_2\text{Nb}_2\text{TiO}_{12-\delta}$ have 20 atom% iron exchanged for titanium and 10 atom% lead exchanged for bismuth. These compositions are referred to as having 20 atom% iron and 10 atom% lead substitution, respectively.

When investigating these series of compositions a specific terminology will be utilized, which must be explained before proceeding. When describing a specific composition for one of the series presented above, either the exact composition or the substitution amount (ie $x=0.1$ or $y=0.2$) will be stated.

The first step in determining the substitutions to attempt is looking at the ionic radius of the proposed substitutions and compare it to the radius of the ion it is replacing. This was done for the transition metal series, and a percent difference to titanium in 6-fold coordination is presented in Table III. The ionic radius for bismuth (Bi^{3+}) in 8-fold coordination is 1.31\AA and for lead (Pb^{2+}) in 8 fold coordination is 1.43\AA , a reasonable match. Typically a difference of more than 12% in ionic radius between the substitution and the host site will not result in phase purity.⁴⁹

The transition metal substitutions were attempted because of their ability to change valence to best fit the needs of the structure. The idea was that the transition metal would replace some of the titanium in the perovskite layer, and create a site for electronic conduction.

Table I: List of Compositions Whose Synthesis was Attempted.

Transition Metal Substitutions	Lead and Aluminum Substitutions
$\text{Bi}_2\text{Sr}_2\text{Nb}_2\text{Ti}_{0.95}\text{Fe}_{0.05}\text{O}_{11.975}$	$\text{Bi}_{1.9}\text{Pb}_{0.1}\text{Sr}_2\text{Nb}_2\text{TiO}_{11.95}$
$\text{Bi}_2\text{Sr}_2\text{Nb}_2\text{Ti}_{0.9}\text{Fe}_{0.1}\text{O}_{11.95}$	$\text{Bi}_{1.8}\text{Pb}_{0.2}\text{Sr}_2\text{Nb}_2\text{TiO}_{11.9}$
$\text{Bi}_2\text{Sr}_2\text{Nb}_2\text{Ti}_{0.8}\text{Fe}_{0.2}\text{O}_{11.9}$	$\text{Bi}_{1.7}\text{Pb}_{0.3}\text{Sr}_2\text{Nb}_2\text{TiO}_{11.85}$
$\text{Bi}_2\text{Sr}_2\text{Nb}_2\text{Ti}_{0.5}\text{Fe}_{0.5}\text{O}_{11.75}$	$\text{Bi}_{1.6}\text{Pb}_{0.4}\text{Sr}_2\text{Nb}_2\text{TiO}_{11.8}$
$\text{Bi}_2\text{Sr}_2\text{Nb}_2\text{Ti}_{0.25}\text{Fe}_{0.75}\text{O}_{11.625}$	$\text{Bi}_{1.5}\text{Pb}_{0.5}\text{Sr}_2\text{Nb}_2\text{TiO}_{11.75}$
$\text{Bi}_2\text{Sr}_2\text{Nb}_2\text{FeO}_{11.5}$	$\text{Bi}_{1.4}\text{Pb}_{0.6}\text{Sr}_2\text{Nb}_2\text{TiO}_{11.7}$
$\text{Bi}_2\text{Sr}_2\text{Nb}_{1.5}\text{Fe}_{0.5}\text{Ti}_{0.5}\text{Fe}_{0.5}\text{O}_{11.5}$	$\text{BiPbSr}_2\text{Nb}_2\text{TiO}_{11.5}$
$\text{Bi}_2\text{Sr}_2\text{Nb}_{1.3}\text{Fe}_{0.7}\text{Ti}_{0.5}\text{Fe}_{0.5}\text{O}_{11.35}$	$\text{Bi}_{0.8}\text{Pb}_{1.2}\text{Sr}_2\text{Nb}_2\text{TiO}_{11.4}$
$\text{Bi}_2\text{Sr}_2\text{Nb}_2\text{Ti}_{0.95}\text{Cr}_{0.05}\text{O}_{11.975}$	$\text{Bi}_2\text{Sr}_2\text{Nb}_2\text{Ti}_{0.75}\text{Al}_{0.25}\text{O}_{11.5}$
$\text{Bi}_2\text{Sr}_2\text{Nb}_2\text{Ti}_{0.9}\text{Cr}_{0.1}\text{O}_{11.95}$	$\text{Bi}_{1.6}\text{Pb}_{0.4}\text{Sr}_2\text{Nb}_2\text{Ti}_{0.8}\text{Al}_{0.2}\text{O}_{11.7}$
$\text{Bi}_2\text{Sr}_2\text{Nb}_2\text{Ti}_{0.8}\text{Cr}_{0.2}\text{O}_{11.9}$	$\text{Bi}_2\text{Sr}_2\text{Nb}_2\text{AlO}_{11.5}$
$\text{Bi}_2\text{Sr}_2\text{Nb}_2\text{Ti}_{0.5}\text{Cr}_{0.5}\text{O}_{11.75}$	
$\text{Bi}_2\text{Sr}_2\text{Nb}_2\text{Ti}_{0.95}\text{Co}_{0.05}\text{O}_{11.975}$	
$\text{Bi}_2\text{Sr}_2\text{Nb}_2\text{Ti}_{0.8}\text{Co}_{0.2}\text{O}_{11.9}$	
$\text{Bi}_2\text{Sr}_2\text{Nb}_2\text{MnO}_{11.5}$	

It was also the intention that once a suitable electronic conductor was obtained one could substitute on the bismuth site (with lead) to create some ionic conduction, yielding a mixed conductor as a final product. The overall goal of the transition metal series remained to determine the structural limits of substitutions on the titanium site, and the effect of the substitutions on the electrical properties of the material.

The transition metals cobalt, chromium and iron were selected by comparing their size to that of titanium (all in 6-fold coordination) using Shannon's⁵⁰ ionic radii (Table II). If titanium (in 6-fold coordination) is considered to be the optimum size for the structure (at 0.6\AA), the predicted stability can be related to the ionic radius of the substitution. The transition metals can enter the structure as a mixture of valence states (3+, 4+ and even 2+). By examining the ionic radii presented in Table II one can make a

rough prediction about stability of the transition metal substitutions. Iron is the closest match to titanium in three valence states, with chromium and cobalt following (both suitable matches in two valence states).

Table II: Ionic Radii of Transition Metals Substituted for Titanium.⁵⁰

Atom	Charge	Coordination	Radii (Å)	% difference (Ti)
Ti	4+	6	0.61	0.00%
Nb	5+	6	0.64	5.79%
Fe	2+	6	0.61	0.83%
	3+	6	0.65	6.61%
	4+	6	0.59	-3.31%
Cr	2+	6	0.80	32.23%
	3+	6	0.62	1.65%
	4+	6	0.55	-9.09%
	5+	6	0.49	-19.01%
	6+	6	0.44	-27.27%
Co	2+	6	0.75	23.14%
	3+	6	0.61	0.83%
	4+	6	0.53	-12.40%
Mn	2+	6	0.83	37.19%
	3+	6	0.645	6.61%
	4+	6	0.53	-12.40%

The composition $\text{Bi}_2\text{Sr}_2\text{Nb}_2\text{MnO}_{12}$ was attempted because Yu⁵¹ stated that he was successful in synthesizing it yet provided insufficient data to confirm this. There are other cations that might have substituted successfully at low levels e.g. V and Ni; however, Cr, Fe, and Co were chosen because they were a good match in several valence states and were most likely to substitute into the structure at the highest levels.

The atomic radii published by Shannon⁵⁰ show that the atomic radius of strontium (1.32 Å) is close to Fe²⁺ in the high spin state (1.1 Å). Therefore an attempt was made to substitute iron for strontium, in addition to the substitution of 50 atom% on the titanium site discussed in Section 3.2.

The compositions within the lead series $\text{Bi}_{(2-x)}\text{Pb}_y\text{Sr}_2\text{Nb}_2\text{TiO}_{12-\delta}$ ($y=0.1, 0.2, 0.3, 0.4, 0.5, 0.6, 1$) were chosen because initial work completed by Luisi⁴⁶ showed phase purity for $\text{Bi}_{1.4}\text{Pb}_{0.6}\text{Sr}_2\text{Nb}_2\text{TiO}_{12-\delta}$. It was hoped that addition of the lower valence (2^+) lead ions onto the bismuth (3^+) sites would create oxygen vacancies in the bismuth layer, and cause the conductivity of the material to increase. It was also shown by several other authors that substitution of lead for bismuth was successful.^{25,26}

The substitution of aluminum for titanium was also attempted because of initial work completed by Luisi.⁴⁶ It was once again hoped that the substitution of the lower valence aluminum ions into the perovskite layer would create oxygen vacancies and increase the materials conductivity.

The polymerized complex method was utilized for all compositions because it was believed this was the best way to determine the structural limits of the substitutions. Due to the atomic scale mixing of chemical processing, successful synthesis by the polymerized complex method (Figure 1.8) is much more likely than by solid-state processing.

2.1.2 Synthesis

A list of all compositions attempted is provided in Table I. The polymerized complex method involves dissolving stoichiometric amounts of all constituents into solution (either H_2O or HCl). The polymerizing agents are then added to this cation solution: citric acid was added in a 30:1 molar ratio with the cations, Ethylene glycol was added in a 4:1 molar ratio with the citric acid. The resulting final solution was then stirred magnetically while heated to 95°C to evaporate the solvent. Gradual polymerization of the citric acid occurred as the solvent evaporated, resulting in a viscous mass. The solvent evaporation was completed by heating in a furnace at 180°C for 6 hours. The organics were then removed by heating, uncovered, in a Pyrex beaker at $450\text{-}500^\circ\text{C}$ under a continuously flowing air atmosphere, which aided in organic burnoff. Calcination was completed by placing the organic-free powder into a covered MgO crucible and heating to 900°C for 10 hours in a closed (static air) furnace.^{16,46-48,52,53} All of the precursor materials used in the polymerized complex processing are presented in Table III .

Table III: List of Polymerized Complex Precursor Materials.

Precursor	Purity (%)	Source
Bi_2O_3	99.99	Alfa-Aesar
$\text{Sr}(\text{NO}_3)_2$	98	Alfa-Aesar
NbCl_5	99	Alfa-Aesar
Ti(IV)butoxide	99+	Alfa-Aesar
PbO	99.9	Acros
$\text{Al}(\text{NO}_3)_3 \cdot 9\text{H}_2\text{O}$	98	Alfa-Aesar
$\text{Ca}(\text{NO}_3)_2 \cdot 4\text{H}_2\text{O}$	99	Alfa-Aesar
$\text{Ba}(\text{NO}_3)_2$	99.4	Fisher Sci.
$\text{Co}(\text{NO}_3)_2 \cdot 6\text{H}_2\text{O}$	98-100	Alfa-Aesar
$\text{Cr}(\text{NO}_3)_3 \cdot 9\text{H}_2\text{O}$	99-100	Alfa-Aesar
$\text{Fe}(\text{NO}_3)_3 \cdot 9\text{H}_2\text{O}$	98+	Alfa-Aesar
Citric Acid	99.5	Alfa-Aesar
Ethylene Glycol	99+	Alfa-Aesar
$\text{Mn}(\text{NO}_3)_2$ solution	50% H_2O	Alfa-Aesar

Bismuth oxide was dissolved in a 10 ml solution of 36.5% - 38% HCl in water (Alfa-Aesar). Lead oxide was dissolved in a heated solution of the hydrochloric acid on a magnetic hot plate with stirring. The niobium (V) chloride was dispensed in a glove box under a hydrogen/nitrogen atmosphere (to prevent decomposition of the chloride) and subsequently dissolved in 5 ml of hydrochloric acid. Titanium (IV) butoxide was dissolved directly into ethylene glycol. All other nitrates were dissolved in 10mL of de-ionized water. After all of the cations were individually dissolved they were combined in a beaker. To this solution, a 30 mole % excess of citric acid was added to chelate the metal cations. Ethylene glycol was then added in a 4:1 molar ratio with the citric acid.⁴⁶ The exact amounts of each component depended on the desired amount of final product and composition. In order to provide a frame of reference the amount of the materials used in synthesizing a four gram batch of $\text{Bi}_{1.9}\text{Pb}_{0.1}\text{Sr}_2\text{Nb}_2\text{TiO}_{12-\delta}$ are presented in Table IV.

Table IV: Batch Constituents for a four gram batch of $\text{Bi}_{1.9}\text{Pb}_{0.1}\text{Sr}_2\text{Nb}_2\text{TiO}_{12-\delta}$.

Precursor	g needed	moles	Solution	Solution Vol (ml)
Bi_2O_3	1.328	0.0057	HCl	10
PbO	0.067	0.0003	HCl	30
$\text{Sr}(\text{NO}_3)_2$	1.270	0.0060	H ₂ O	10
NbCl_5	1.621	0.0060	H ₂ O	5
Ti-Butoxide	1.021	0.0030	Ethylene Glycol	10
Citric Acid	80.69	0.42	Cation solution	-
Ethylene Glycol	94.05 (ml)	1.68	Cation solution	-

Sintering was completed after pressing pellets into disks with a 1 cm die to 34 MPa with a hold time of one minute. The resulting disks were placed in a sacrificial powder bed of identical composition and sintered in covered MgO crucibles at 1050°C for 30 hours. The powder bed was used to minimize bismuth vaporization from the sample, which was confirmed to be negligible by weighing all samples before and after sintering.

2.1.3 Density Measurements

All density measurements were completed on pellets made using ASTM standard C 20-97.⁵⁴ With a basic procedure as follows. The pellet was first heated in air to 110°C for 20 minutes and the dry weight was measured. The pellet was then boiled in water for two hours, and subsequently cooled to room temperature. The pellet then sat in water for 12 hours. The suspended weight of the pellet in water was then measured. The pellet was then blotted with a wet paper towel and the saturated weight was measured. The density was then calculated by dividing the dry weight (D) by the saturated (W) minus the suspended (S) weight $\{\rho=D/(W-S)\}$. All theoretical density values were obtained via the Powdercell program,⁵⁵ which calculates the theoretical density from the size of the unit cell and mass of constituent ions.

2.1.4 Phase Analysis Via X-ray Diffraction

All x-ray diffraction experiments were performed on a Siemens D500 diffractometer utilizing Bragg-Brentano geometry, unless otherwise noted. The D500

instrument was equipped with a graphite diffracted beam monochromator, with fixed divergence slits of 0.3° . The source radiation was copper $K\alpha$, with a wavelength of 1.54\AA . Diffraction experiments were completed with source power levels of 40 kV and 30 mA, ranging from $2-100^\circ 2\theta$ with a step size of 0.02 or 0.04° , and count times of 6-10 seconds. All powder samples were prepared by loading into a top-loaded holder utilizing a Siemens sample changer, rotating at 50 rpm during the measurement. Unless otherwise noted all diffraction experiments for sintered powders were completed on solid pellet faces.

2.1.5 Use of Jade 6.0 for XRD Analysis

Jade 6.0 is an x-ray diffraction pattern analysis software, and was utilized for all XRD analysis. Phase identification was completed using a least squares algorithm to present a list of possible PDF matches, using the information on possible elements present in the sample. The choices presented by Jade were then manually refined to identify possible phases in the pattern. Profile fitting was completed using Jade 6.0, with the default profile fitting parameters (Pseudo-Voigt shape, $K\alpha_2$ present, fixed background, exponent=1.5, lorentzian=0.5).

2.1.6 Scanning Electron Microscopy

Scanning electron microscopy (SEM) was conducted using a Phillips 515 electron microscope. An acceleration voltage of 20kV was used with a LaB_6 filament. Microstructural characterization was completed under secondary electron imaging. The presence of secondary phases was investigated under backscatter electron imaging, in conjunction with an EVEX EDS for elemental analysis.

Electron microscopy was completed on polished pellet faces. All pellets were prepared for SEM by polishing one pellet face using 400, 600, and 1000 grit SiC polishing paper, washing samples between polishing steps. Polished samples were then coated with 60:40 Au:Pd conductive layer. Samples were then placed on aluminum stubs and conductive carbon tape was used to connect the faces with the stub.

2.1.7 Electrical Characterization

2.1.7.1 Impedance Spectroscopy

Impedance spectroscopy (IS) was completed utilizing a two-point, 5-terminal geometry. Measurements were obtained using a Solartron 1260 impedance/gain analyzer and a Centurion Qex furnace, using platinum leads. Data was typically collected from RT-1000°C in 200°C intervals from RT-400°C, in 100°C intervals from 400-700°C, and in 50°C intervals from 700-1000°C. One-centimeter diameter pellets were electroded on both faces by painting on a platinum paste* and firing to 900°C for 1 hour. The measurements ranged from 5Hz-15MHz with 100 data points collected by scanning from low to high frequency.

The IS data typically consisted of one broad arc combining bulk and grain boundary response at high frequencies, and in most cases a small electrode arc was visible at low frequency. The IS analysis software Zview⁵⁶ (Scribner & Ass., 1999) was utilized for analysis of IS data. The width of the high frequency arc was utilized as the sample resistance in all conductivity calculations. Correction files were utilized to limit the effects of systematic errors. Confirmatory DC measurements were completed from RT-1000°C and compared to IS data to check for accuracy and systematic errors.

2.1.7.2 Controlled Atmosphere DC Conductivity

Four-point DC conductivity was measured under controlled atmospheres utilizing a Centurion Qex furnace, and a voltage supply of 3V. The current and voltage responses of a conductivity bar were monitored using Keithley 2000 multimeters. Bars were prepared using a 1.9 by 0.6 cm rectangular die and pressing the bars to 34 MPa and sintering as pellets. Samples were run under air ($P_{O_2} = 0.22$), oxygen ($P_{O_2} = 1.0$), 99%Ar-1%O₂ ($P_{O_2} = 0.01$), and Ar ($P_{O_2} = 0.005$). A flow rate of 1 liter/min was used for all gasses. The oxygen level* in the furnace was monitored using a Thermo series-2000 oxygen monitor.

* Platinum Ink, Lot # M31914A Englehard Inc, Eselin, NJ

The furnace was purged for 2-4 hours before each measurement was started, followed by two-hour holds at each temperature used. The temperature was increased at 100°C intervals from 500-800°C.

3 RESULTS AND DISCUSSION

3.1 Characterization of $\text{Bi}_2\text{Sr}_2\text{Nb}_2\text{TiO}_{12}$

3.1.1 *Synthesis of $\text{Bi}_2\text{Sr}_2\text{Nb}_2\text{TiO}_{12}$*

$\text{Bi}_2\text{Sr}_2\text{Nb}_2\text{TiO}_{12}$ was synthesized as described in Section 2.1.2. The diffraction patterns for $\text{Bi}_2\text{Sr}_2\text{Nb}_2\text{TiO}_{12}$ after calcination and sintering are shown in Figure 3.1.

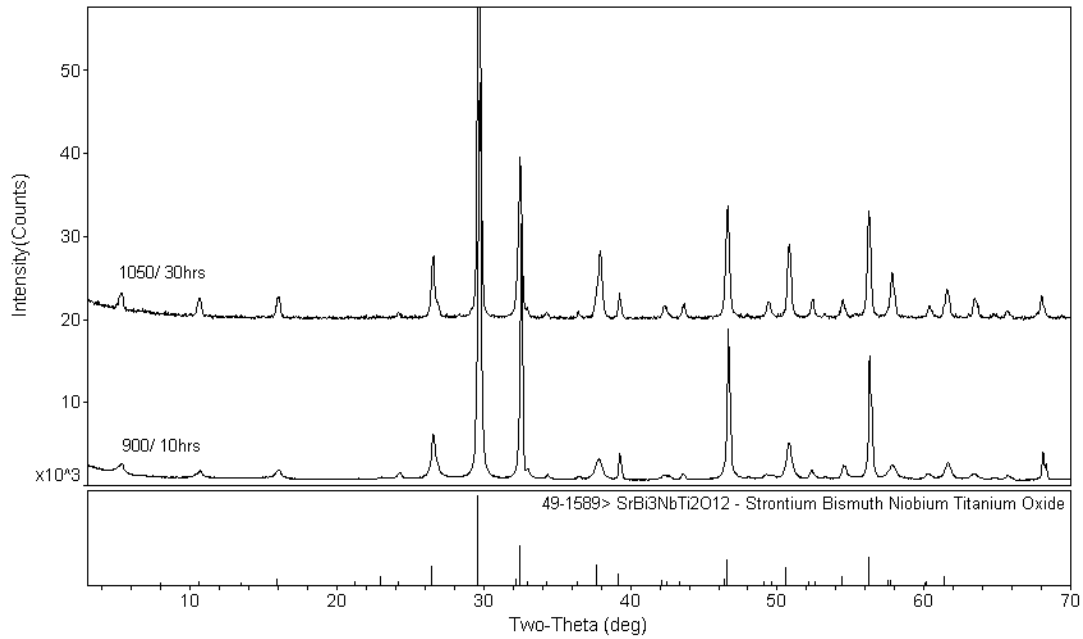


Figure 3.1. XRD patterns for $\text{Bi}_2\text{Sr}_2\text{Nb}_2\text{TiO}_{12}$ after calcination (900°C/10hrs) and sintering (1050°C/30hrs). The sticks in the bottom of the figure represent the peak placement of the corresponding PDF cards.

3.1.2 *Electrical Characterization of $\text{Bi}_2\text{Sr}_2\text{Nb}_2\text{TiO}_{12}$*

$\text{Bi}_2\text{Sr}_2\text{Nb}_2\text{TiO}_{12}$ has been well characterized by Haluska³⁷ and Peterson⁵⁷, as a baseline 2-point impedance was employed as described in Section 2.1.7.1 to measure the conductivity.

A typical Cole-Cole impedance plot for $\text{Bi}_2\text{Sr}_2\text{Nb}_2\text{TiO}_{12}$ is shown in Figure 3.2 below. Notice the well resolved grain and grain boundary arcs described in Section 1.3.2 are not distinguishable; one large arc is present that resembles a depressed semicircle. This is most likely because the two responses are blended together, and appear as one large arc, while the very small arc at low frequency (high Z') is likely the electrode response. In such cases the intercept of this large high-frequency arc with the real (Z') axis was taken as the resistance value at that temperature.

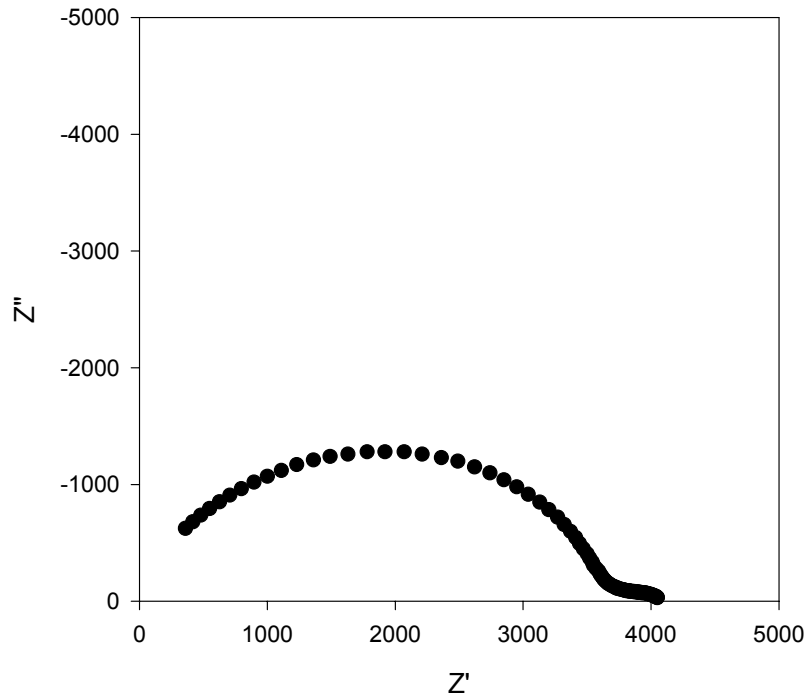


Figure 3.2. Typical Cole-Cole plot of $\text{Bi}_2\text{Sr}_2\text{Nb}_2\text{TiO}_{12}$ (600°C).

The conductivity value exceeds 10^{-3} S/cm at 1000°C, as seen in Figure 3.3. This is substantially below that of the industry standard, YSZ, which is 10^{-1} S \cdot cm $^{-1}$ at 800°C. The conductivity of the parent phase is notably low, and it was hoped that the substitutions substituted into the structure would increase the conductivity.

Note that in the parent phase, there are clearly two activation energy regions present in the Arrhenius conductivity plot. At low temperatures (200-400°C) the activation energy appears extrinsic and is about 0.25eV. Above 400°C, the activation energy appears to be extrinsic, at approximately 1eV.

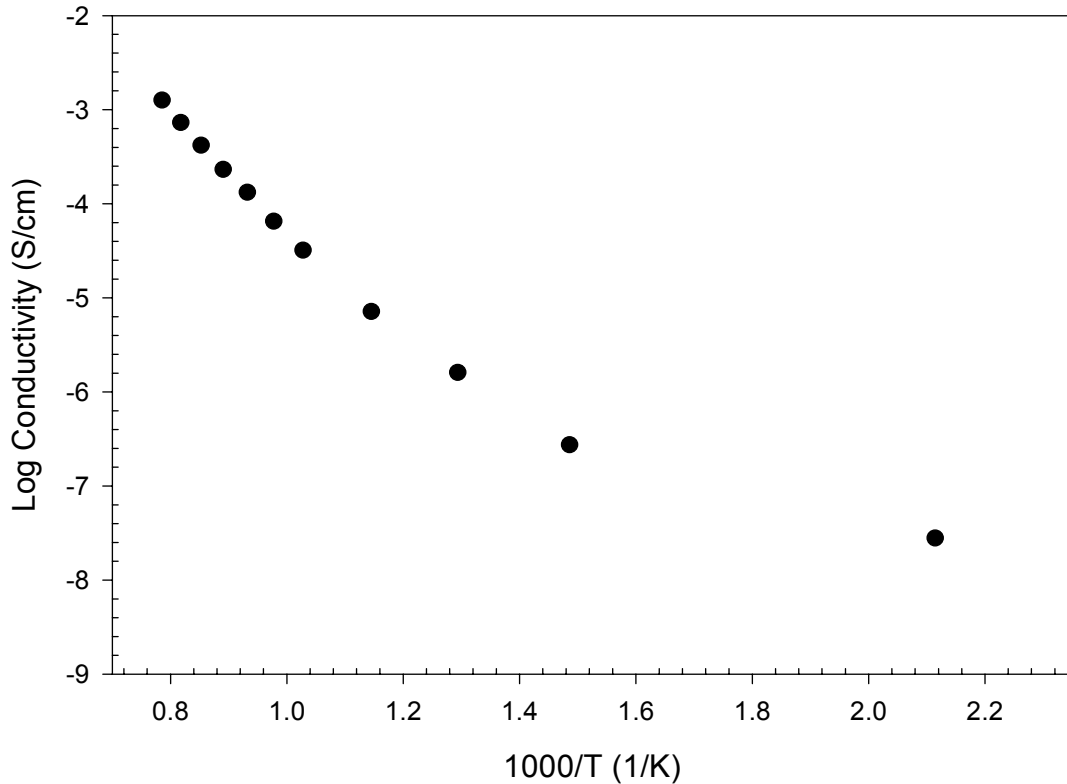


Figure 3.3. Conductivity of $\text{Bi}_2\text{Sr}_2\text{Nb}_2\text{TiO}_{12}$ from 2-point AC impedance spectroscopy.

3.1.3 *Microstructure of $\text{Bi}_2\text{Sr}_2\text{Nb}_2\text{TiO}_{12}$*

SEM was conducted as described in Section 2.1.6 on the $\text{Bi}_2\text{Sr}_2\text{Nb}_2\text{TiO}_{12}$ sample, obtaining both SE and BSE images. Bismuth oxide is the most common impurity in Aurivillius materials, and appears as a bright phase in BSE images if present.^{27,35,36} A lack of such bright regions, or other any phase contrast in the backscatter electron (BSE) images is an indication of phase purity. Notice the low sintered density evident in the micrographs of Figure 3.4. The SEM images of a high-density ceramic would show hardly any porous regions or granular features unless etched. Comparison of the SEM images presented for the hot-pressed sample in Section 3.1.4 clearly illustrate the low density of $\text{Bi}_2\text{Sr}_2\text{Nb}_2\text{TiO}_{12}$.

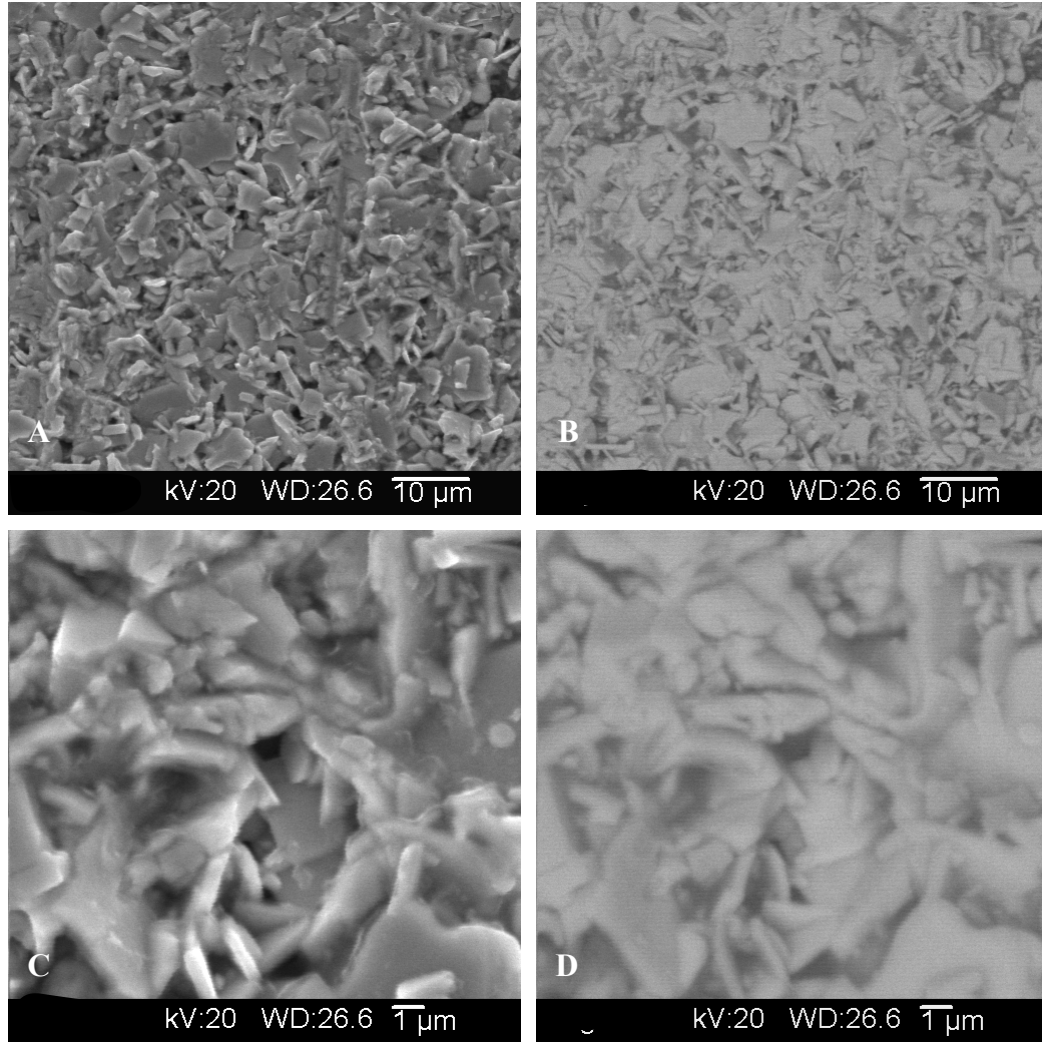


Figure 3.4. SEM images of $\text{Bi}_2\text{Sr}_2\text{Nb}_2\text{TiO}_{12}$ pellet face polished to 1000grit A and C are SE images, while B and D are the corresponding BSE images.

3.1.4 Sintering and Density of $\text{Bi}_2\text{Sr}_2\text{Nb}_2\text{TiO}_{12}$

The $n=3$ Aurivillius materials and related phases do not sinter well.⁵⁷ The optimum sintering time is 1050°C for 30 hours. This typically yields a sintered pellet of 50-60% theoretical density. With a theoretical density of 6.73g/cm³, sample densities were typically about 3.5-4g/cm³. In an effort to increase the sintered density, a hot pressing technique was attempted using a custom-built hot press. The hot press involved placing an already-sintered pellet on the flat faces of two rods of alumina; the pellet was then sintered at 800°C for eight hours with 16kg of weight applied to the metal fulcrum arm, which places the weight on the alumina rods. Using this technique,

a pellet of about 90% theoretical density was prepared. The SEM images obtained of polished and unpolished faces of this pellet are shown in Figure 3.5.

Although hot pressing the samples significantly increased the density of sintered pellets, it was not possible to prevent pellets from fracturing. Many samples deteriorated into very small (and dense) pieces. SEM data in Figure 3.5 was taken on a pellet that fractured into only two pieces. One part was utilized for SEM and the other for AC conductivity. The conductivity did not increase noticeably with the hot pressed piece, and the shape of Cole-Cole plots did not change either. It was expected that the grain and grain boundary arc would both be visible, but this was not the case.

This lack of improvement in properties could be attributed to the integrity of the pellet after hot pressing. Even though the AC conductivity piece was solid, there were large cracks in the pellet, as seen in Figure 3.5 B. These cracks would inhibit easy transfer of charge carriers through the sample, and could mask any increase in conductivity. Even though hot pressing was successful at increasing the density of the samples, it was not a viable option for use with subsequent samples.

Comparison of all SEM images presented for other samples can be made with those in Figure 3.5 as a means of visually comparing the density, as the images for the hot pressed sample are very high density and appear mostly flat and featureless. This is not the case for SEM images for other samples; which are much lower in density and subsequently a large amount of open porosity is typically apparent.

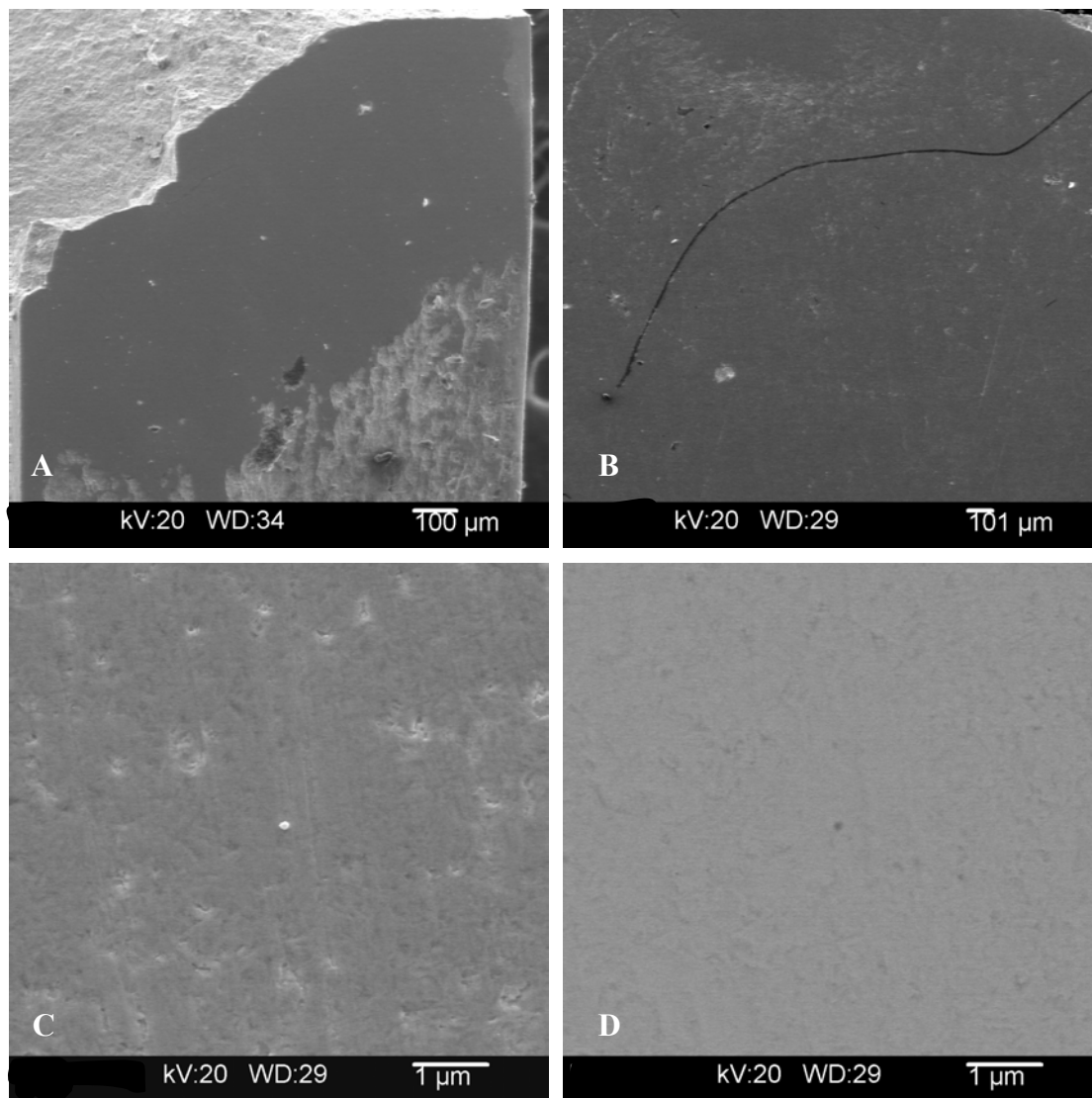


Figure 3.5. SEM micrographs of $\text{Bi}_2\text{Sr}_2\text{Nb}_2\text{TiO}_{12}$, polished face of hot pressed sample
A) SE image B) SE image of cracking caused by hot pressing C) SE image D) BSE image of image C.

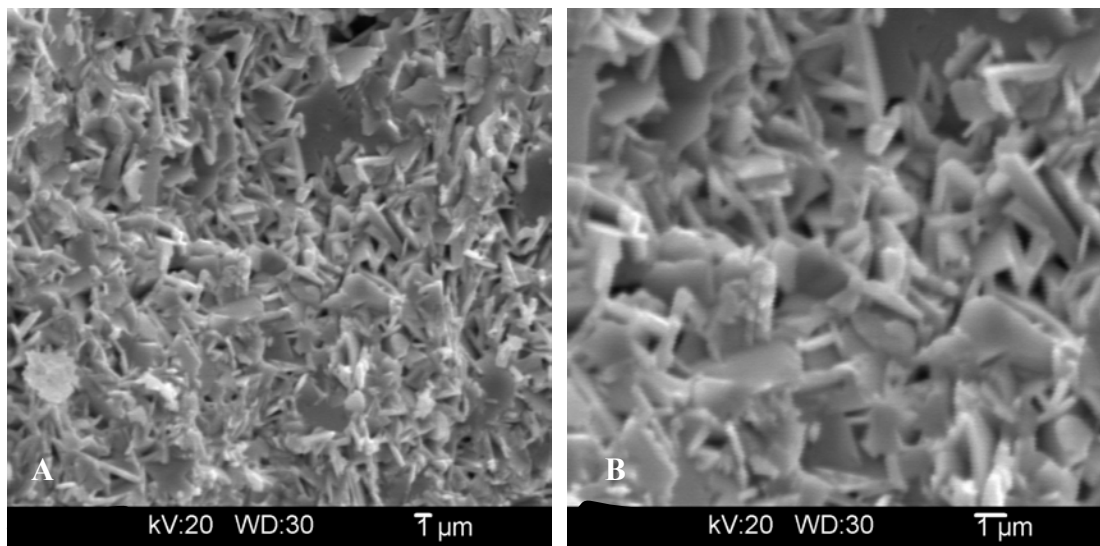


Figure 3.6. SEM micrographs of $\text{Bi}_2\text{Sr}_2\text{Nb}_2\text{TiO}_{12}$ fractured face of hot pressed sample. Both images are SE images.

3.2 Characterization of $\text{Bi}_2\text{Sr}_2\text{Nb}_2\text{Ti}_{(1-x)}\text{M}_x\text{O}_{12-\delta}$ ($x=0-1$, $\text{M}=\text{Co}, \text{Cr}, \text{Fe}, \text{Mn}$)

3.2.1 Synthesis of $\text{Bi}_2\text{Sr}_2\text{Nb}_2\text{Ti}_{(1-x)}\text{M}_x\text{O}_{12-\delta}$

Compositions of the family $\text{Bi}_2\text{Sr}_2\text{Nb}_2\text{Ti}_{(1-x)}\text{M}_x\text{O}_{12-\delta}$ ($x=0-1$, $\text{M}=\text{Co}, \text{Cr}, \text{Fe}, \text{Mn}$) were synthesized as described in Section 2.1.2. Phase purity was monitored after calcination at 900°C for 10 hours and after sintering pellets at 1050°C for 30 hours with x-ray diffraction. The phase purity results are shown in Table V.

Iron was successfully substituted into the structure at 50 atom%, chromium at 20 atom% and cobalt at 5 atom%. The diffraction patterns for all compounds listed in Table V are presented in Section 3.2.2. The trends seen in Table IIV can be explained by relating the substitutions to their ionic radii (Table II). When discussing ionic radii and substitutions, as a general rule of thumb a difference of more than 12% between the host site and the substitution typically does not result in phase purity.⁴⁹

Table V: Phase Purity Results Obtained for Transition Metal Series.

Composition	Phase Pure 900°C/10hrs	Phase Pure 1050°C/30hrs
$\text{Bi}_2\text{Sr}_2\text{Nb}_2\text{Ti}_{0.95}\text{Fe}_{0.05}\text{O}_{11.975}$	Yes	Yes
$\text{Bi}_2\text{Sr}_2\text{Nb}_2\text{Ti}_{0.9}\text{Fe}_{0.1}\text{O}_{11.95}$	Yes	Yes
$\text{Bi}_2\text{Sr}_2\text{Nb}_2\text{Ti}_{0.8}\text{Fe}_{0.2}\text{O}_{11.9}$	Yes	Yes
$\text{Bi}_2\text{Sr}_2\text{Nb}_2\text{Ti}_{0.5}\text{Fe}_{0.5}\text{O}_{11.75}$	Yes	Yes
$\text{Bi}_2\text{Sr}_2\text{Nb}_2\text{Ti}_{0.25}\text{Fe}_{0.75}\text{O}_{11.625}$	Yes	No
$\text{Bi}_2\text{Sr}_2\text{Nb}_2\text{FeO}_{11.5}$	No	No
$\text{Bi}_2\text{Sr}_2\text{Nb}_{1.5}\text{Fe}_{0.5}\text{Ti}_{0.5}\text{Fe}_{0.5}\text{O}_{11.5}$	No	No
$\text{Bi}_2\text{Sr}_2\text{Nb}_{1.3}\text{Fe}_{0.7}\text{Ti}_{0.5}\text{Fe}_{0.5}\text{O}_{11.35}$	No	No
$\text{Bi}_2\text{Sr}_2\text{Nb}_2\text{Ti}_{0.95}\text{Cr}_{0.05}\text{O}_{11.975}$	Yes	Yes
$\text{Bi}_2\text{Sr}_2\text{Nb}_2\text{Ti}_{0.9}\text{Cr}_{0.1}\text{O}_{11.95}$	Yes	Yes
$\text{Bi}_2\text{Sr}_2\text{Nb}_2\text{Ti}_{0.8}\text{Cr}_{0.2}\text{O}_{11.9}$	Yes	Yes
$\text{Bi}_2\text{Sr}_2\text{Nb}_2\text{Ti}_{0.5}\text{Cr}_{0.5}\text{O}_{11.75}$	No	No
$\text{Bi}_2\text{Sr}_2\text{Nb}_2\text{Ti}_{0.95}\text{Co}_{0.05}\text{O}_{11.975}$	Yes	Yes
$\text{Bi}_2\text{Sr}_2\text{Nb}_2\text{Ti}_{0.8}\text{Co}_{0.2}\text{O}_{11.9}$	Yes	No
$\text{Bi}_2\text{Sr}_2\text{Nb}_2\text{MnO}_{11.5}$	No	No

The trends in ionic radii presented in Table II follow the experimental evidence presented in Table V; more iron can be substituted than chromium, and more chromium can be substituted than cobalt. This also suggests that the transition metal substitutions prefer to be incorporated by the structure in the 4+ valence state, resisting the formation of charge carriers (holes or oxygen vacancies). Assuming the majority of the substitutions enter the structure in the 4+ state, the trends seen in phase purity (Table V) would be expected.

Those substitutions that are not a good match with titanium in the 4+ valence state can be substituted into the structure less, regardless of how good a match the ions are in other valence states. The data for the series of cobalt substitutions supports this

idea strongly, because cobalt is the best match to titanium of all the transition metals used in its 3+ state, and 12% different in the 4+ state, one would expect cobalt to substitute at higher level than what was observed, unless it does not assume the 3+ valence. Because substitutions incorporated into the structure at the same valence of titanium would not create charge carriers, a correlated can be made with the electrical characterization results in Section 3.2.3. It was hoped that the transition metal substitutions would substitute into the structure as a mixture a valences, some 3+ and some 4+, creating sites for polaron conduction, and increase the conductivity.

However, the phase purity results and the ionic radii trends suggest that the transition metals entered the structure primarily in the 4+ valence state. Although the transition metal would present a site to make polaron conduction easier (as it switches valence readily), if there are very few charge carrier sites in the structure (3+ on a 4+ site) then the conductivity would not be affected much. The conductivity data presented in Section 3.2.3 is a strong correlation to this speculation. For all of the transition metal compositions synthesized, there is not a noticeable difference between their conductivities. This is an indication that the substitutions were isovalent.

3.2.2 X-Ray Diffraction of $Bi_2Sr_2Nb_2Ti_{(1-x)}M_xO_{12-\delta}$

XRD was performed on all samples as described in Section 2.1.4. Figure 3.7 and Figure 3.8 show the diffraction patterns for M=Fe (x=0.05, 0.1, 0.2, 0.5) after sintering at either 900°C, 1050°C.

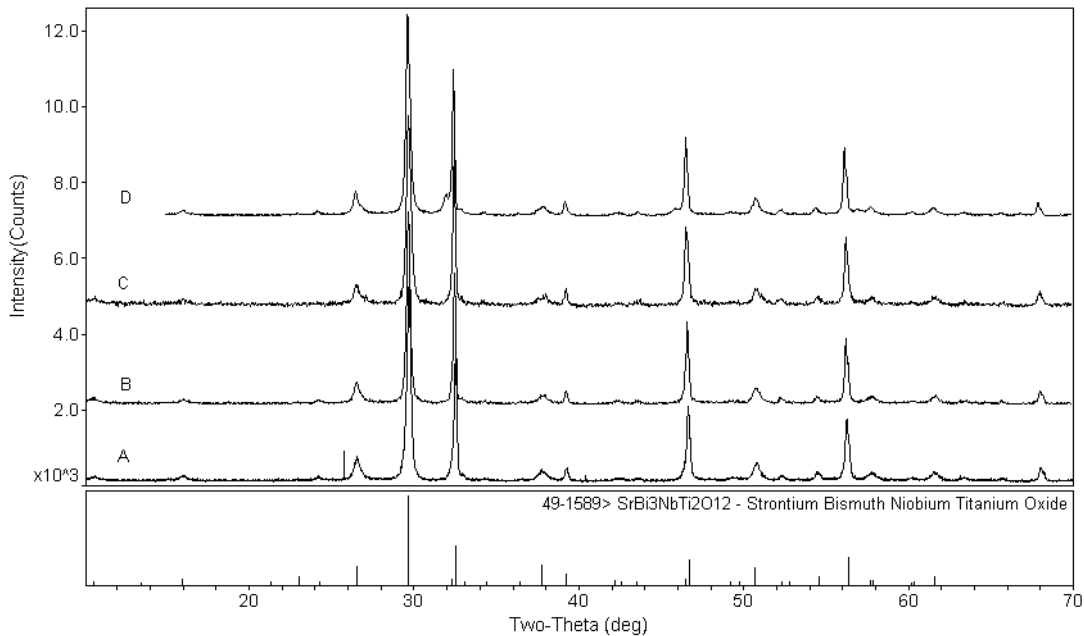


Figure 3.7. XRD pattern for $\text{Bi}_2\text{Sr}_2\text{Nb}_2\text{Ti}_{(1-x)}\text{Fe}_x\text{O}_{12}$ series post $900^\circ\text{C}/10\text{hrs}$, A) $x=0.05$, B) $x=0.1$, C) $x=0.2$, D) $x=0.5$. The sticks in the bottom of the figure represent the peak placement of the corresponding PDF cards..

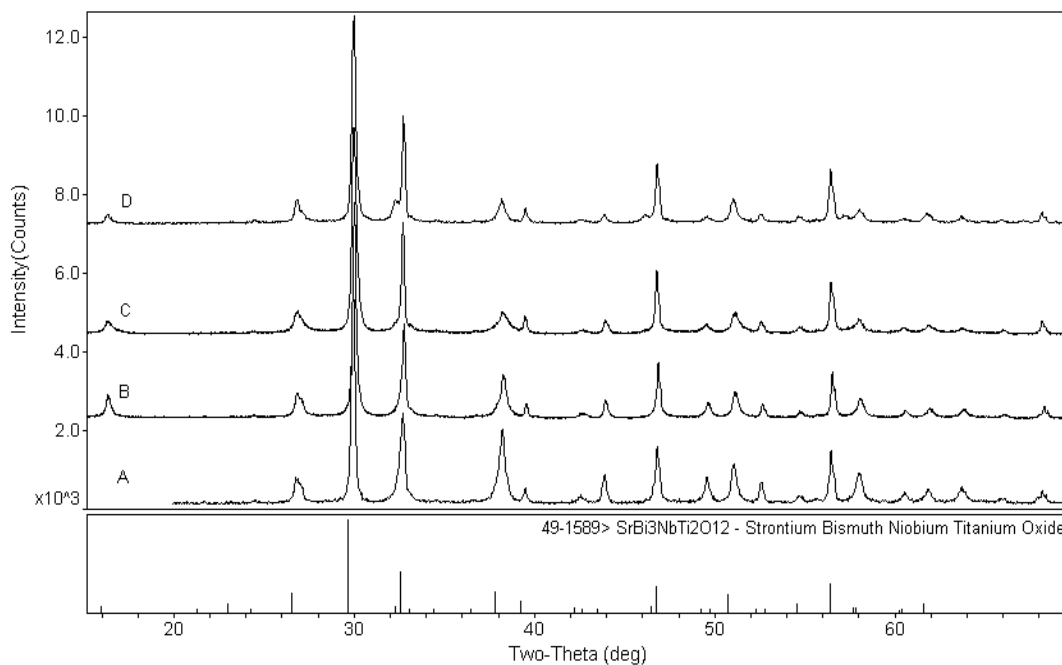


Figure 3.8. XRD pattern for $\text{Bi}_2\text{Sr}_2\text{Nb}_2\text{Ti}_{(1-x)}\text{Fe}_x\text{O}_{12}$ post $1050^\circ\text{C}/30\text{hrs}$, A) $x=0.05$, B) $x=0.1$, C) $x=0.2$, D) $x=0.5$. The sticks in the bottom of the figure represent the peak placement of the corresponding PDF cards.

Samples prepared with substitutions of iron for titanium were not phase pure above 50 atom% iron. A sample prepared with a substitution of 75 atom% iron was pure after calcination at 900°C for 10 hours, but upon sintering into a pellet a strontium iron oxide phase developed, as evident in Figure 3.9.

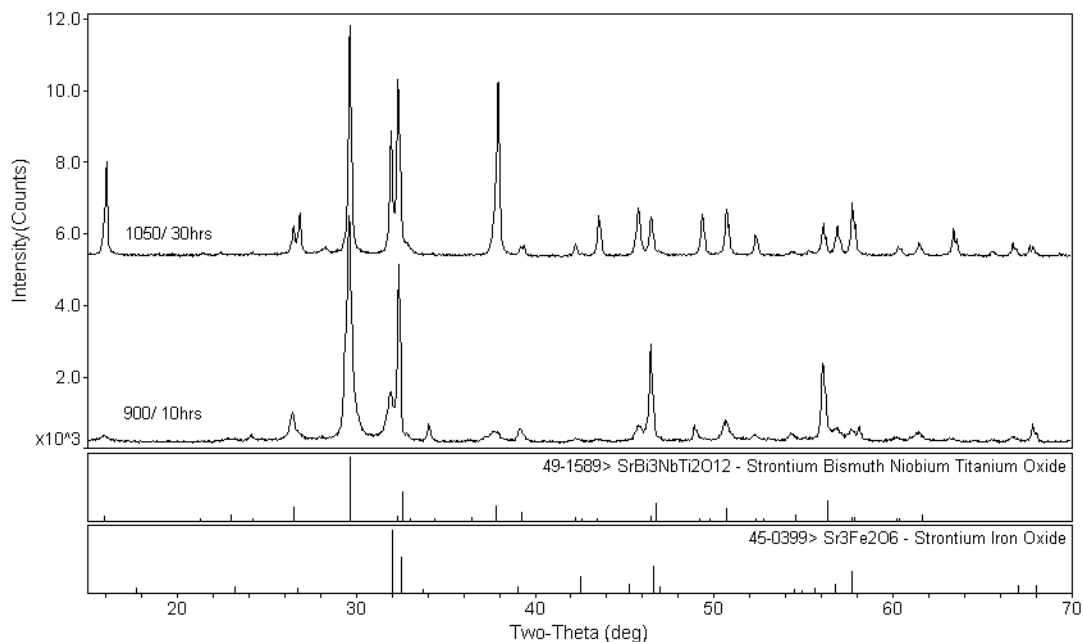


Figure 3.9. XRD patterns for $\text{Bi}_2\text{Sr}_2\text{Nb}_2\text{Ti}_{0.25}\text{Fe}_{0.75}\text{O}_{12-\delta}$ post 900°C/10hrs and 1050°C/30hrs. The sticks in the bottom of the figure represent the peak placement of the corresponding PDF cards.

A sample prepared with a full substitution of iron for titanium contained a strontium-iron phase after calcination at 900°C for 10 hours, which remained after sintering into a pellet, as evident in Figure 3.10.

Sample prepared with substitutions of chromium for titanium were phase pure up to 20 atom% chromium. The diffraction patterns for $\text{Bi}_2\text{Sr}_2\text{Nb}_2\text{Ti}_{0.95}\text{Cr}_{0.05}\text{O}_{11.975}$ and $\text{Bi}_2\text{Sr}_2\text{Nb}_2\text{Ti}_{0.9}\text{Cr}_{0.1}\text{O}_{11.95}$ and $\text{Bi}_2\text{Sr}_2\text{Nb}_2\text{Ti}_{0.8}\text{Cr}_{0.2}\text{O}_{11.9}$ are shown in Figure 3.11 and Figure 3.12, respectively. Both XRD plots show patterns for the samples after calcination at 900°C for 10hrs and after sintering at 1050°C for 30hrs.

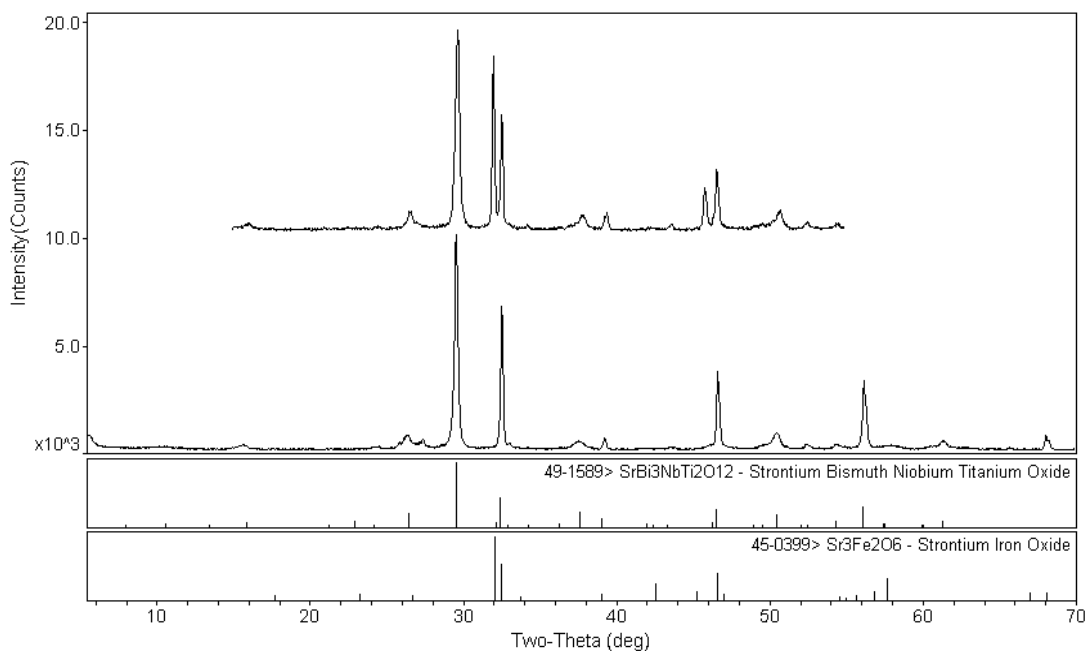


Figure 3.10. XRD patterns for $\text{Bi}_2\text{Sr}_2\text{Nb}_2\text{FeO}_{11.5}$ post $900^\circ\text{C}/10\text{hrs}$ and $1050^\circ\text{C}/30\text{hrs}$. The sticks in the bottom of the figure represent the peak placement of the corresponding PDF cards.

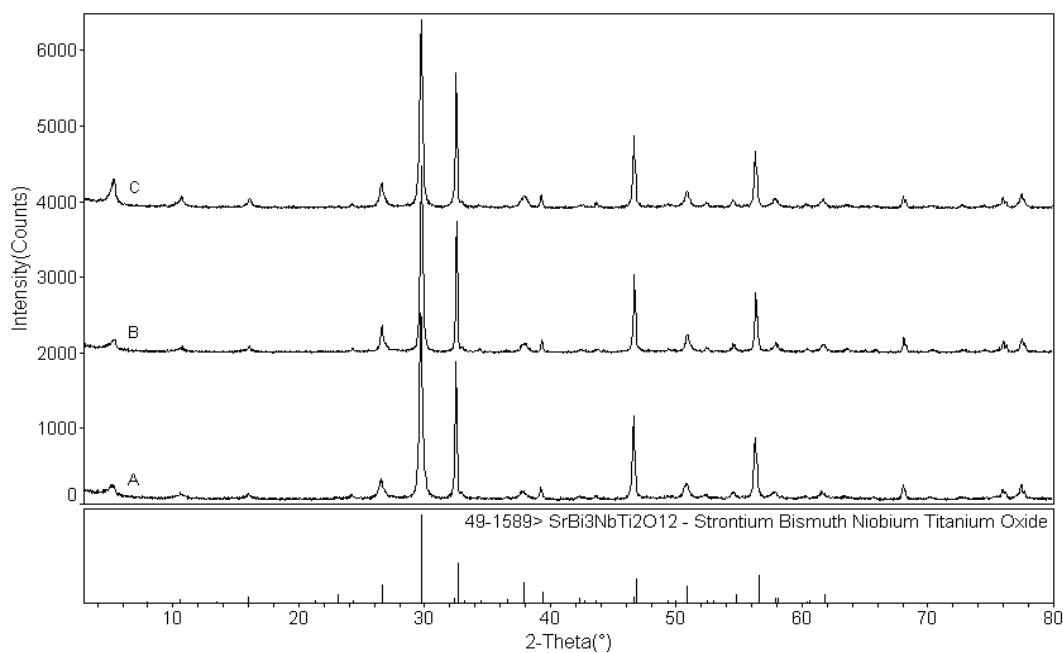


Figure 3.11. XRD patterns for $\text{Bi}_2\text{Sr}_2\text{Nb}_2\text{Ti}_{(1-x)}\text{Cr}_x\text{O}_{12-\delta}$ post $900^\circ\text{C}/10\text{hrs}$ A) $x=0.05$, B) $x=0.1$, C) $x=0.2$. The sticks in the bottom of the figure represent the peak placement of the corresponding PDF cards.

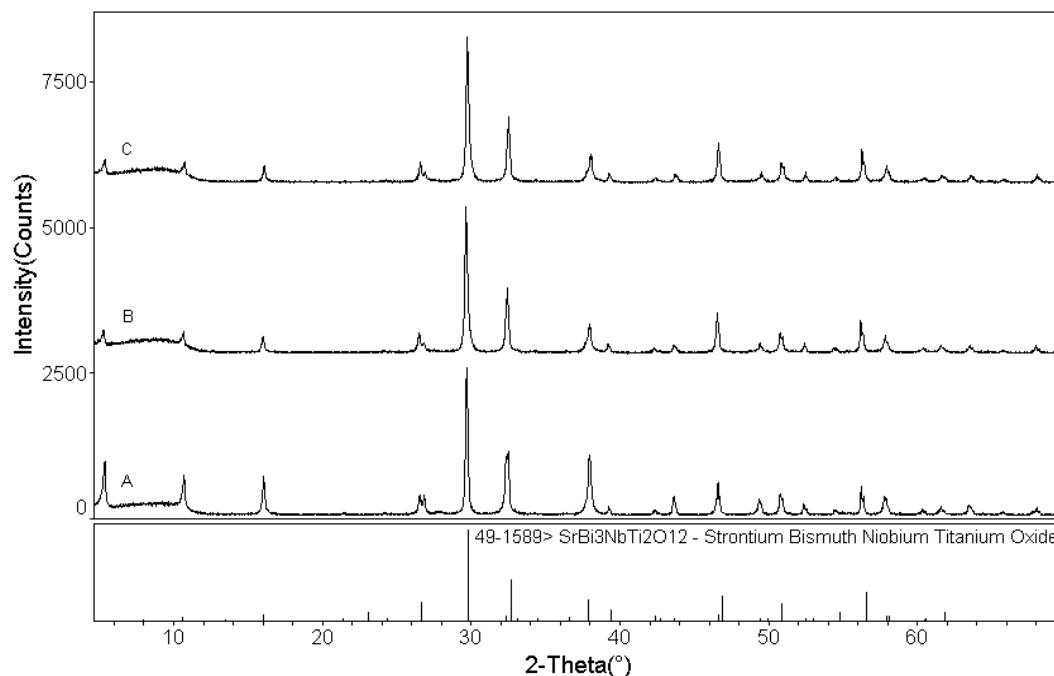


Figure 3.12. XRD patterns for $\text{Bi}_2\text{Sr}_2\text{Nb}_2\text{Ti}_{(1-x)}\text{Cr}_x\text{O}_{12-\delta}$ post $1050^\circ\text{C}/30\text{hrs}$ the amorphous hump seen below $10^\circ 2\theta$ is from the sample holder. A) $x=0.05$, B) $x=0.1$, C) $x=0.2$. The sticks in the bottom of the figure represent the peak placement of the corresponding PDF cards.

Samples prepared with chromium substitutions of 50 atom% were impure, resulting in the formation of a bismuth-chromium oxide phase and a strontium titanate phase along with the Aurivillius phase. The diffraction pattern for $\text{Bi}_2\text{Sr}_2\text{Nb}_2\text{Ti}_{0.5}\text{Cr}_{0.5}\text{O}_{12-\delta}$ after calcination at 900°C for 10hrs is shown in Figure 3.13.

Samples with cobalt substitutions were phase pure at 5 atom% cobalt, as shown in Figure 3.14, yet cobalt substituted for titanium at 20 atom% was not phase pure. As shown in the diffraction pattern in Figure 3.15, $\text{Bi}_2\text{Sr}_2\text{Nb}_2\text{Ti}_{0.8}\text{Co}_{0.2}\text{O}_{11.75}$ was phase pure after calcination at 900°C , yet upon sintering at 1050°C for 30hrs, a bismuth oxide phase develops.

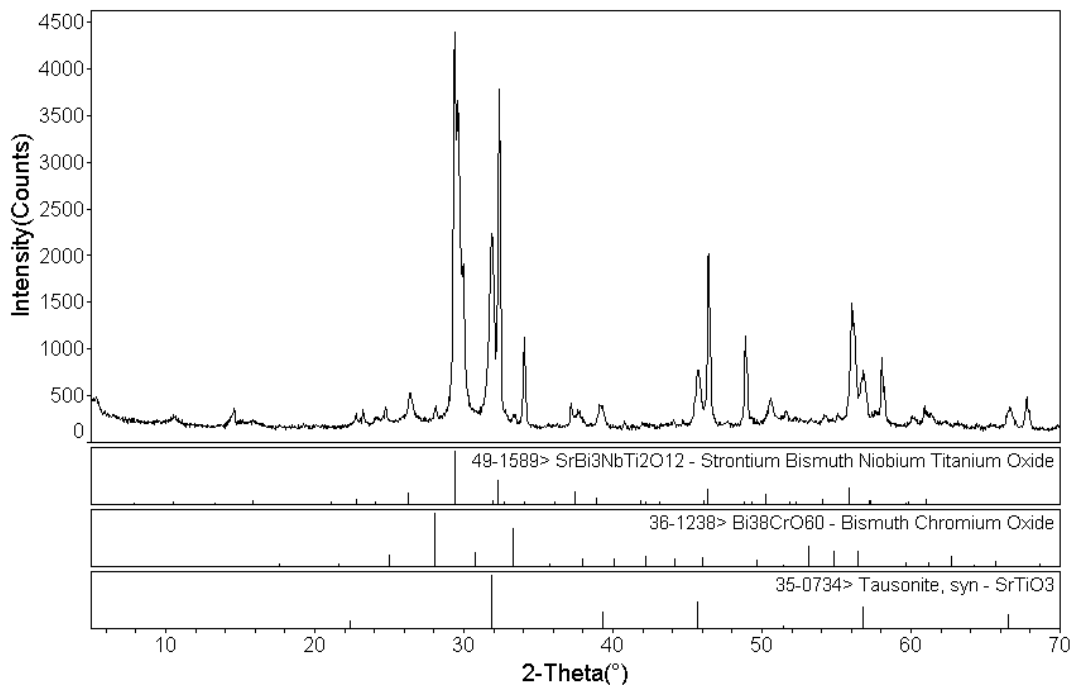


Figure 3.13. XRD pattern for $\text{Bi}_2\text{Sr}_2\text{Nb}_2\text{Ti}_{0.5}\text{Cr}_{0.5}\text{O}_{11.75}$ post $900^\circ\text{C}/10\text{hrs}$. The sticks in the bottom of the figure represent the peak placement of the corresponding PDF cards.

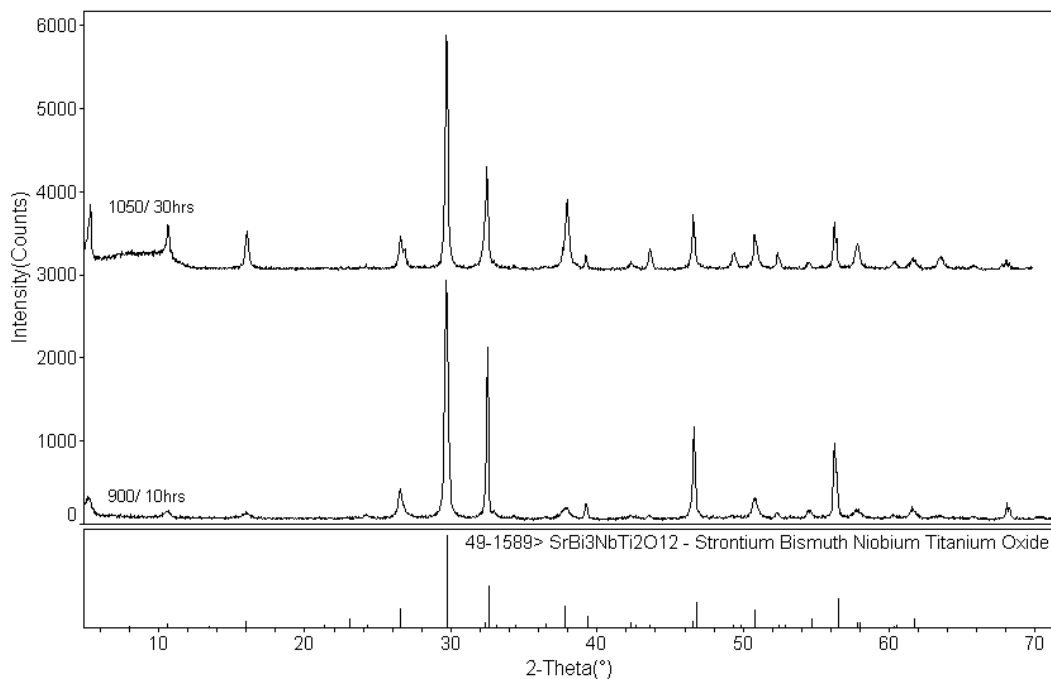


Figure 3.14. XRD patterns for $\text{Bi}_2\text{Sr}_2\text{Nb}_2\text{Ti}_{0.95}\text{Co}_{0.05}\text{O}_{11.975}$ post calcination and sintering. The sticks in the bottom of the figure represent the peak placement of the corresponding PDF cards.

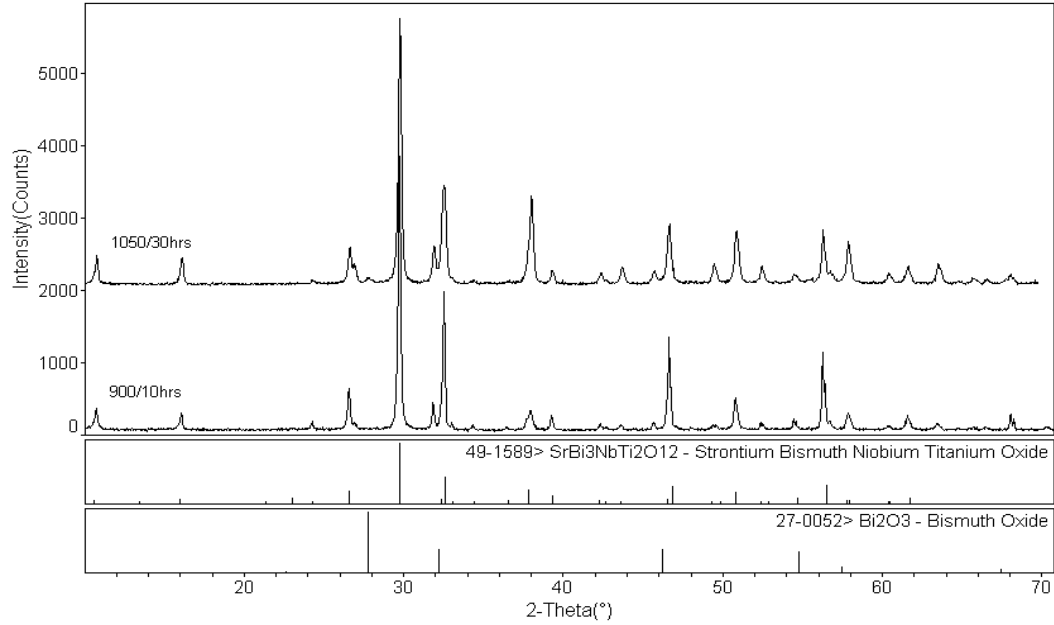


Figure 3.15. XRD pattern for $\text{Bi}_2\text{Sr}_2\text{Nb}_2\text{Ti}_{0.8}\text{Co}_{0.2}\text{O}_{11.9}$ post calcination and sintering. The sticks in the bottom of the figure represent the peak placement of the corresponding PDF cards.

A paper by Yu et. al.⁵¹ stated that titanium could be fully substituted with manganese ($\text{Bi}_2\text{Sr}_2\text{Nb}_2\text{MnO}_{11.5}$). This was attempted in this study, however phase purity was not obtained. The diffraction pattern for $\text{Bi}_2\text{Sr}_2\text{Nb}_2\text{MnO}_{11.5}$ after calcination at 900°C for 10hrs, Figure 3.16, shows the presence of a manganese stabilized bismuth-oxide phase as well as the Aurivillius phase.

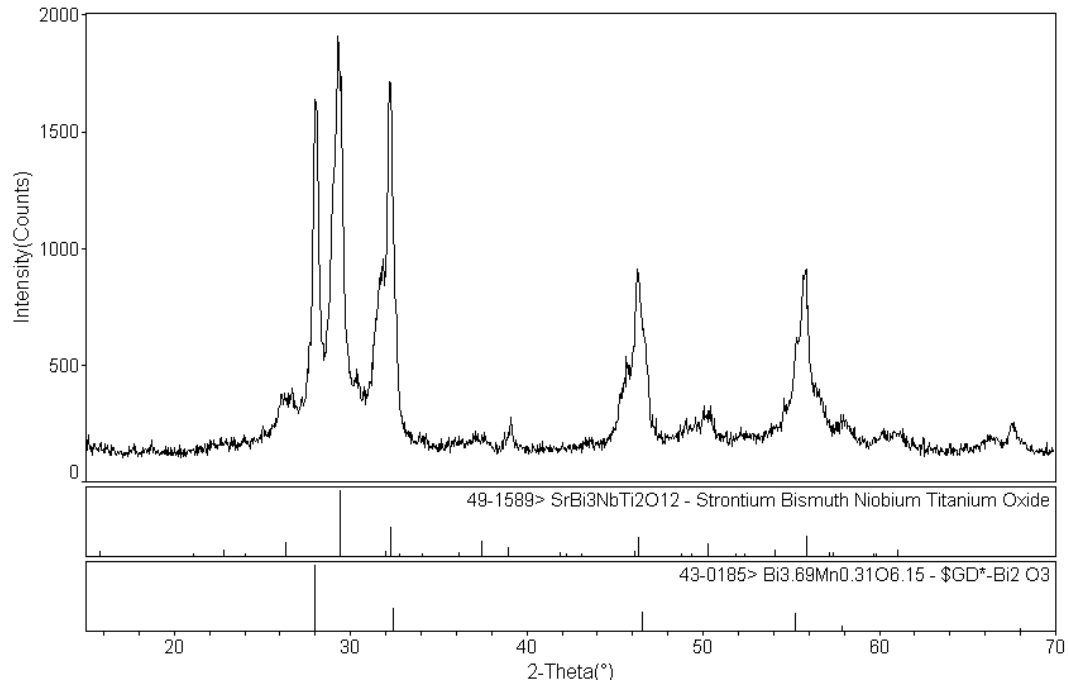


Figure 3.16. XRD pattern for $\text{Bi}_2\text{Sr}_2\text{Nb}_2\text{MnO}_{11.5}$ post 900/10hrs. The sticks in the bottom of the figure represent the peak placement of the corresponding PDF cards.

3.2.3 Electrical Characterization of $\text{Bi}_2\text{Sr}_2\text{Nb}_2\text{Ti}_{(1-x)}\text{M}_x\text{O}_{12-\delta}$ ($x=0-1$, $M=\text{Co}, \text{Cr}, \text{Fe}$)

The addition of transition metals to the parent phase $\text{Bi}_2\text{Sr}_2\text{Nb}_2\text{TiO}_{12}$ did not increase the conductivity significantly. The largest increases in conductivity were seen with the iron-substituted samples.

3.2.3.1 AC Conductivity of $\text{Bi}_2\text{Sr}_2\text{Nb}_2\text{Ti}_{(1-x)}\text{Fe}_x\text{O}_{12-\delta}$

Table VI and Figure 3.17 show the conductivity data for the iron substituted series $\text{Bi}_2\text{Sr}_2\text{Nb}_2\text{Ti}_{(1-x)}\text{Fe}_x\text{O}_{12-\delta}$. All conductivity data was normalized to the sample with the highest density within the iron series. Dividing the density of each sample by the highest density obtained within the series accomplished this. The sample $\text{Bi}_2\text{Sr}_2\text{Nb}_2\text{Ti}_{0.8}\text{Fe}_{0.2}\text{O}_{12-\delta}$ had the highest conductivity, however the spread in the data was under 10%, so no significant increases in conductivity were obtained upon increased iron substitution.

Table VI: Conductivity and Activation Energies for $\text{Bi}_2\text{Sr}_2\text{Nb}_2\text{Ti}_{(1-x)}\text{Fe}_x\text{O}_{12-\delta}$.

$\text{Bi}_2\text{Sr}_2\text{Nb}_2\text{Ti}_{(1-x)}\text{Fe}_x\text{O}_{12-\delta}$					
x	Conductivity @ 950°C (S/cm)	E_{a3} (>850°C)	E_{a2} (400-850°C)	Theoretical Density (g/cm ³)	% Theoretical Density
0	-3.1	1.4	0.9	6.731	52.6
0.05	-2.88	0.6	1	6.734	60.5
0.1	-2.85	0.7	1.2	6.736	68
0.2	-2.59	0.5	0.8	6.742	62.2
0.5	-2.55	1	1	6.757	52.7

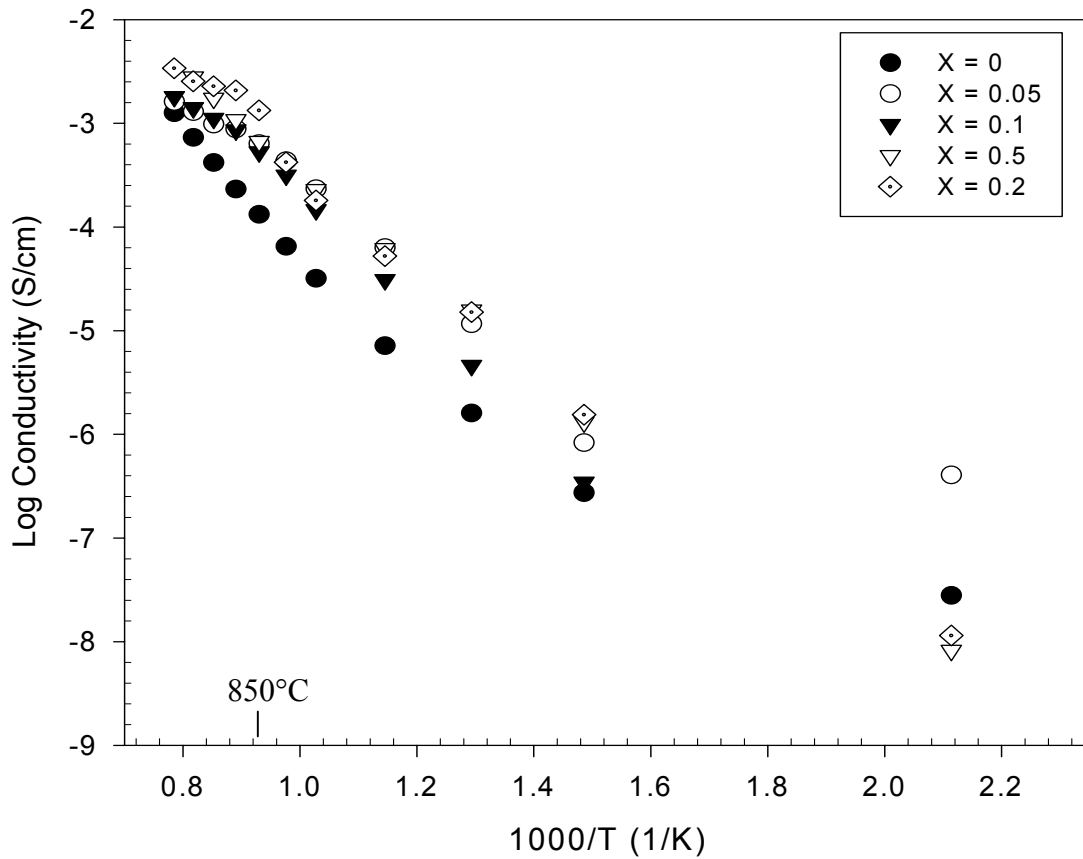


Figure 3.17. Conductivity data for from $\text{Bi}_2\text{Sr}_2\text{Nb}_2\text{Ti}_{(1-x)}\text{Fe}_x\text{O}_{12-\delta}$ 200-1000°C.

All Cole-Cole plots for the iron series were similar to those shown in Figure 3.18. The Cole-Cole plots appear as depressed semi-circles because the grain and grain boundary responses are not separated, instead they appear as one elongated arc at the high frequency (left) end of the plot. Although all sample conductivity values were normalized to density, the density could explain the shape of the Cole-Cole plots in Figure 3.18. A lower density could increase the grain boundary response.

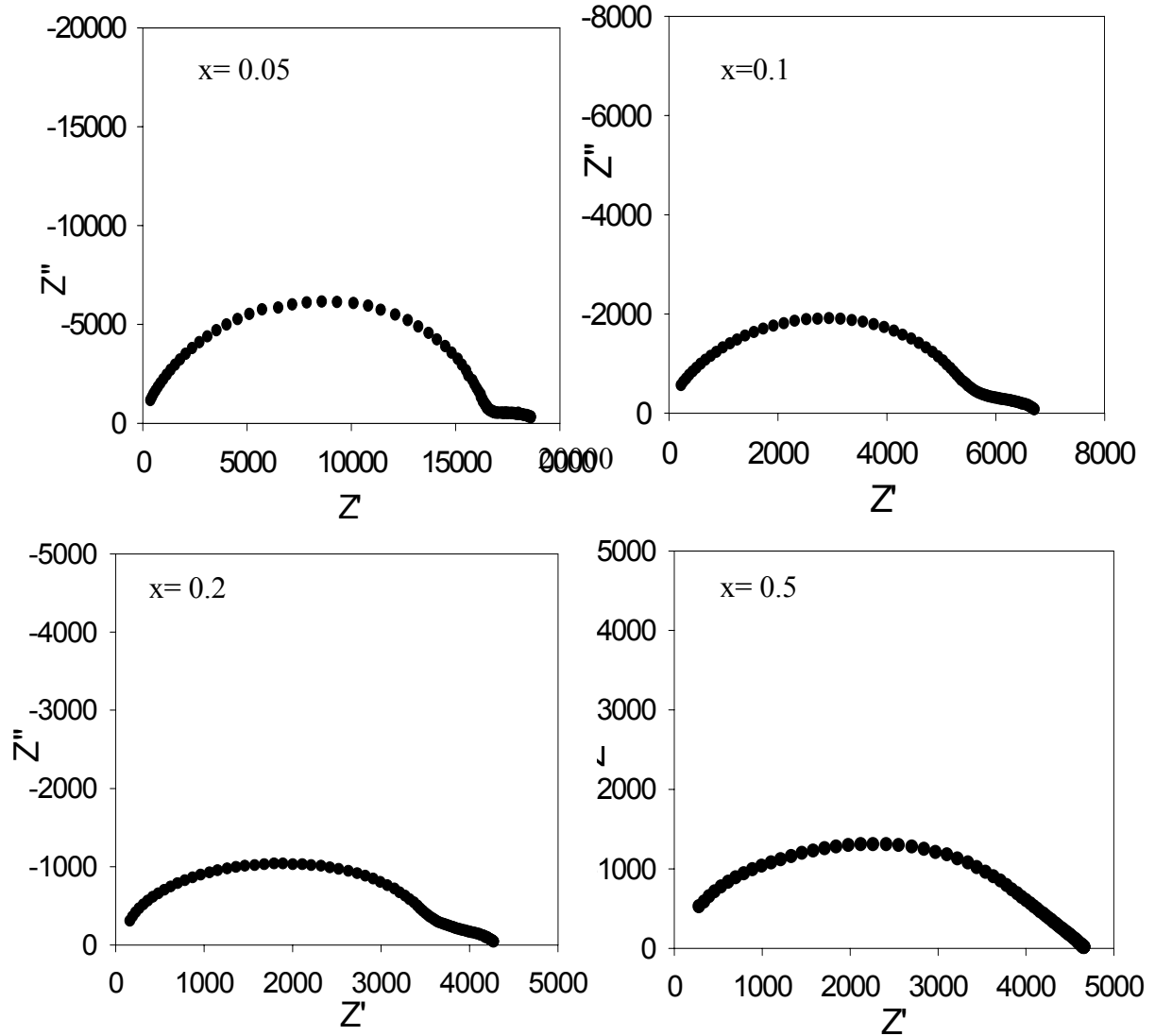


Figure 3.18. Cole-Cole plots for $\text{Bi}_2\text{Sr}_2\text{Nb}_2\text{Ti}_{(1-x)}\text{Fe}_x\text{O}_{12-\delta}$, at 600°C , with iron substitution levels listed in the plot window.

3.2.3.2 AC Conductivity of $\text{Bi}_2\text{Sr}_2\text{Nb}_2\text{Ti}_{(1-x)}\text{Cr}_x\text{O}_{12-\delta}$

Table VII and Figure 3.19 show the conductivity data for the chromium substituted series $\text{Bi}_2\text{Sr}_2\text{Nb}_2\text{Ti}_{(1-x)}\text{Cr}_x\text{O}_{12-\delta}$. All conductivity was normalized to the density of the sample with the highest density within the chromium series. The samples did not differ distinctly with respect to conductivity. The error in the data was under 8%. The Cole-Cole plots for the chromium substituted samples were the same in appearance to those presented for the iron series in Figure 3.18.

Table VII: Conductivity and Activation Energies for $\text{Bi}_2\text{Sr}_2\text{Nb}_2\text{Ti}_{(1-x)}\text{Cr}_x\text{O}_{12-\delta}$.

$\text{Bi}_2\text{Sr}_2\text{Nb}_2\text{Ti}_{(1-x)}\text{Cr}_x\text{O}_{12-\delta}$					
x	Conductivity @ 950°C (S/cm)	E_{a_3} (>850°C) eV	E_{a_2} (400- 850°C) eV	Theoretical Density (g/cm ³)	% Theoretical Density
0	-3.10	1.4	0.9	6.731	52.6
0.05	-2.69	0.6	1	6.732	82
0.1	-2.73	1	1	6.734	73
0.2	-2.72	0.7	1.2	6.737	71

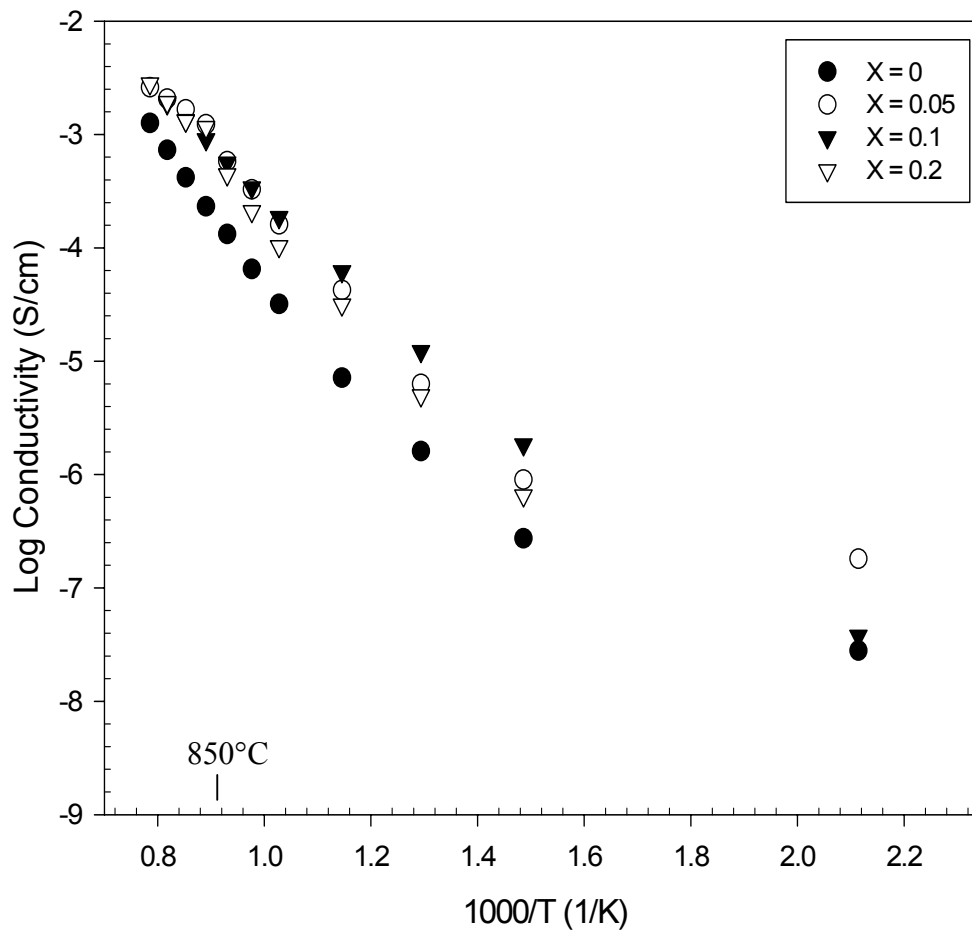


Figure 3.19. Conductivity data for $\text{Bi}_2\text{Sr}_2\text{Nb}_2\text{Ti}_{(1-x)}\text{Cr}_x\text{O}_{12-\delta}$ from 200-1000°C.

3.2.3.3 AC Conductivity of $\text{Bi}_2\text{Sr}_2\text{Nb}_2\text{Ti}_{0.95}\text{Co}_{0.05}\text{O}_{12-\delta}$

Table VIII and Figure 3.20 show the conductivity data for the cobalt-substituted sample $\text{Bi}_2\text{Sr}_2\text{Nb}_2\text{Ti}_{0.95}\text{Co}_{0.05}\text{O}_{12-\delta}$. The two samples were normalized for density. The cobalt sample's conductivity showed a slight improvement over the parent phase; however, as stated previously the spread in the data was under 8%, making this conclusion less definitive.

Table VIII: Conductivity and Activation Energies for $\text{Bi}_2\text{Sr}_2\text{Nb}_2\text{Ti}_{0.95}\text{Co}_{0.05}\text{O}_{12-\delta}$.

$\text{Bi}_2\text{Sr}_2\text{Nb}_2\text{Ti}_{0.95}\text{Co}_{0.05}\text{O}_{12-\delta}$					
x	Conductivity @ 950°C (S/cm)	E_{a3} (>850°C) eV	E_{a2} (400- 850°C) eV	Theoretical Density (g/cm ³)	% Theoretical Density
0	-3.1	1.4	0.9	6.731	52.6
0.05	-2.97	0.75	1.2	6.735	62.7

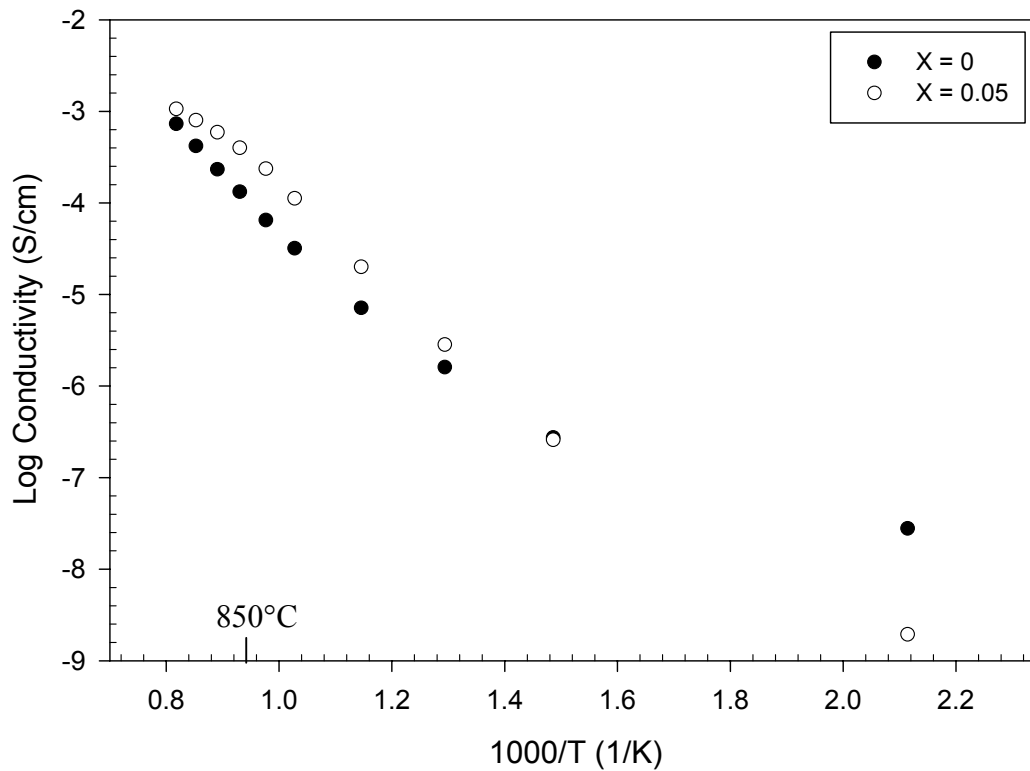


Figure 3.20. Conductivity for $\text{Bi}_2\text{Sr}_2\text{Nb}_2\text{Ti}_{0.95}\text{Co}_{0.05}\text{O}_{12-\delta}$ from 200-1000°C.

It is clear from the Arrhenius conductivity plots presented in Figure 3.17, Figure 3.19, and Figure 3.20 that there are multiple activation energy regions in the plots for the transition metal samples. In almost all samples there is a region from 200-400°C that has very low activation energy, which is characteristic of an extrinsic type region.

This data was not included in the conductivity tables because it would be based on only two points and would therefore have a large amount of error associated with it. All the samples then display an activation energy of about 1 eV from 400°C up to 850°C (and continues if the third region is not present), which is characteristic of an intrinsic type region.

The transition metal substituted samples display a high temperature activation energy region above 850°C that is less than 1 eV. Although the cause for this slope change is unknown, it indicates that the transition metal substitutions are having some effect on the conduction of the sample.

3.2.4 Microstructural characterization of $\text{Bi}_2\text{Sr}_2\text{Nb}_2\text{Ti}_{(1-x)}\text{M}_x\text{O}_{12-\delta}$ ($M=\text{Fe}, \text{Cr}$)

Scanning electron microscope images were taken to check phase purity with backscatter electron imaging, and look at the microstructure characteristics with secondary electron imaging.

The microstructure and measurements show that small amounts of substitution of iron for titanium ($x=0.05, 0.1$) increased the sintered density of samples (to 65-70% theoretical). However for samples with higher iron levels, ($x=0.2, 0.5$) the sintered density approaches that of the parent phase, or about 55 percent of the theoretical value. This trend (Figure 3.21) can be observed in Figure 3.22, which is SEM images obtained for both $\text{Bi}_2\text{Sr}_2\text{Nb}_2\text{Ti}_{0.80}\text{Fe}_{0.20}\text{O}_{12-\delta}$ and $\text{Bi}_2\text{Sr}_2\text{Nb}_2\text{Ti}_{0.50}\text{Fe}_{0.50}\text{O}_{12-\delta}$.

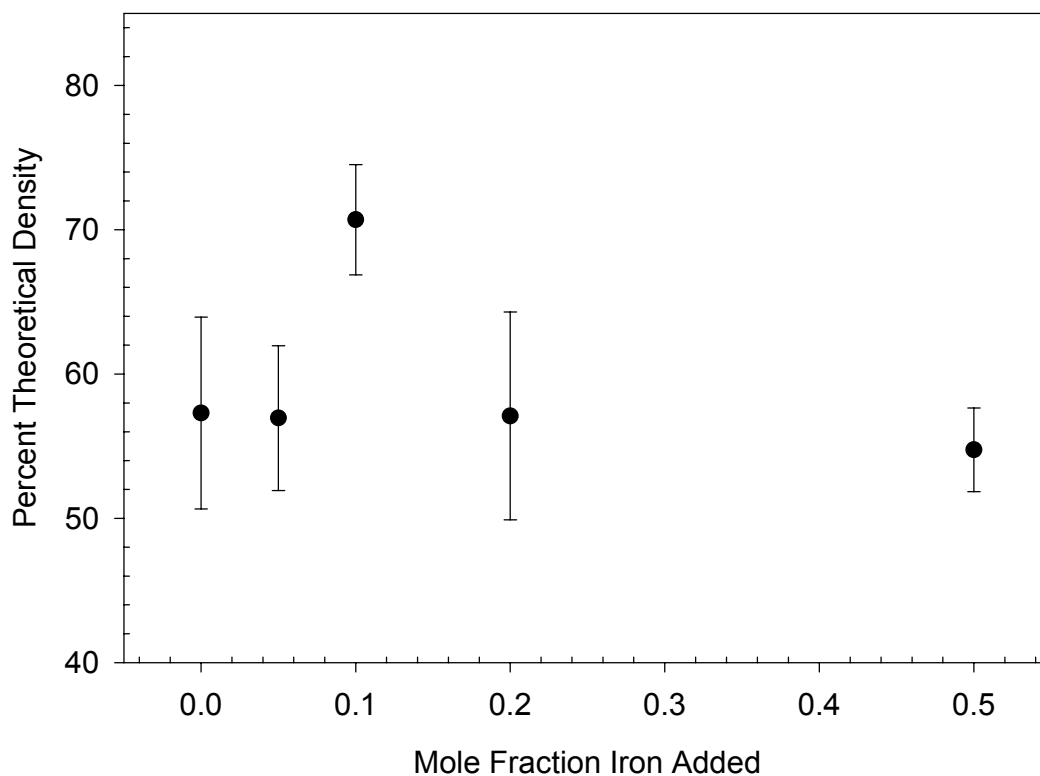


Figure 3.21. Percent of theoretical density of conductivity disks from series $\text{Bi}_2\text{Sr}_2\text{Nb}_2\text{Ti}_{(1-x)}\text{Fe}_x\text{O}_{12-\delta}$ ($x=0, 0.5, 0.1, 0.2, 0.5$) as a function of added iron. The data has been fit to a Spline curve.

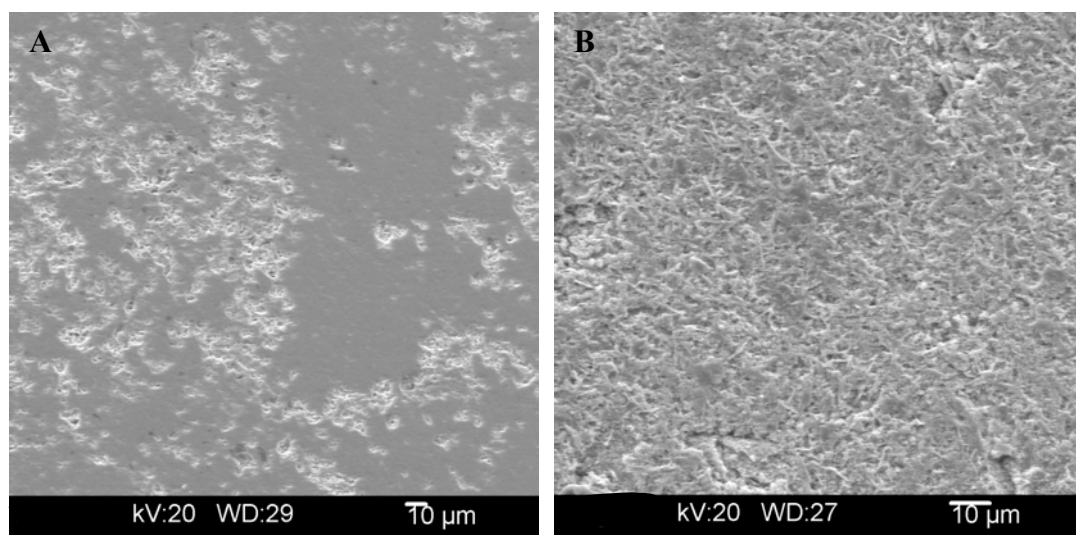


Figure 3.22. SE SEM images for both A) $\text{Bi}_2\text{Sr}_2\text{Nb}_2\text{Ti}_{0.80}\text{Fe}_{0.20}\text{O}_{12-\delta}$ and B) $\text{Bi}_2\text{Sr}_2\text{Nb}_2\text{Ti}_{0.50}\text{Fe}_{0.50}\text{O}_{12-\delta}$.

3.2.4.1 Microstructure of $\text{Bi}_2\text{Sr}_2\text{Nb}_2\text{Ti}_{0.95}\text{Fe}_{0.05}\text{O}_{12-\delta}$

SEM images obtained for $\text{Bi}_2\text{Sr}_2\text{Nb}_2\text{Ti}_{0.95}\text{Fe}_{0.05}\text{O}_{12-\delta}$ are shown in

Figure 3.23. Images are of a polished pellet face, even though there were visible black spots on the pellet surface, they are not visible as a compositional difference in the BSE images or with EDS analysis. This means that the spots are not a major compositional difference from the parent phase of the pellet. The small black spots that are visible in the BSE image are pieces of the polishing paper lodged in the pores of the pellet. Notice the higher density evident when compared with SEM images of the parent phase in Figure 3.4. A homogeneous BSE image is a confirmation of phase purity determined from diffraction in Figure 3.8.

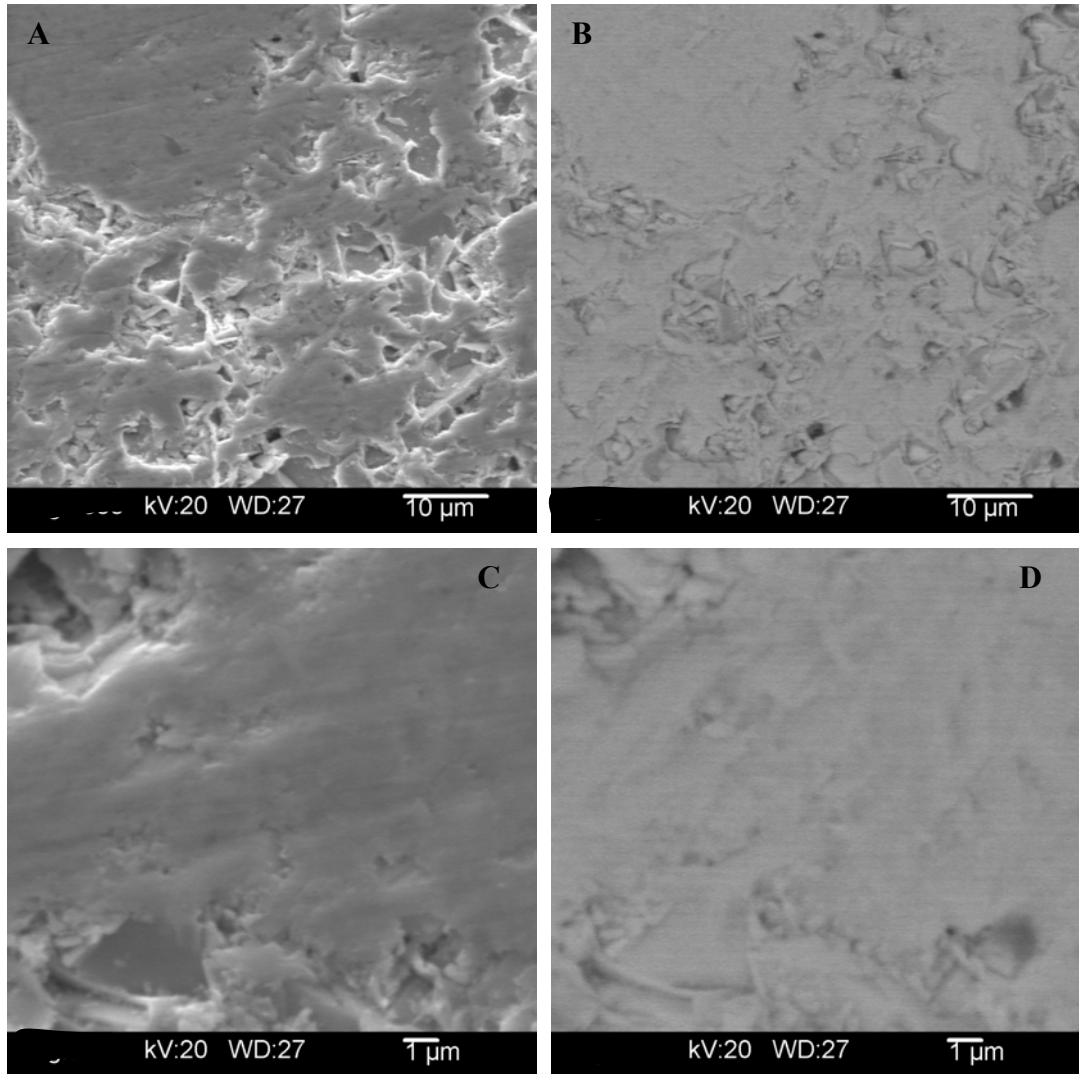


Figure 3.23. SEM images of $\text{Bi}_2\text{Sr}_2\text{Nb}_2\text{Ti}_{0.95}\text{Fe}_{0.05}\text{O}_{11.975}$. A and C are SE images; B and D are the corresponding BSE images.

3.2.4.2 Microstructure of $\text{Bi}_2\text{Sr}_2\text{Nb}_2\text{Ti}_{0.50}\text{Fe}_{0.50}\text{O}_{12-\delta}$

SEM images obtained for $\text{Bi}_2\text{Sr}_2\text{Nb}_2\text{Ti}_{0.50}\text{Fe}_{0.50}\text{O}_{12-\delta}$ are shown in Figure 3.24. Once again images are of a polished pellet face. Note the high level of porosity, much more than all of the other compositions within the iron series. The image closely resembles the parent phase in Figure 3.4 because of the low density. Yet again a homogeneous BSE image is a confirmation of phase purity determined from diffraction in Figure 3.8.

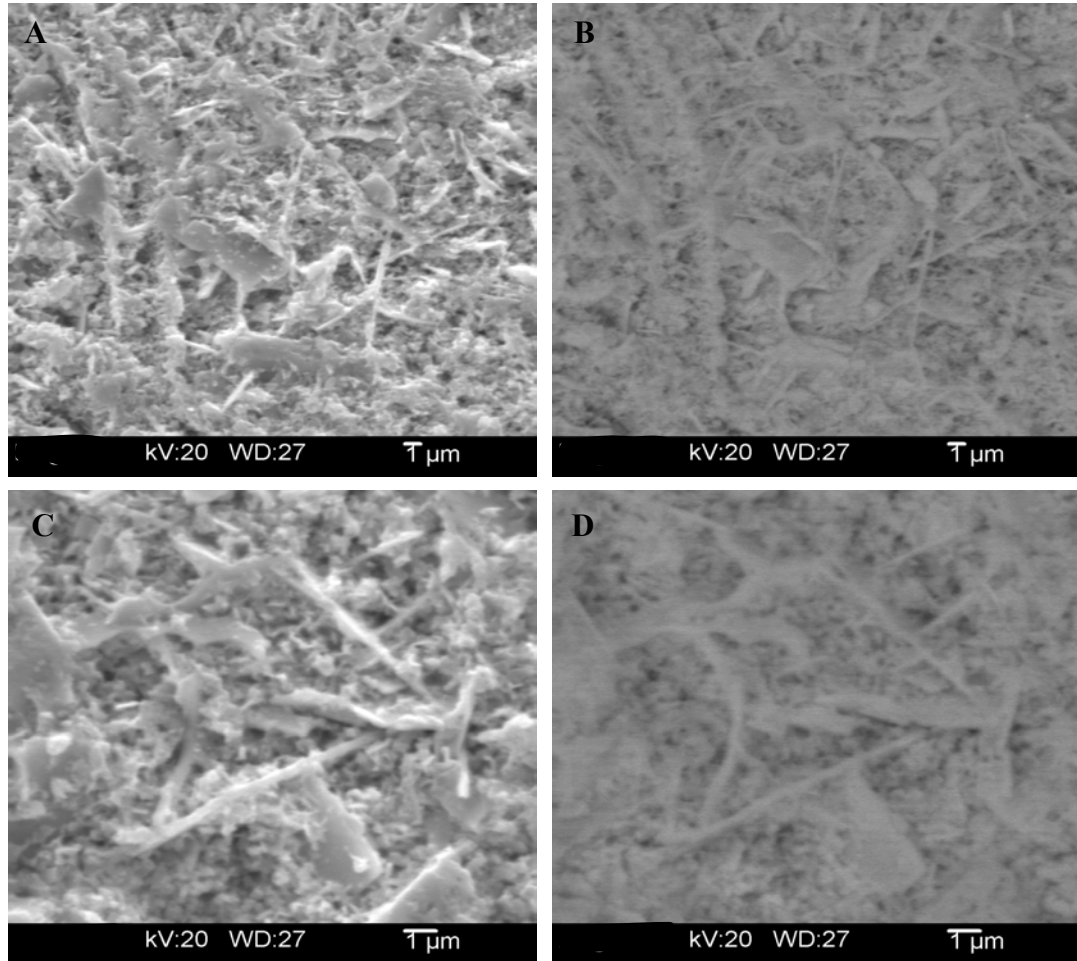


Figure 3.24. SEM images of $\text{Bi}_2\text{Sr}_2\text{Nb}_2\text{Ti}_{0.50}\text{Fe}_{0.50}\text{O}_{12-\delta}$ A and C are SE images; B and D are BSE images.

3.2.4.3 Microstructure of $\text{Bi}_2\text{Sr}_2\text{Nb}_2\text{Ti}_{0.8}\text{Cr}_{0.2}\text{O}_{12-\delta}$

The microstructure of all the chromium samples ($\text{Bi}_2\text{Sr}_2\text{Nb}_2\text{Ti}_{(1-x)}\text{Cr}_x\text{O}_{12-\delta}$ ($x=0.05, 0.1, 0.2$)) was similar to those of the iron substituted samples $\text{Bi}_2\text{Sr}_2\text{Nb}_2\text{Ti}_{(1-x)}$

x) $\text{Fe}_x\text{O}_{12-\delta}$ ($x=0, 0.5, 0.1, 0.2, 0.5$). All chromium samples had about the same density, which ranged from 72-82% theoretical, and were phase pure with no secondary phases. The $\text{Bi}_2\text{Sr}_2\text{Nb}_2\text{Ti}_{0.95}\text{Cr}_{0.05}\text{O}_{12-\delta}$ sample was the densest of all samples synthesized at 82% theoretical. The SEM images obtained for $\text{Bi}_2\text{Sr}_2\text{Nb}_2\text{Ti}_{0.8}\text{Cr}_{0.2}\text{O}_{12-\delta}$ are shown in Figure 3.26. The density values for $\text{Bi}_2\text{Sr}_2\text{Nb}_2\text{Ti}_{(1-x)}\text{Cr}_x\text{O}_{12-\delta}$ are plotted as a function of chromium additions in Figure 3.25.

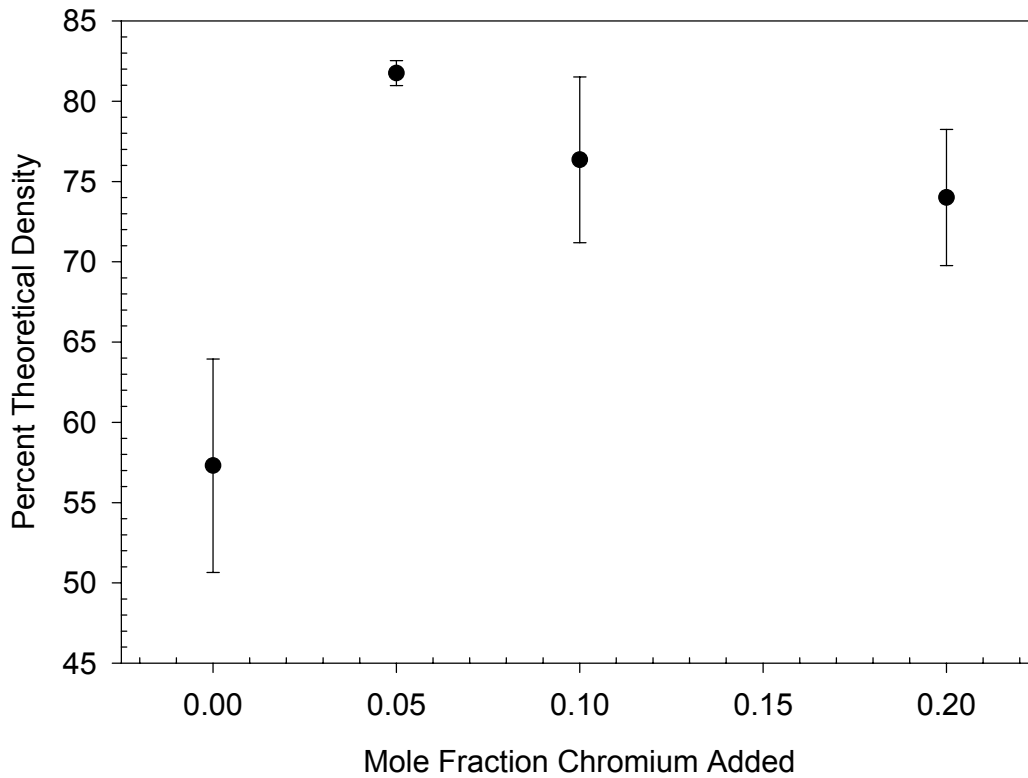


Figure 3.25. Percent of theoretical density of conductivity disks from series $\text{Bi}_2\text{Sr}_2\text{Nb}_2\text{Ti}_{(1-x)}\text{Cr}_x\text{O}_{12-\delta}$ ($x=0,0.5,0.1,0.2$). The data is fit with a Spline curve.

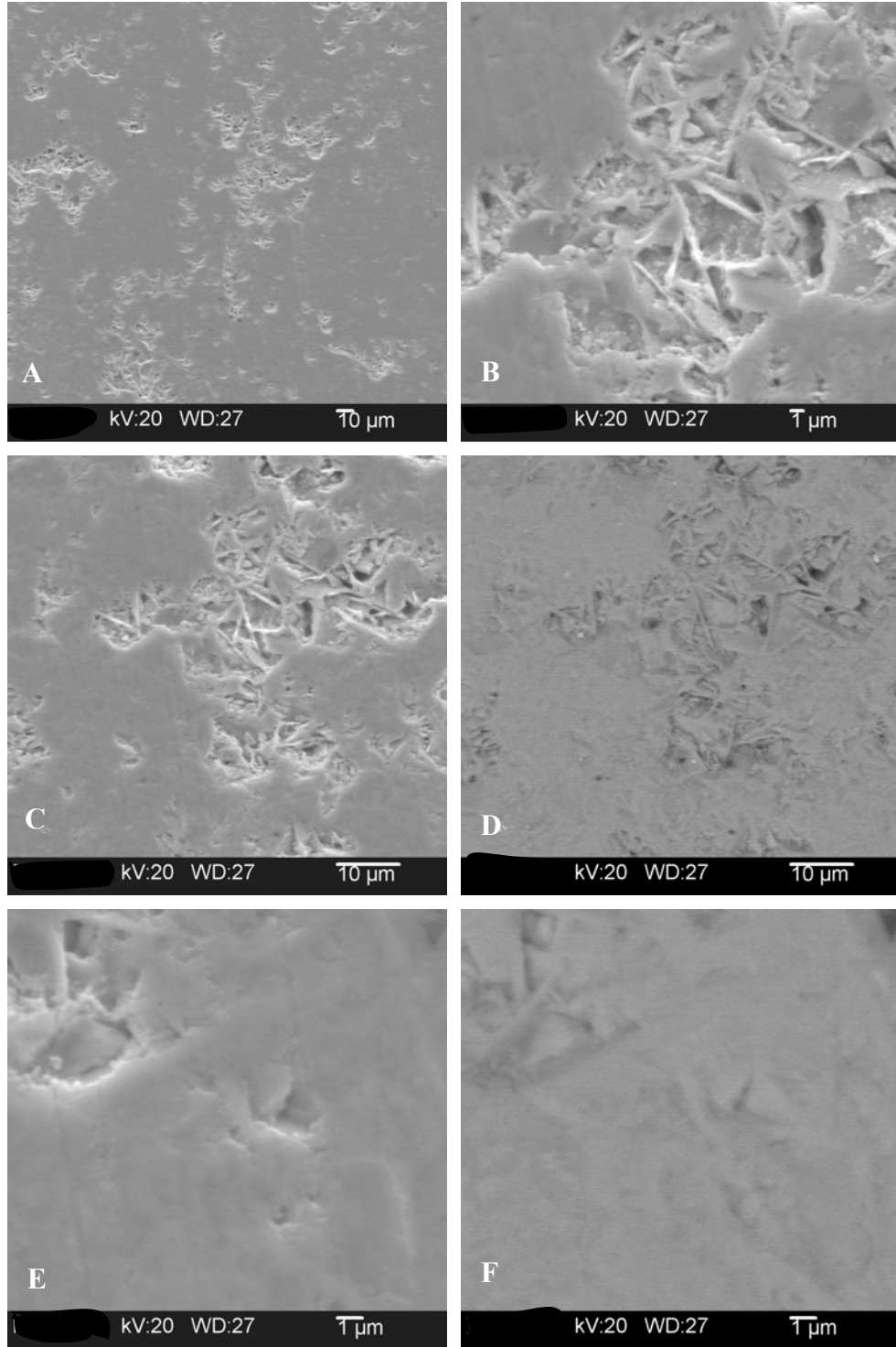


Figure 3.26. SEM images of $\text{Bi}_2\text{Sr}_2\text{Nb}_2\text{Ti}_{0.8}\text{Cr}_{0.2}\text{O}_{12-\delta}$ A,B, C,E are SE images, D and F are BSE images of C and D, respectively.

3.3 Characterization of $\text{Bi}_2\text{Sr}_{(2-x)}\text{Fe}_x\text{Nb}_2\text{Ti}_{0.5}\text{Fe}_{0.5}\text{O}_{12-\delta}$ ($x=0.5,1$)

The samples $\text{Bi}_2\text{Sr}_{1.5}\text{Fe}_{0.5}\text{Nb}_2\text{Ti}_{0.5}\text{Fe}_{0.5}\text{O}_{12-\delta}$ and $\text{Bi}_2\text{Sr}_1\text{Fe}_1\text{Nb}_2\text{Ti}_{0.5}\text{Fe}_{0.5}\text{O}_{12-\delta}$ were prepared by the polymerized complex method, as outlined in Section 2.1.2. Neither sample was phase pure, as evident in Figure 3.27 and Figure 3.28. Both samples contained a strontium-iron-niobate phase and well as a bismuth oxide impurity phase. Unlike other samples, all measurements were made on a Phillips 3100 x-ray diffractometer, with a step size of 0.04° and a count time of 5 seconds.

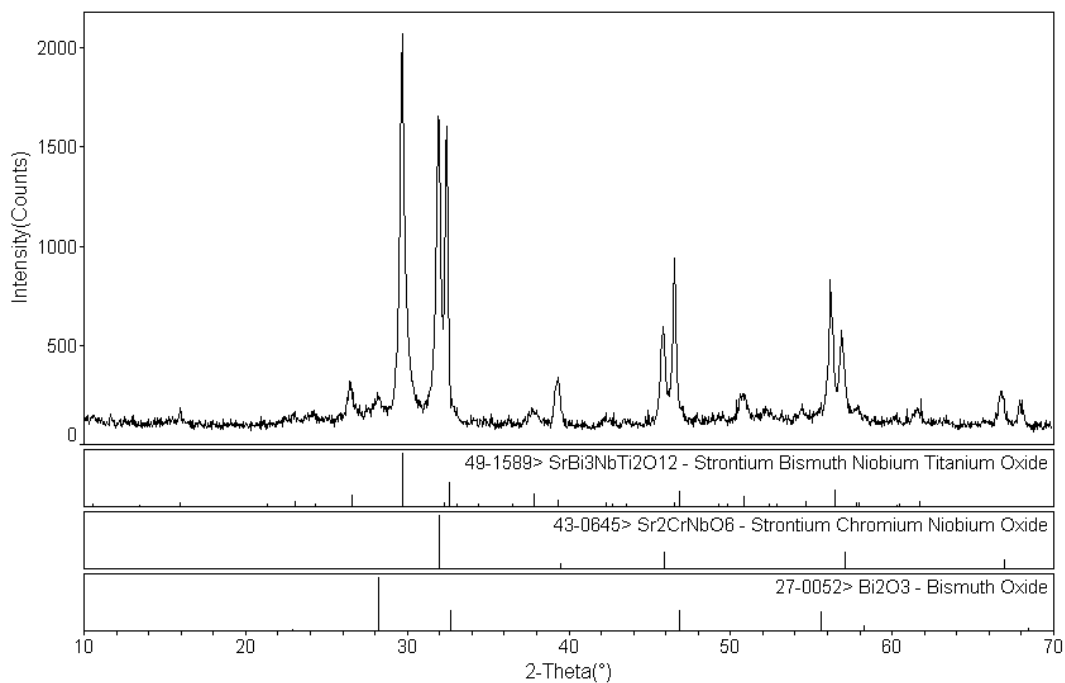


Figure 3.27. XRD pattern of $\text{Bi}_2\text{Sr}_{1.5}\text{Fe}_{0.5}\text{Nb}_2\text{Ti}_{0.5}\text{Fe}_{0.5}\text{O}_{12-\delta}$ post 900/10hrs. The sticks in the bottom of the figure represent the peak placement of the corresponding PDF cards.

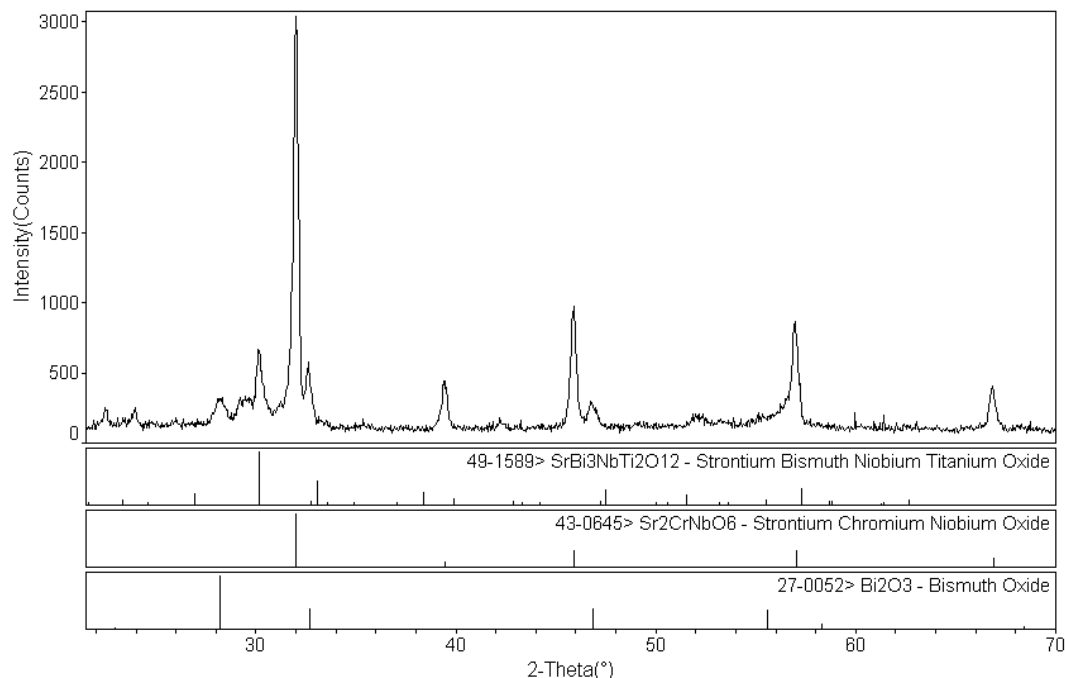


Figure 3.28. XRD pattern of $\text{Bi}_2\text{Sr}_1\text{Fe}_1\text{Nb}_2\text{Ti}_{0.50}\text{Fe}_{0.50}\text{O}_{12-\delta}$ post 900/10hrs. The sticks in the bottom of the figure represent the peak placement of the corresponding PDF cards.

3.4 Characterization of $\text{Bi}_{(2-y)}\text{Pb}_y\text{Nb}_2\text{Ti}_{(1-z)}\text{Al}_z\text{O}_{12-\delta}$ ($y=0-1.2$, $z=0.2, 0.25, 1$)

3.4.1 Synthesis of $\text{Bi}_{(2-y)}\text{Pb}_y\text{Sr}_2\text{Nb}_2\text{Ti}_{(1-z)}\text{Al}_z\text{O}_{12-\delta}$ ($y=0-1.2$)

Compositions of the family $\text{Bi}_{(2-y)}\text{Pb}_y\text{Sr}_2\text{Nb}_2\text{TiO}_{12-\delta}$ ($y=0-1.2$) were synthesized as described in Section 2.1.2. Phase purity was monitored after calcination at 900°C for 10 hours and after sintering pellets at 1050°C for 30 hours with x-ray diffraction. The phase purity results shown in Table X were obtained. Montero obtained the same results in 1998 for the family of compositions $\text{Bi}_{(2-y)}\text{Pb}_y\text{Sr}_2\text{Nb}_2\text{TiO}_{12-\delta}$ ($y=0.25, 0.5, 1, 1.5, 2$), finding phase purity up to $y=0.5$ and questionable purity at $y=1$.²⁶

Table X lists phase purity up to $\text{BiPbSr}_2\text{Nb}_2\text{TiO}_{12-\delta}$; however, above $\text{Bi}_{1.7}\text{Pb}_{0.3}\text{Sr}_2\text{Nb}_2\text{TiO}_{12-\delta}$ phase purity can be disputed, which is discussed in more detail in Sections 3.4.2 and 3.4.3

Table IX: Phase Purity Results Obtained for Lead Substitution Series.

$\text{Bi}_{(2-y)}\text{Pb}_y\text{Sr}_2\text{Nb}_2\text{TiO}_{12-\delta}$		
Composition	Phase Pure 900°C/10hr	Phase Pure 1050°C/30hr
x = 0.1	Yes	Yes
x = 0.2	Yes	Yes
x = 0.3	Yes	Yes
x = 0.4	Yes	Yes
x = 0.5	Yes	Yes
x = 0.6	Yes	Yes
x = 1	Yes	Yes
x = 1.2	No	No

3.4.2 X-ray diffraction of $\text{Bi}_{(2-y)}\text{Pb}_y\text{Sr}_2\text{Nb}_2\text{TiO}_{12-\delta}$ ($y=0-1$)

Figure 3.29 and Figure 3.30 show the diffraction patterns for varying lead concentrations $\text{Bi}_{(2-y)}\text{Pb}_y\text{Sr}_2\text{Nb}_2\text{TiO}_{12-\delta}$ ($y=0.1, 0.2, 0.3, 0.4, 0.5, 0.6, 1$) after sintering at both 900°C and 1050°C. The data collected for the 1050°C series was completed on 1 cm pellet faces (ground lightly on 600 grit SiC paper). The broad low angle hump seen in the patterns in Figure 3.30 is attributed to x-rays striking the sample holder at low angle, when the beam was larger than the pellet face.

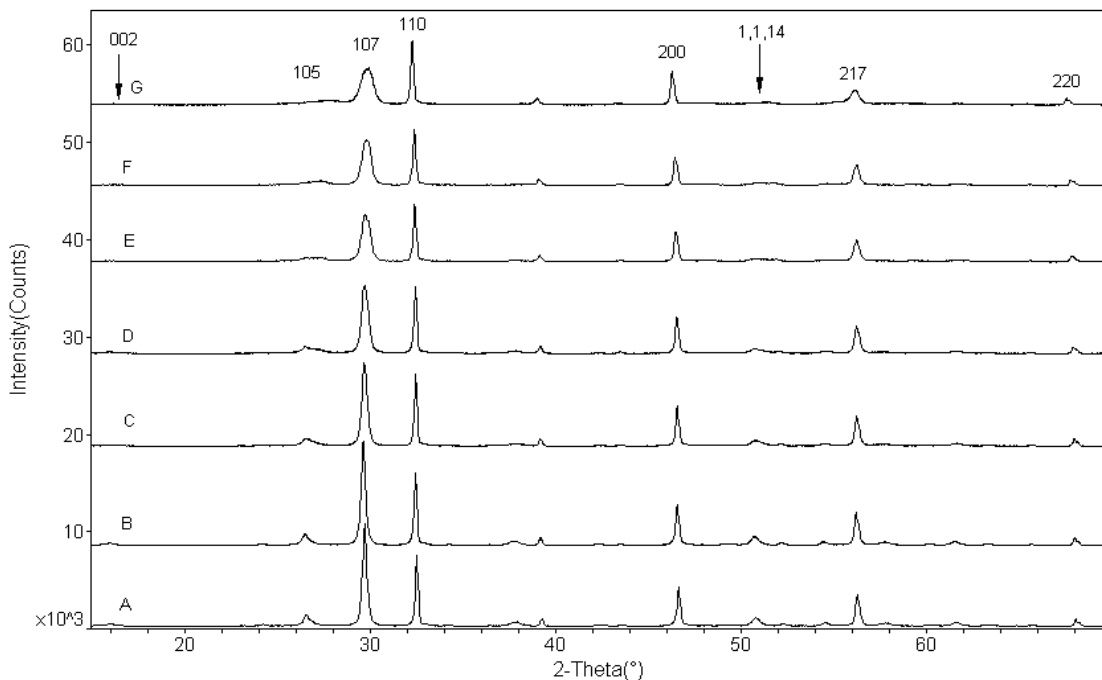


Figure 3.29. XRD patterns of $\text{Bi}_{(2-y)}\text{Pb}_y\text{Sr}_2\text{Nb}_2\text{TiO}_{12-\delta}$ post 900/10hours calcination A) $y=0.1$ B) $y=0.2$, C) $y=0.3$, D) $y=0.4$, E) $y=0.5$, F) $y=0.6$, G) $y=1$.

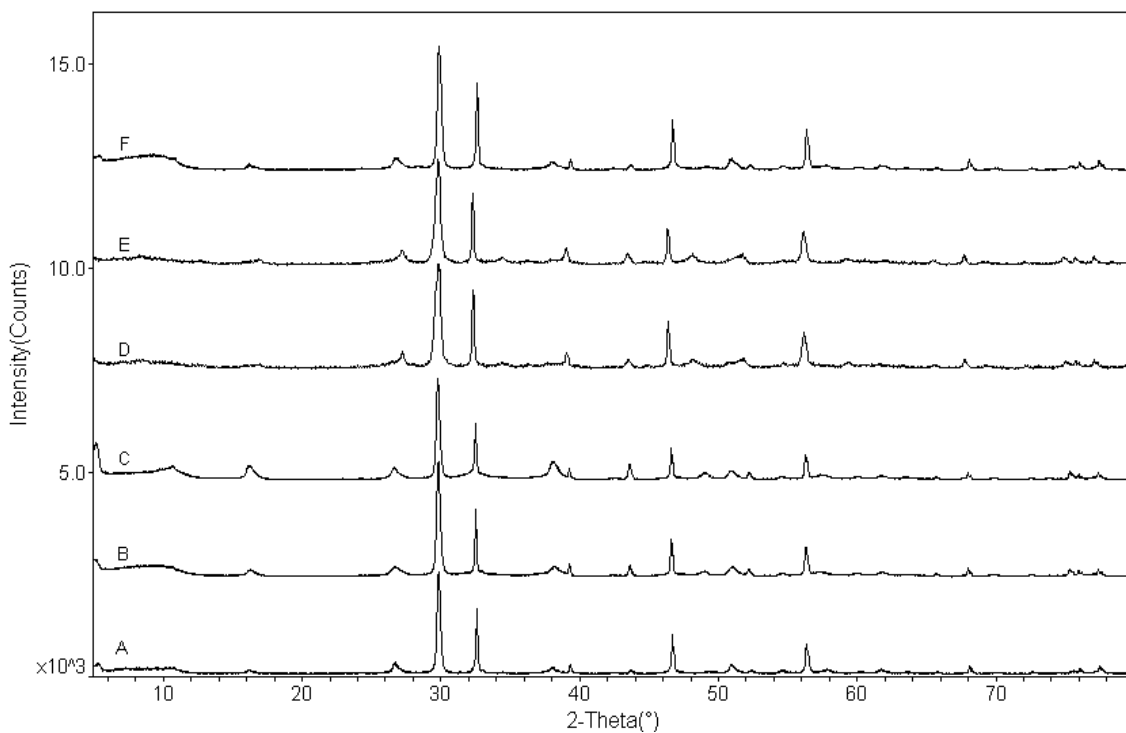


Figure 3.30. XRD patterns of $\text{Bi}_{(2-y)}\text{Pb}_y\text{Sr}_2\text{Nb}_2\text{TiO}_{12-\delta}$ ($y=0-1$) pellet faces post 1050/30hrs sintering A) $y=0.2$ B) $y=0.3$, C) $y=0.4$, D) $y=0.5$, E) $y=0.6$, F) $y=1$. The hump below $15^\circ 2\theta$ is from the sample holder.

3.4.2.1 Anomalous Diffraction Behavior in $\text{Bi}_{(2-y)}\text{Pb}_y\text{Sr}_2\text{Nb}_2\text{TiO}_{12-\delta}$ ($y=0-1$)

Comparison of diffraction data for the lead series (Figure 3.29 and Figure 3.30) with the diffraction data presented for the transition metal series (Section 3.2.2), highlights anomalies. As the amount of lead in $\text{Bi}_{(2-y)}\text{Pb}_y\text{Sr}_2\text{Nb}_2\text{TiO}_{12-\delta}$ is increased, the diffraction pattern of the material changes. It appears that the typical 100% intensity peak ((107) peak at $30^\circ 2\theta$) broadens as a function of composition, while the typical 50% intensity peak ((110) peak at $32.7^\circ 2\theta$) clearly remains sharp.

This trend of broadened peaks is most obvious with the (105) and (107) (Figure 3.29) peaks. However, this broadening continues throughout the pattern as a broadening of all peaks with c-axis character. The characteristic low-angle lines of the Aurivillius material, the (002), (004), and (006) peaks, (at $5, 11$, and $16^\circ 2\theta$ respectively), are not visible with a lead concentration higher than $y=0.2$ (in Figure 3.29), due to this broadening effect. Also the (200) (at $46.5^\circ 2\theta$) and (220) (at $68^\circ 2\theta$) peaks remain sharp independent of composition.

It is also clear from Figure 3.30 that upon sintering some of this effect is relieved, and the diffraction patterns display less of this hkl-specific broadening; however, some of the effect is still seen after sintering.

3.4.2.2 Stacking Faults in Layered Structures

With a layered structure such as the Aurivillius materials, there are often stacking faults present. For example: imagine a layered structure consisting of 3 layers of type B sandwiched between two layers of type C. A stacking fault would be having the incorrect number of B layers between the C layers. With an ideal stacking of CBBBCBBBCBBBC, stacking faults would likely be of CBBBC**BB**CBBBC or CBBBC**BBBB**CBBBC type, with one and 5 B layer stacking faults also possible.^{23,58-60}

This incorrect stacking will affect the d-spacing of the crystals, and therefore the diffraction pattern. Stacking faults are typically observed as anisotropically broadened peaks, as the varying d-spacing causes diffraction at slightly different 2-theta angles than is expected for a particular peak. As Boule noted with an $n=2$ Aurivillius structure, stacking faults typically cause anisotropic broadening of peaks.⁶¹ The broad

peaks in this series were broadened isotropically, while some peaks remained sharp, therefore it was concluded the broadening in this case was not caused by stacking faults.

3.4.2.3 Williamson-Hall plots

With the absence of stacking faults, this leaves the possibility of a crystallite size effect or a crystal strain effect to examine. When one desires to separate crystallite size and strain effects from XRD data, a Williamson-Hall (W.H.) plot is typically used.⁶² Once the full width at half maximum (FWHM or β) is obtained for all the peaks, one can plot $\beta \cdot \cos(\Theta)$ on the y-axis against $4 \cdot \sin(\Theta)$. When this is done the y-intercept represents the crystallite size, and the slope is the strain in the crystallites, as shown in Figure 3.31.

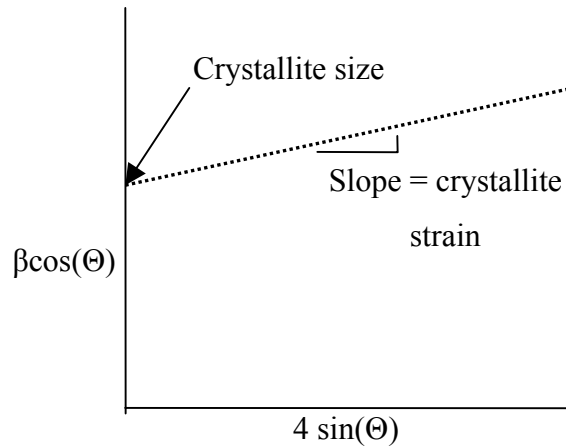


Figure 3.31. Example of a Williamson-Hall plot.

The W.H. method was not successful in separating crystallite size and strain effects. Because of the unique nature of the patterns, with some very broad and some very sharp peaks, the data did not produce a reliable W.H. plot as is clearly seen in Figure 3.32 which is representative of the entire lead series.

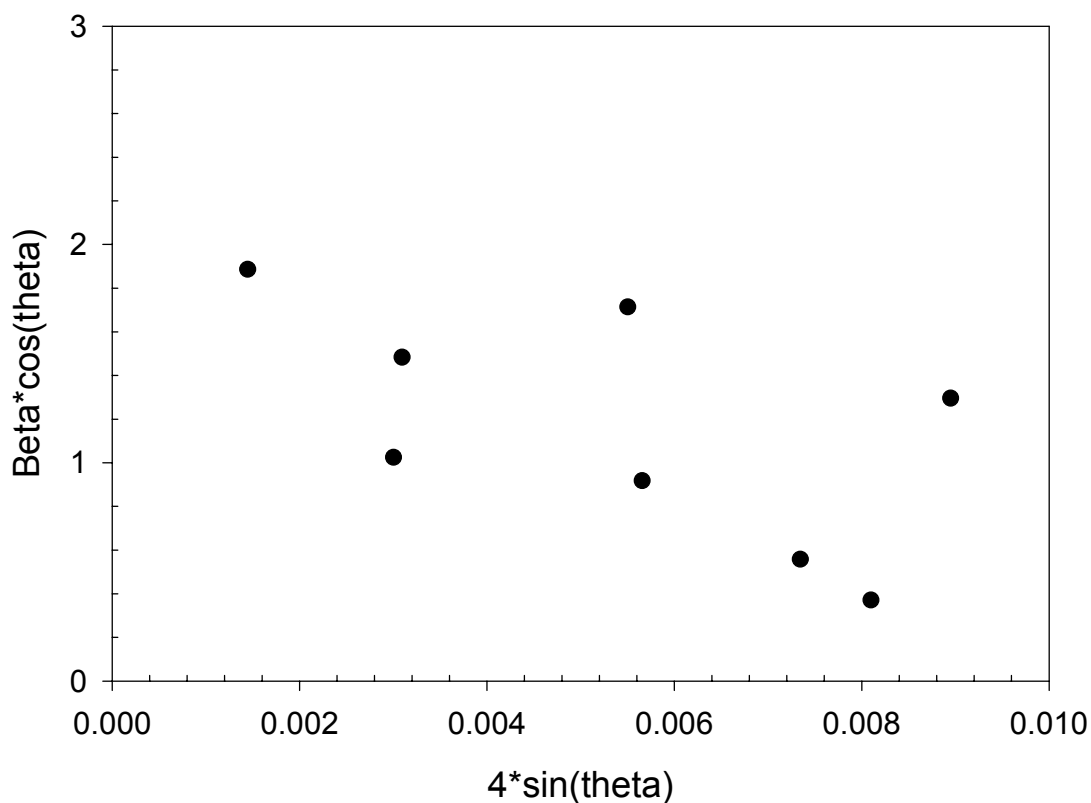


Figure 3.32. Williamson-Hall plot of $\text{Bi}_{1.8}\text{Pb}_{0.2}\text{Sr}_2\text{Nb}_2\text{TiO}_{12-\delta}$ post $900^\circ\text{C}/10\text{hrs}$. The data is representative of Williamson-Hall plots of the entire lead series.

The Williamson-Hall analysis was completed on patterns from the calcined powder ($900^\circ\text{C}/10\text{hrs}$), and sintered pellets ($1050^\circ\text{C}/30\text{hrs}$) on the following hkl's: (006), (105), (107), (110), (1,0,13), (200), (1,1,14), and (217). There were two major problems with the Williamson-Hall plots attempted, which are visible in Figure 3.32. The first problem is the very large amount of scatter in the data used, the second problem was that even if the most erroneous points were removed to try and obtain a linear relationship, the resulting line typically possessed a negative slope, which is not possible in Williamson-Hall analysis, where a slope of zero corresponds to no strain.

3.4.2.4 Separating Size and Strain Effects

Because the standard Williamson-Hall analysis was unsuccessful in separating size and strain effects, a different strategy was adapted. This involved obtaining the FWHM values for the hkl planes ((105), (107), (110), (1,0,13), (200), (1,1,14), and

(217)) using Jade 6.0 and assuming the FWHM was either completely size or stain based, and the corresponding results were plotted as a function of 2-theta. Equations 20 and 21 were used and are listed below. All of the results obtained for the series are familiar, and typical results are show in Figure 3.33 and Figure 3.34.

The crystallite size can be calculated using the Sherrer equation (Equation 20)

$$\tau = \frac{K\lambda}{\beta \cos(\Theta)} \quad (20)$$

Where τ is the crystallite size, K is a shape factor (typically 0.9) β is the FWHM minus the instrumental broadening, while λ is the source radiation.⁶²

The crystallite strain can be calculated using Equation 21.

$$\varepsilon = \frac{\beta}{4 \tan (\Theta)} \quad (21)$$

Where ε is the strain, β is the FWHM minus the instrumental broadening, and theta is the angle of diffraction for the peak.⁶²

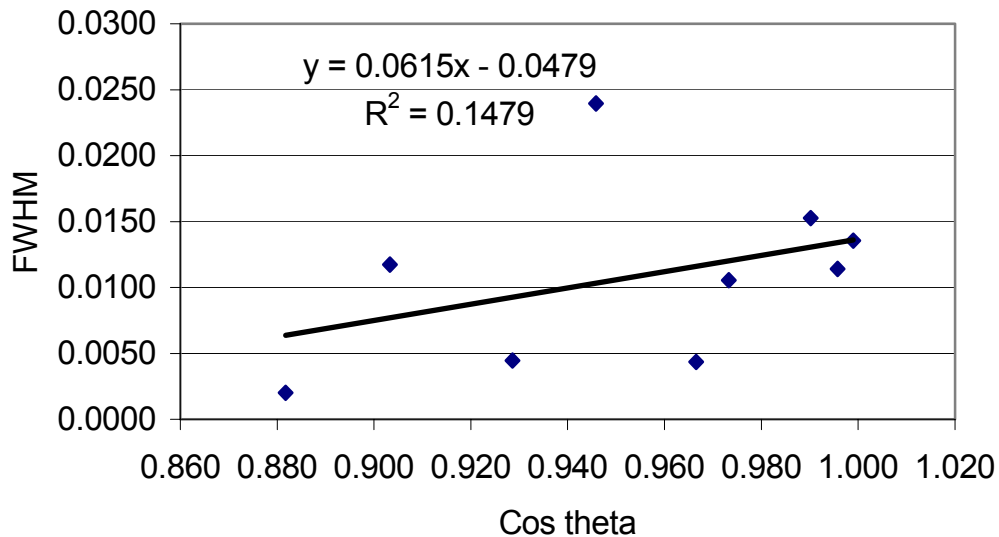


Figure 3.33. Full-width and half maximum plotted against a crystallite size correlation.

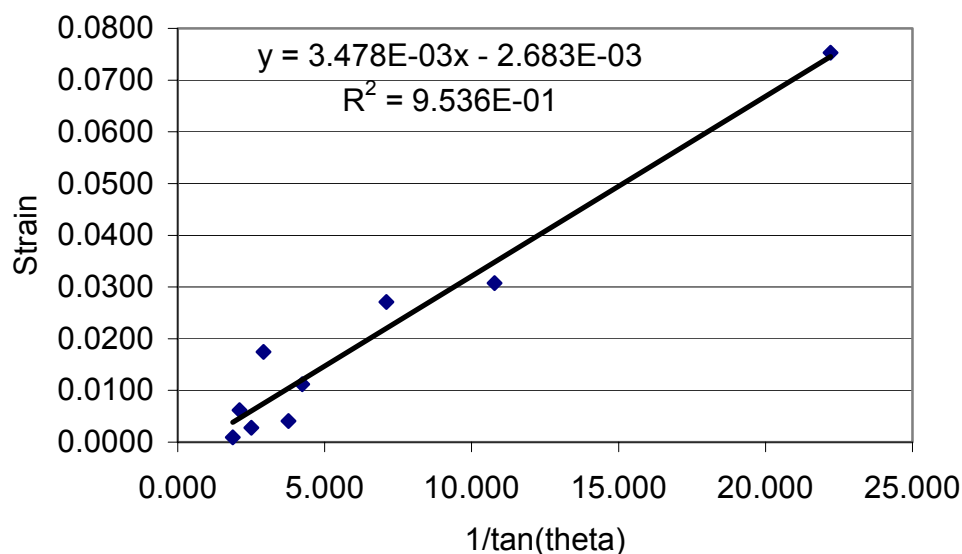


Figure 3.34. Full-width and half maximum plotted against a crystallite strain correlation.

Figures 3.35 and 3.36 present the FWHM values for the lead series as a means of correlating the broadening to a crystallite size or strain effect. The fit of the data to a straight line (the “R” value) was used as means of correlation. It is clear that this approach indicates a stronger crystallite strain effect (Figure 3.34) than a crystallite size effect (Figure 3.33).

The FWHM values were also separated based on peaks that had c-axis character (i.e. (1,1,X) peak where $x \neq 0$), and those that have no c-axis character (i.e. (1,1,0) peak). The crystallite size and the crystallite strain were then calculated and averaged for each concentration of lead substitution. Both were then plotted as a function of the amount of lead in the structure $\text{Bi}_{(2-y)}\text{Pb}_y\text{Sr}_2\text{Nb}_2\text{TiO}_{12-\delta}$ ($y=0-1$) as shown in Figure 3.35 and Figure 3.36. In both cases the crystallite size and strain values are and average of multiple peaks, and are presented as a means of visual comparison. They are not intended for extraction of numerical values of the crystallite size or strain.

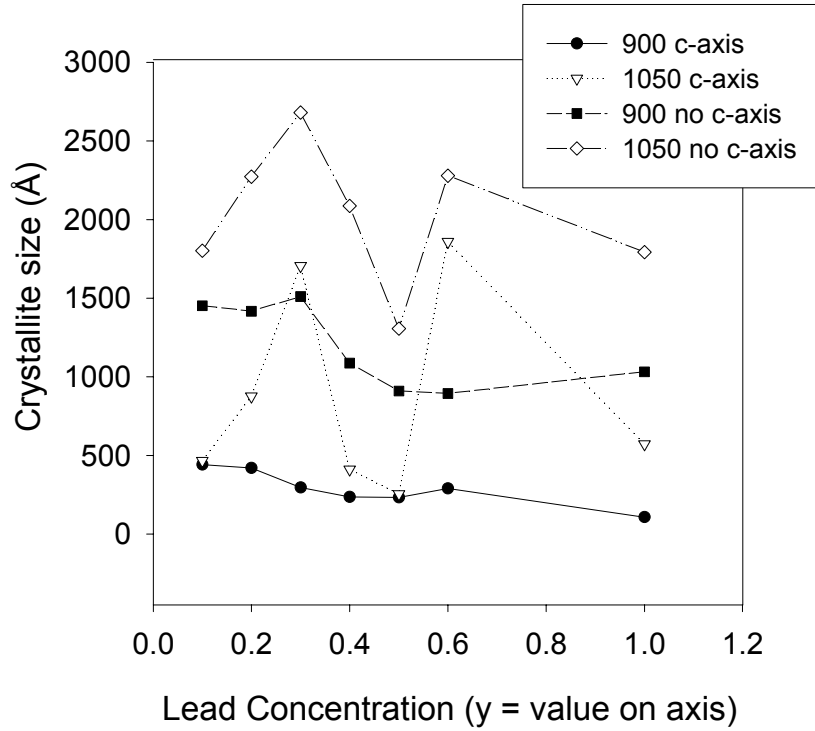


Figure 3.35. Crystallite size of $\text{Bi}_{(2-y)}\text{Pb}_y\text{Sr}_2\text{N}_2\text{TiO}_{12-\delta}$ (y=0-1) calculated from Scherrer equation.

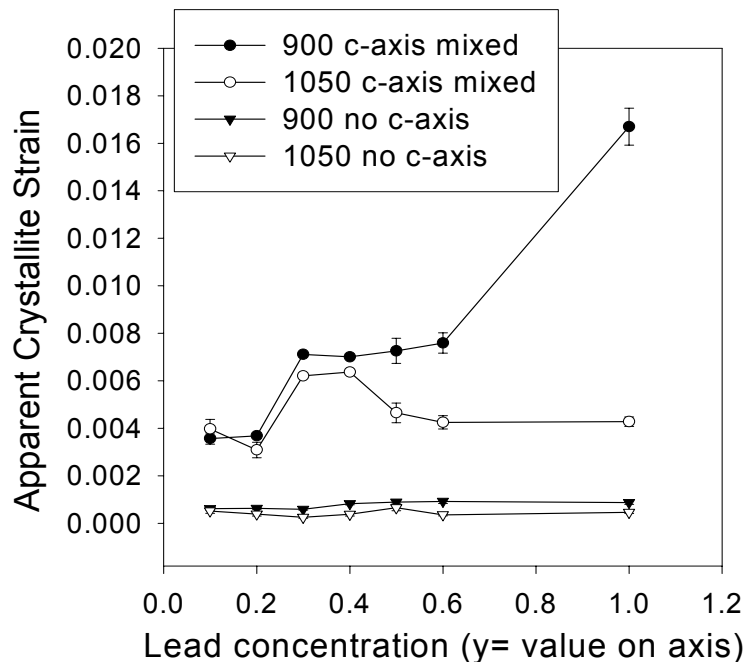


Figure 3.36. Crystallite strain of $\text{Bi}_{(2-y)}\text{Pb}_y\text{Sr}_2\text{Nb}_2\text{TiO}_{12-\delta}$ (y=0-1).

Comparison of Figure 3.35 and Figure 3.36 indicates that crystallite strain correlates more than crystallite size, since the crystallite size data for the sintered pellets show no clear trends (Figure 3.35). This result is in conjunction with those shown in Figure 3.33 and Figure 3.34.

The techniques applied to the FWHM values indicate a possible strain effect to explain the anomalous broadening behavior. However, an experimental observation of the powder having platelet-like characteristics supports an argument for a crystallite size effect. An observation was made that the calcined (900°C/10hrs) powder had a very platelet-like nature. It is possible that the diffraction phenomena could be related to the crystallite size if the crystals preferentially grew along the a-b plane during the calcination step, and the c-axis of the crystals did not develop until the higher temperatures and longer times of sintering.

Another possible explanation for the broadening of the lead series diffraction patterns is small compositional fluctuations at a nanocrystalline scale. The lead ion is slightly larger (1.43Å) than bismuth (1.31Å) in 8-fold coordination. If all the lead is concentrated in one specific (very small) area, and the bismuth in another, this will create fluctuations in unit cell size. The unit cell fluctuations would result in broadened peaks, as there would be diffraction at angles slightly above and below the Bragg angle.

3.4.2.5 Crystallite Size Effect

SEM was completed on the calcined powder in order to confirm the preferential shape of the particles. The powder was sprinkled onto a conductive tape for analysis. Several of the images obtained are presented in the Figure 3.37 and Figure 3.38 below.

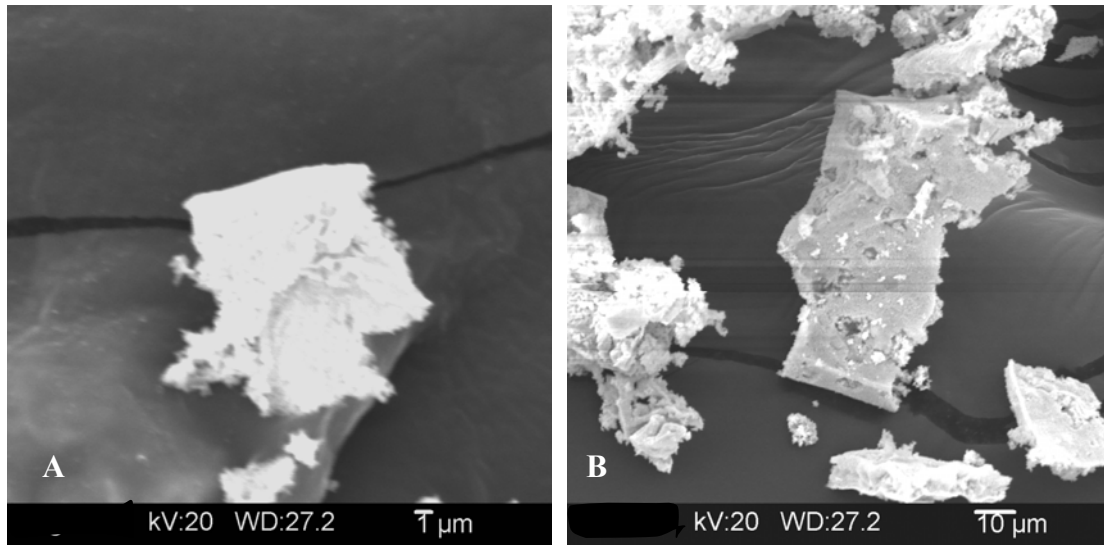


Figure 3.37. Secondary electron SEM images of calcined powder. A and B show platelet nature of particles, A shows square-like nature, an indication of growth along the a-b plane.

The SEM images show not only that the particles tend to have smooth surfaces; in many cases there was a square cross-section. This is believed to be a correlation to the a-b plane in the tetragonal Aurivillius materials synthesized. The SEM image for the sample after calcination show this square cross section, and the SEM images of the sintered pellets show many elongated crystals, a possible parallel to the long c-axis of the Aurivillius material, which has had longer time to grow after sintering at 1050°C/30 hours. This could just as easily be the square platelet particles (like Figure 3.37) on edge. Figure 3.39 illustrates this elongation in the sintered disks for several samples within the lead series and one iron substituted sample from Section 3.2.4.2.

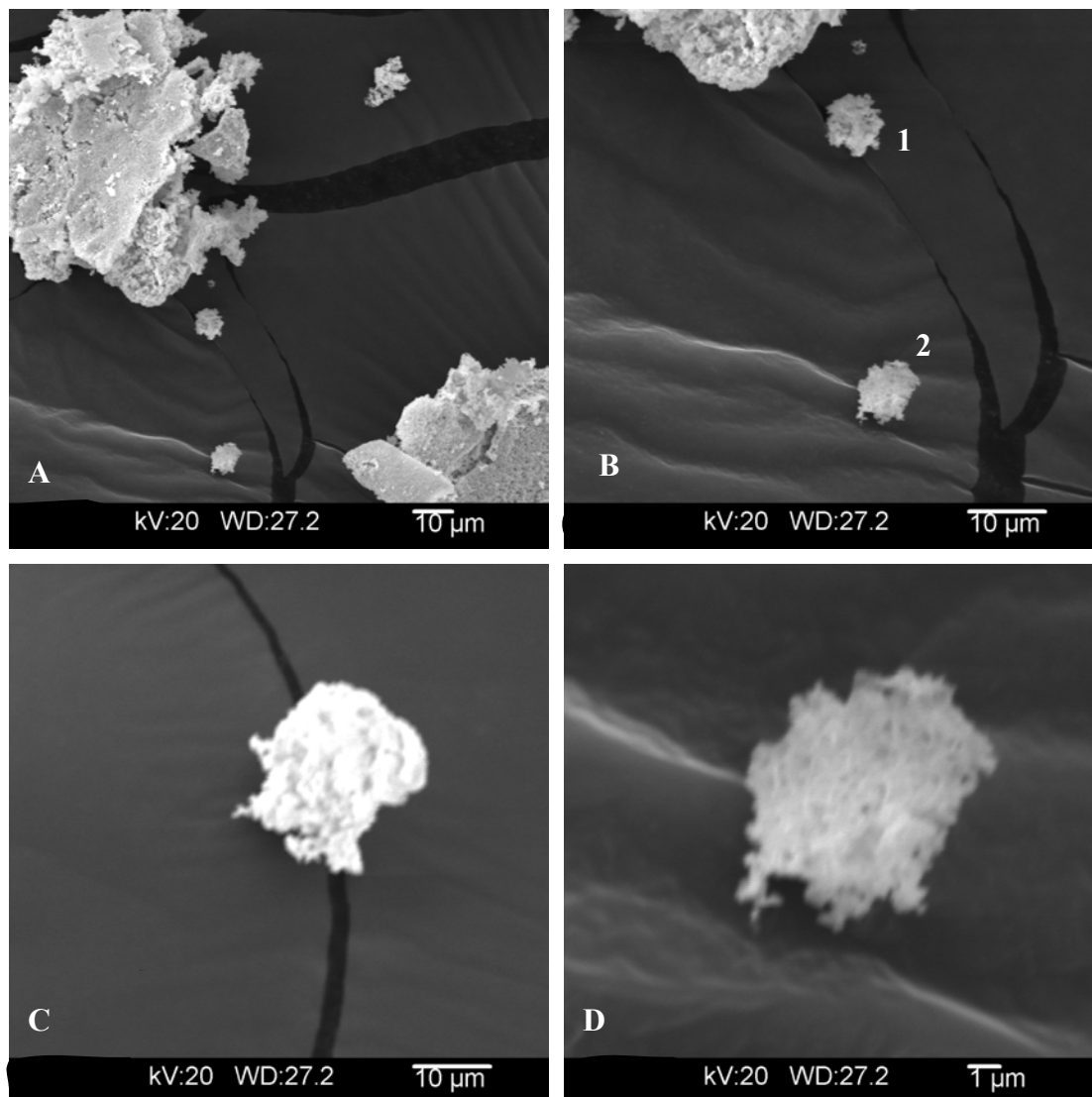


Figure 3.38. Secondary electron SEM images of calcined powder A) particle platelet of damaged square B) Close up of A C) close up of the particle labeled 1 in B, notice the square nature D) close up of the particle labeled 2 in B.

Attempts to model the XRD patterns for all compositions within the lead series $\text{Bi}_{(2-y)}\text{Pb}_y\text{Sr}_2\text{N}_2\text{TiO}_{12-\delta}$ ($y=0.1,0.2,0.3,0.4,0.5,0.6,1$) (after calcination and sintering) via Rietveld analysis proved unsuccessful. Once again this was attributed to the anomalous nature of the peak broadening. The possibility of an impurity phase is described in detail in Section 3.4.3.

The existing evidence presented does suggest that some of the anomalous diffraction phenomenon is caused by a crystallite size effect, while some crystallite

strain is likely still present in the structure, as evident by the broadening still present in the patterns after sintering.

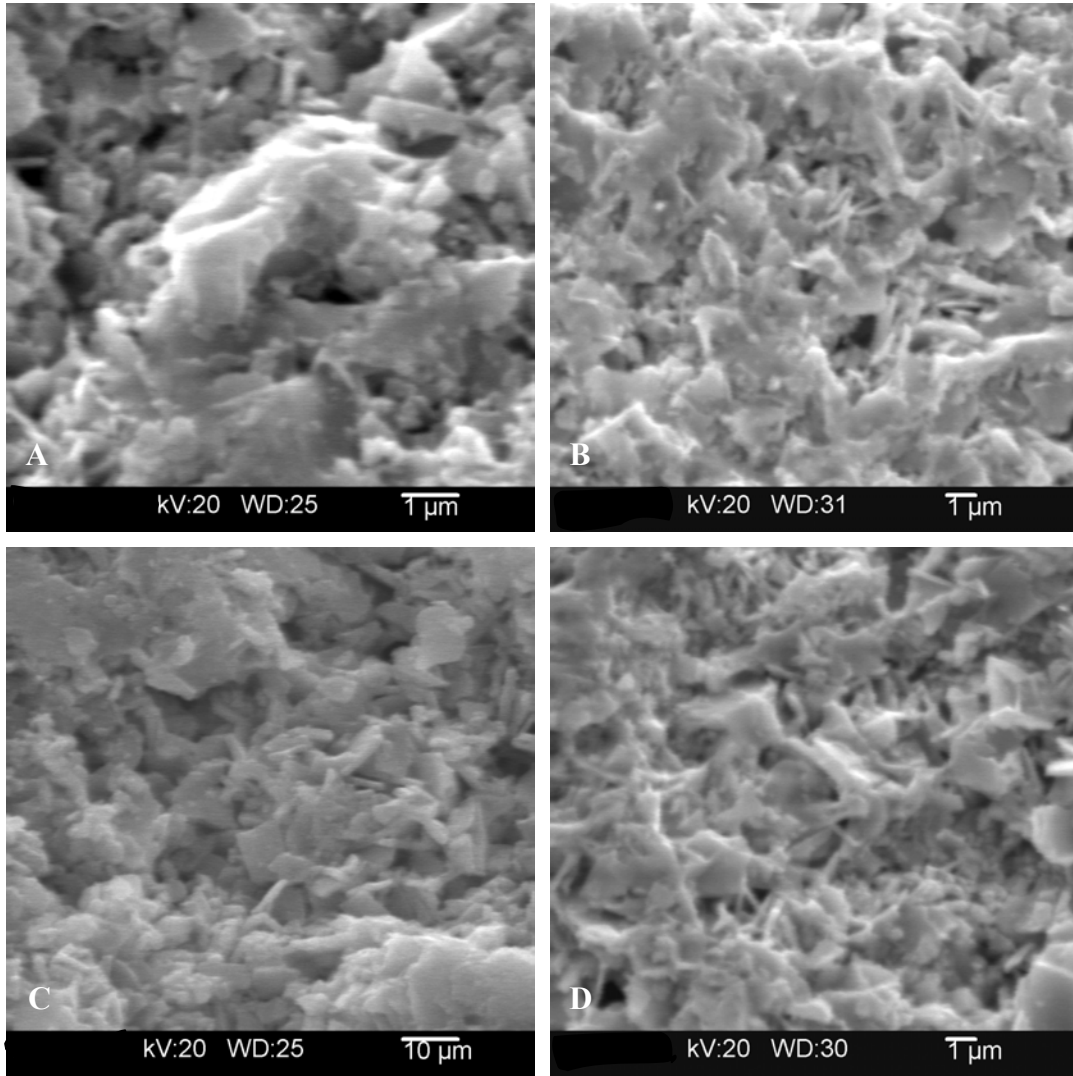


Figure 3.39. All images are secondary electron images of sintered pellets micrograph A is $\text{Bi}_{1.6}\text{Pb}_{0.4}\text{Sr}_2\text{Nb}_2\text{TiO}_{12-\delta}$, B is $\text{Bi}_{1.7}\text{Pb}_{0.3}\text{Sr}_2\text{Nb}_2\text{TiO}_{12-\delta}$, C is $\text{BiPbSr}_2\text{Nb}_2\text{TiO}_{12-\delta}$, and D is $\text{Bi}_{1.4}\text{Pb}_{0.6}\text{Sr}_2\text{Nb}_2\text{TiO}_{12-\delta}$.

3.4.3 Possible Impurity Phase in $\text{Bi}_{(2-y)}\text{Pb}_y\text{Sr}_2\text{Nb}_2\text{TiO}_{12-\delta}$ ($y=0.4-1$)

As was mentioned previously, the compositions in the series $\text{Bi}_{(2-y)}\text{Pb}_y\text{Sr}_2\text{Nb}_2\text{TiO}_{12-\delta}$ above $y=0.3$ may not be phase pure. Although the SEM images presented in Section 3.4.4 do not show impurity phases; the diffraction phenomena

could indicate an impurity. As is evident in Figure 3.29, the (105) peak (at about $27.5^\circ 2\theta$) seems to both broaden, and shift to the right significantly. This indicates the possibility of the impurity phase (most likely a bismuth-oxide or lead-oxide impurity is apparent, as shown in Figure 3.40).

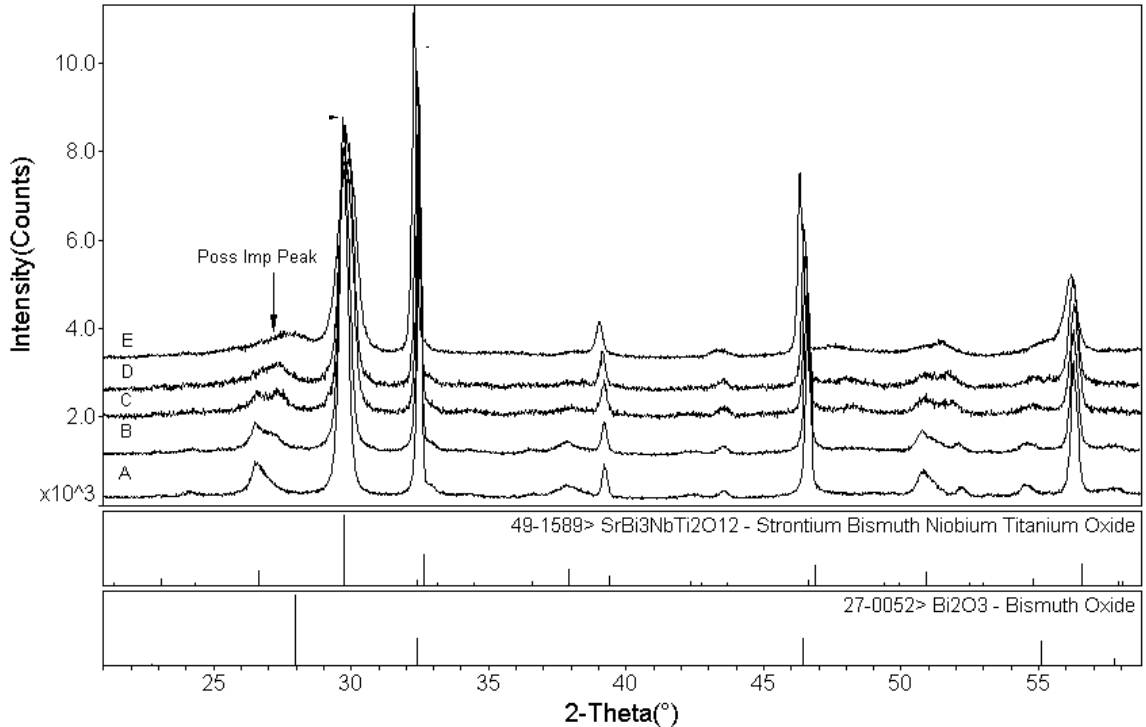


Figure 3.40. XRD patterns for $\text{Bi}_{(2-y)}\text{Pb}_y\text{Sr}_2\text{Nb}_2\text{TiO}_{12-\delta}$ showing possible impurity phase appearing at lead concentrations of $y=0.4$ and higher, indicated by arrow at about $28^\circ 2\theta$. A) $\text{Bi}_{1.7}\text{Pb}_{0.3}\text{Sr}_2\text{Nb}_2\text{TiO}_{12-\delta}$ B) $\text{Bi}_{1.6}\text{Pb}_{0.4}\text{Sr}_2\text{Nb}_2\text{TiO}_{12-\delta}$ C) $\text{Bi}_{1.5}\text{Pb}_{0.5}\text{Sr}_2\text{Nb}_2\text{TiO}_{12-\delta}$ D) $\text{Bi}_{1.4}\text{Pb}_{0.6}\text{Sr}_2\text{Nb}_2\text{TiO}_{12-\delta}$ E) $\text{BiPbSr}_2\text{Nb}_2\text{TiO}_{12-\delta}$. All patterns are for calcined powder ($900^\circ\text{C}/10\text{hrs}$). The sticks in the bottom of the figure represent the peak placement of the corresponding PDF cards.

It is evident that at lead substitution higher than $y=0.3$ in the family of compositions $\text{Bi}_{(2-y)}\text{Pb}_y\text{Sr}_2\text{Nb}_2\text{TiO}_{12-\delta}$ a peak is present at about $28^\circ 2\theta$. This was not alarming at first because the structure dictates that there are two peaks at $27.5^\circ 2\theta$, and two are often present (see the transition metal series in Figure 3.12, for example). However, it is concerning that as the lead concentration increases the peak position shifts to higher 2θ . The concerning fact is that this peak is at the correct angle to be the 100% intensity peak of a bismuth or lead-oxide impurity phase, as PDF card 27-0052 in

Figure 3.40 shows. Some of the peaks shift and broadening could be explained by the anomalous diffraction behavior explained earlier, but it is less likely to create such a large shift of the peak. This gives evidence that the lead series compositions are possibly not phase pure at levels higher than $y=0.2$ in $\text{Bi}_{(2-y)}\text{Pb}_y\text{Sr}_2\text{Nb}_2\text{TiO}_{12-\delta}$, a 10% lead for bismuth substitution.

There are also equally as convincing arguments against the possibly impurity phase. The first argument against an impurity phase is an experimental observation; most impure Aurivillius materials (with the typical bismuth-oxide impurity) have at least a slight yellow color to them from the bismuth. The parent phase $\text{Bi}_2\text{Sr}_2\text{Nb}_2\text{TiO}_{12}$ in its pure form is white, as are all those compositions within the lead series. If in fact there was an impurity phase present in the higher lead concentration samples one would expect to observe at least a slight color change, which was not the case.

The impedance and conductivity data presented in Section 3.4.5 also argue against the impurity possibility. Bismuth oxide is a good ionic conductor, $10^1 \text{S}\cdot\text{cm}^{-1}$ at 800°C^{34} , and even in small amounts it could influence the conductivity of the sample. Yet in the series $\text{Bi}_{(2-y)}\text{Pb}_y\text{Sr}_2\text{Nb}_2\text{TiO}_{12-\delta}$ as

Figure 3.45 shows, as lead is added the conductivity noticeably decreases.

It is noted that this impurity phase speculation is also hindered by Figure 3.30; which shows that after sintering A) there does not appear to be an impurity peak, and B) a majority of the anomalous diffraction behavior observed after calcination (Figure 3.29) has been relieved. Even with all the evidence to the contrary, the possibility of the impurity phase cannot be ignored. More evidence against a possible impurity phase was obtained via TEM analysis, which is presented in the appendix.

3.4.4 Microstructure of $\text{Bi}_{(2-y)}\text{Pb}_y\text{Sr}_2\text{Nb}_2\text{TiO}_{12-\delta}$ ($y=0-1$)

The microstructure of the series $\text{Bi}_{(2-y)}\text{Pb}_y\text{Sr}_2\text{Nb}_2\text{TiO}_{12-\delta}$ ($y=0.1, 0.2, 0.3, 0.4, 0.5, 0.6, 1$) was examined using SEM as described in Section 2.1.6. The density of all pellets in the lead series were on the order of 50% theoretical density, noticeably lower than those obtained for the transition metal series. The SEM was completed as a means of confirming phase purity. All of the SEM images were similar, and only images for the $y=0.3, y=0.4$ and $y=1$ compositions will be presented.

Figure 3.42 and Figure 3.43 illustrate the large amount of porosity with the SE images, and the lack of observable secondary phases in the BSE images, which contradicts the possibility of an impurity phase.

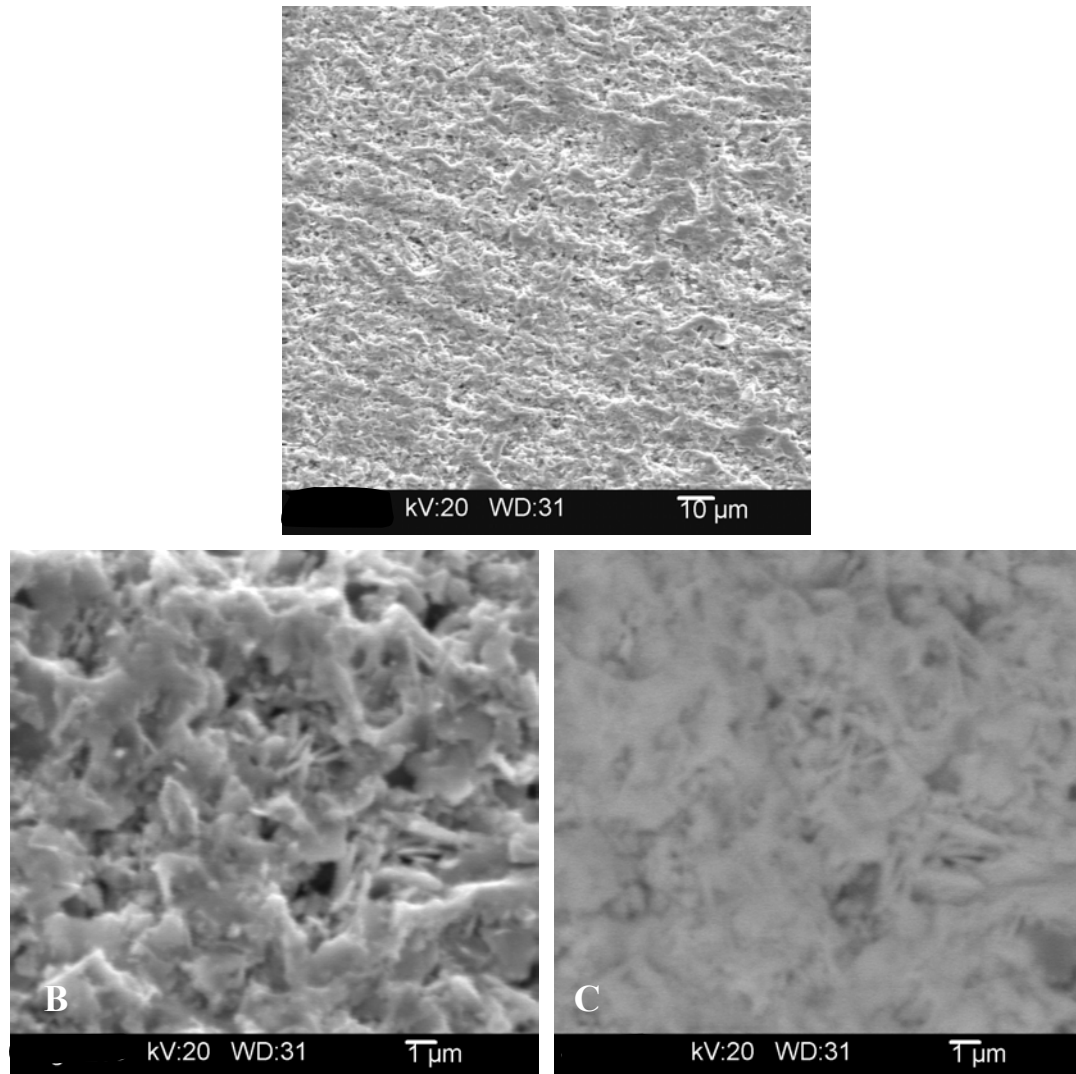


Figure 3.41. SEM images of $\text{Bi}_{1.7}\text{Pb}_{0.3}\text{Sr}_2\text{Nb}_2\text{TiO}_{12-\delta}$ after sintering at $1050^\circ\text{C}/30\text{hrs}$. A and B are SE images, C is a BSE image of the same area as B.

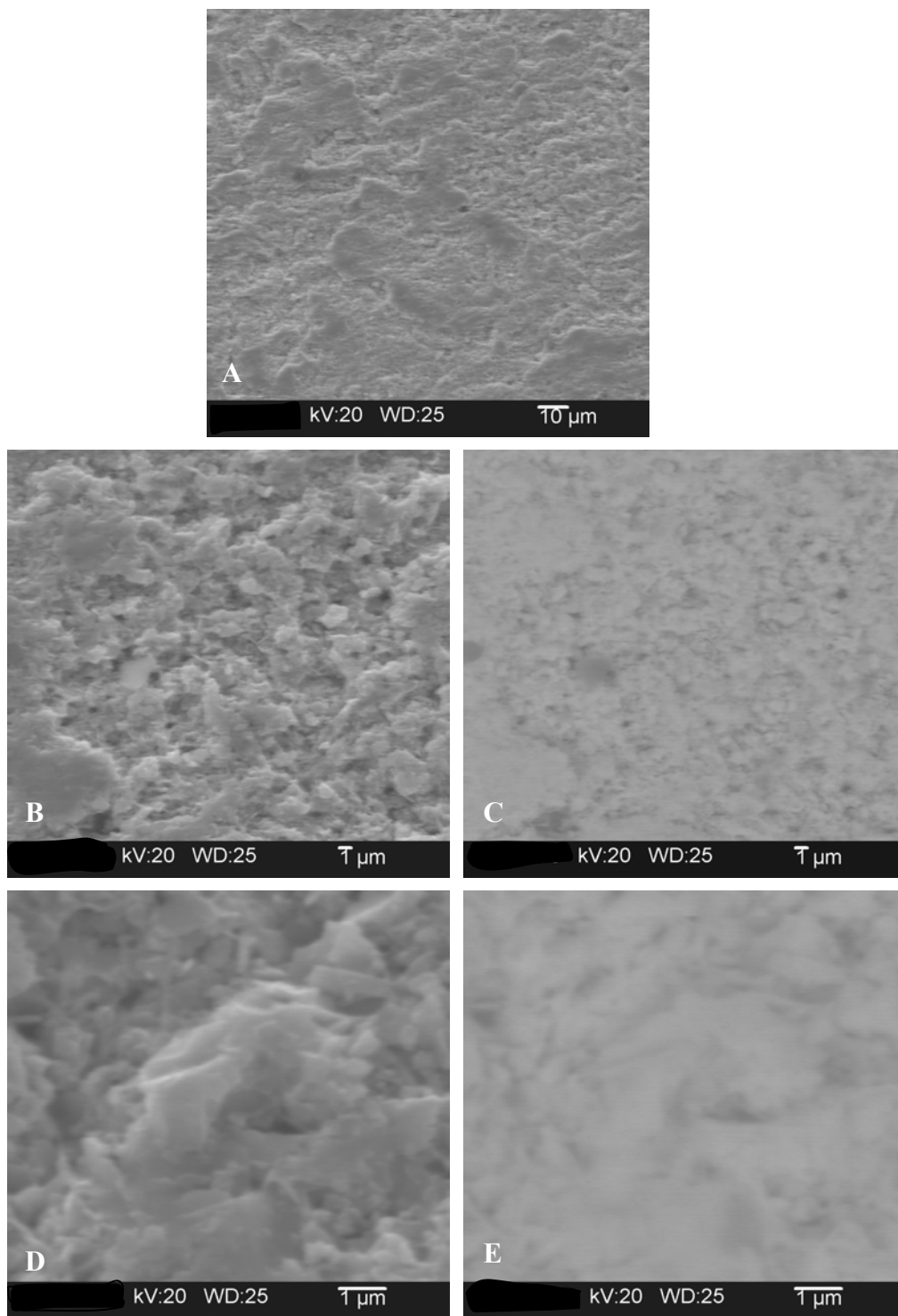


Figure 3.42. SEM images of $\text{Bi}_{1.6}\text{Pb}_{0.4}\text{Sr}_2\text{Nb}_2\text{TiO}_{12-\delta}$ C, E are BSE images of B,D.

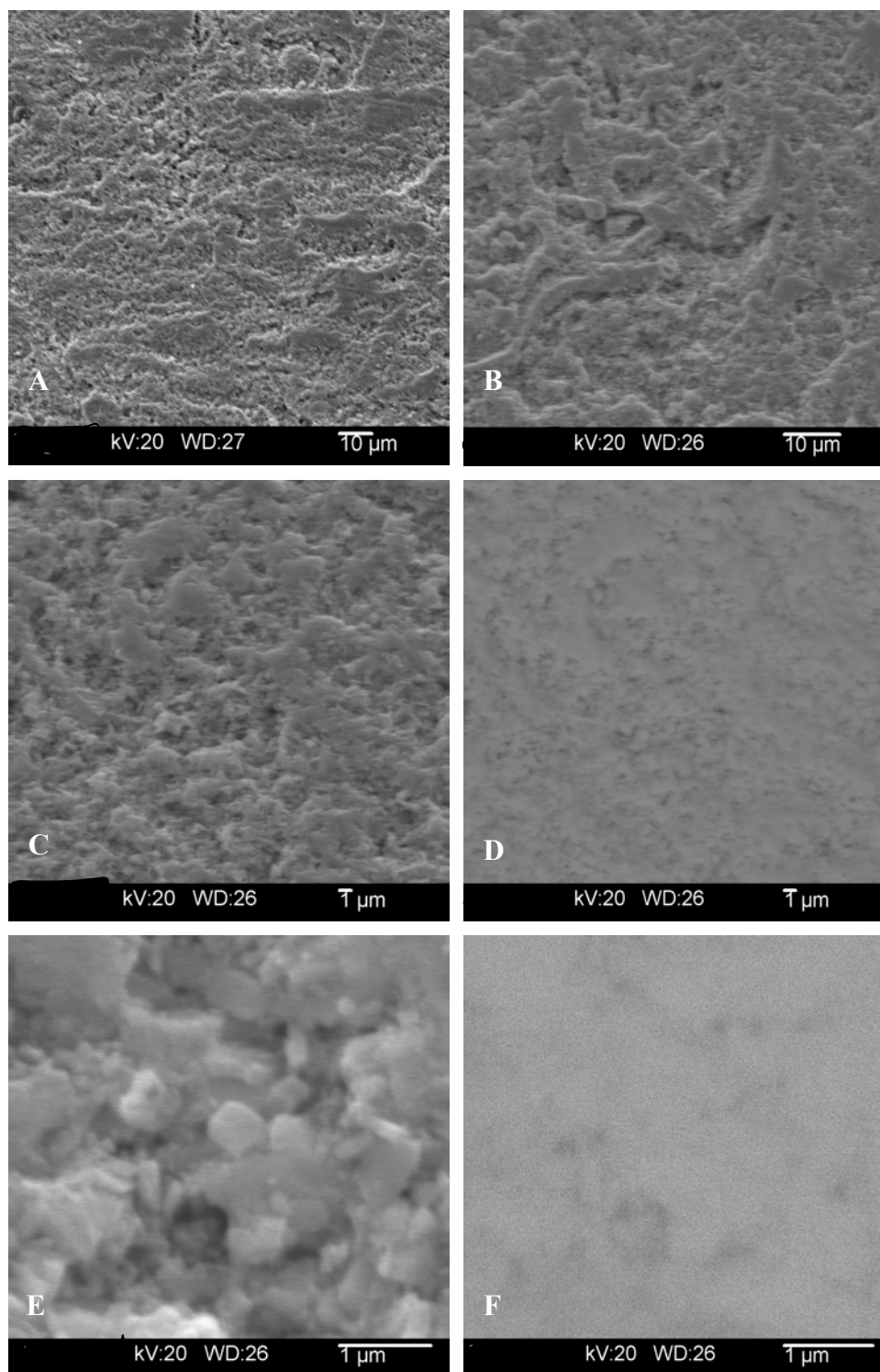


Figure 3.43. SEM images of $\text{BiPbSr}_2\text{Nb}_2\text{TiO}_{12-\delta}$. A, B, C, and E are SE images, D and F are the BSE images of C and E, respectively.

3.4.5 AC Conductivity of $\text{Bi}_{(2-y)}\text{Pb}_y\text{Sr}_2\text{Nb}_2\text{TiO}_{12-\delta}$ ($y=0-1$)

Table X and Figure 3.45 show the conductivity data for the lead substituted series $\text{Bi}_{(2-y)}\text{Pb}_y\text{Sr}_2\text{Nb}_2\text{TiO}_{12-\delta}$ ($y=0-1$). All conductivity was normalized to the density of the sample with the highest density ($y=0.2$) within the lead series. Large additions of lead decreased the sample conductivity. The error in the data was less than 6% in all samples.

Table X: Conductivity Data for $\text{Bi}_{(2-y)}\text{Pb}_y\text{Sr}_2\text{Nb}_2\text{TiO}_{12-\delta}$ ($y=0-1$).

$\text{Bi}_{(2-y)}\text{Pb}_y\text{Sr}_2\text{Nb}_2\text{TiO}_{12-\delta}$					
x	Conductivity @ 950°C (S/cm)	E_{a2} (400-1000°C) (eV)	E_{a1} <400°C (eV)	Theoretical Density (g/cm ³)	% Theoretical Density
0	-3.10	0.9	0.2	6.731	52.6
0.2	-3.22	1	0.7	6.729	58.3
0.3	-3.26	1	0.6	6.728	47.3
0.4	-3.39	1	0.6	6.726	50.8
0.5	-3.31	1	0.6	6.725	47.8
0.6	-3.40	1	0.5	6.724	53
1	-4.00	1	n/a	6.719	52.7

It is evident from Table X that large additions of lead to the parent phase tend to decrease the conductivity. At lead substitution levels higher than $y=0.2$ the conductivity decreased (except for the $y=0.5$ sample). This phenomenon was also observed by Pineda-Flores in the similar composition $\text{Bi}_4\text{Ti}_3\text{O}_{12}$, where gadolinium and dysprosium were substituted for bismuth.¹⁵

All Cole-Cole plots appeared the same, with a large arc encompassing grain and grain boundary response, and a smaller electrode arc at low frequency. However in the $\text{BiPbSr}_2\text{Nb}_2\text{TiO}_{12-\delta}$ composition the grain and grain boundary response are visible, with the grain response at higher frequency (low Z'). Several typical Cole-Cole plots can be seen below in Figure 3.44. The Conductivity data is presented graphically in Figure 3.45.

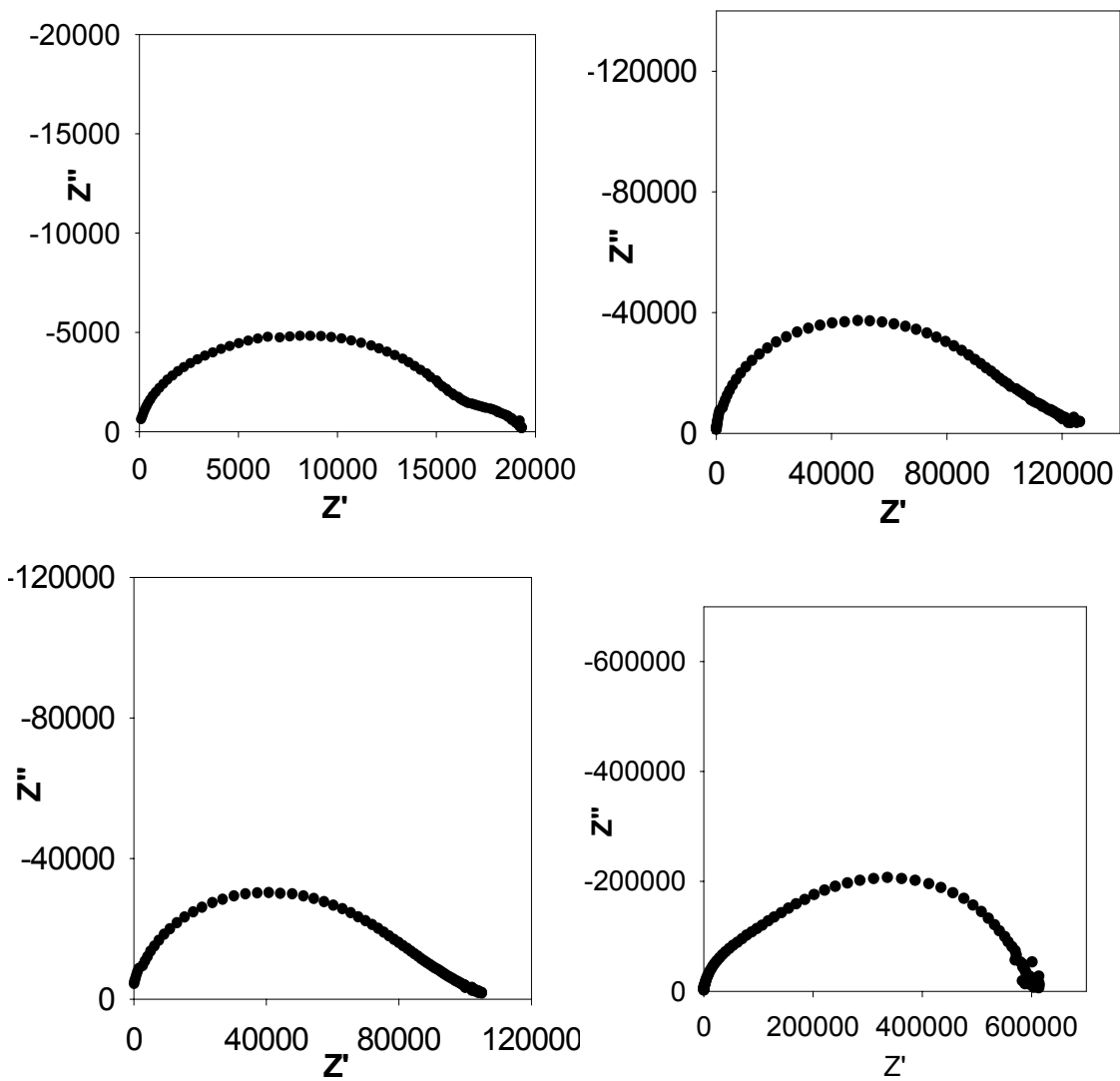


Figure 3.44. Cole-Cole plots for several compositions within lead series $\text{Bi}_{(2-y)}\text{Pb}_y\text{Sr}_2\text{Nb}_2\text{TiO}_{12-\delta}$ at 600°C .

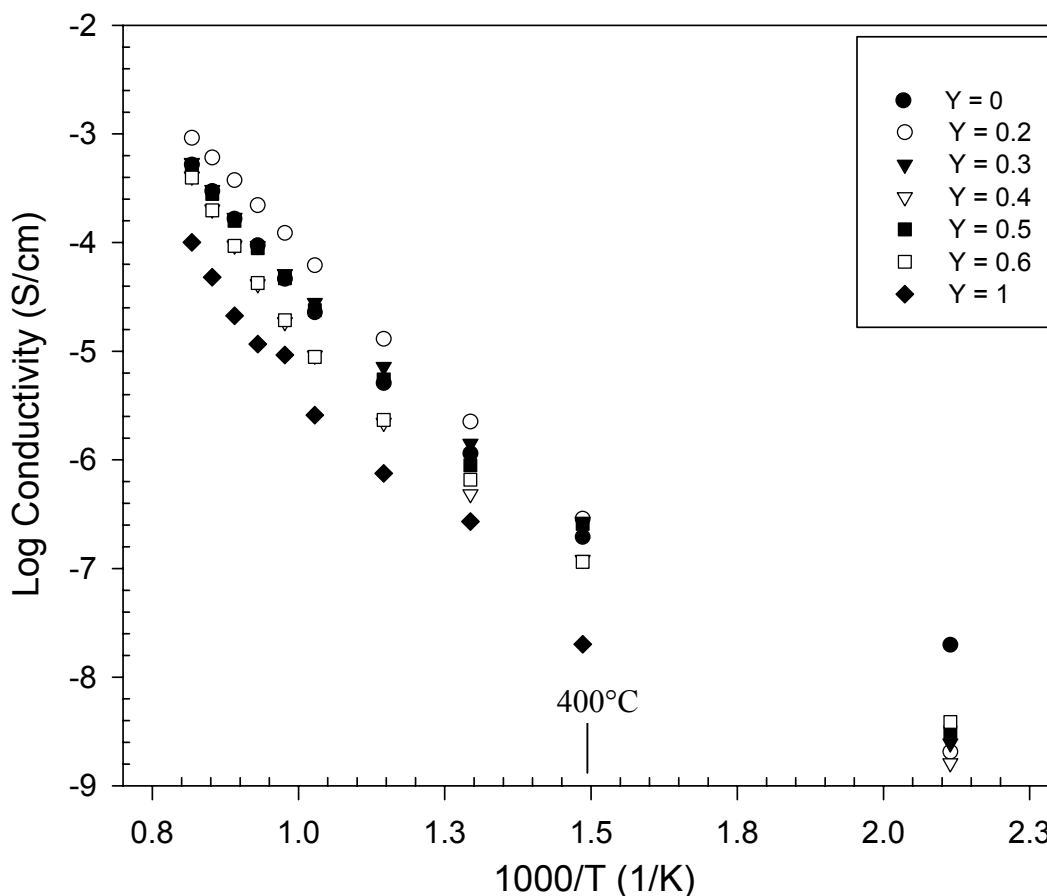


Figure 3.45. Conductivity of $\text{Bi}_{(2-y)}\text{Pb}_y\text{Sr}_2\text{Nb}_2\text{TiO}_{12-\delta}$ ($y=0-1$) from AC impedance.

It is assumed that when lead is substituted for bismuth, oxygen vacancies are created to compensate for the lower valence cation. However, addition of vacancies should increase the conductivity, which did not occur.

If the majority of conduction occurs in the bismuth layer, a conductivity drop can be explained by vacancy association. Low additions of lead create oxygen vacancies, which do not effect the conductivity significantly because they are not very mobile in the structure.³⁷ As additional lead is substituted for bismuth, there are a large number of oxygen vacancies being created in the bismuth layer. If these vacancies are close to one another they can associate. The defect pair is less mobile than a lone oxygen vacancy to move through the structure, thus the conductivity is lowered.

When the highest lead concentration is reached ($\text{BiPbSr}_2\text{Nb}_2\text{TiO}_{12-\delta}$), it is possible we have a large number of associated oxygen vacancies throughout the

bismuth layer. These would further impede the motion of the non-associated vacancies, resulting in a noticeable drop in conductivity, as seen in Figure 3.45.

The other factor to consider when discussing this drop in conductivity is site mixing. Aurivillius materials are known to display site mixing, which essentially means that some of the bismuth ions swap with the strontium ions in $\text{Bi}_2\text{Sr}_2\text{Nb}_2\text{TiO}_{12}$ as a means of alleviating some of the strain associated with the structure.^{37,63-65} This effect is also known to increase as the amount of a larger substitution (than that on the host site) is incorporated into the structure.³⁷ Henceforth, there is likely a situation where some lead and bismuth are sitting in the perovskite layer, and strontium in the bismuth layer as we add more lead. Although the exact affects of this situation are not clear, this could certainly play a factor in the observed drop in conductivity as well.

3.4.6 X-ray Diffraction of $\text{Bi}_{0.8}\text{Pb}_{1.2}\text{Sr}_2\text{Nb}_2\text{TiO}_{12-\delta}$

As shown in Table and Figure 3.46, at a lead concentration of $y=1.2$ ($\text{Bi}_{0.8}\text{Pb}_{1.2}\text{Sr}_2\text{Nb}_2\text{TiO}_{12-\delta}$), phase stability is not achieved. Similar to the compositions in Section 3.4.3, the XRD data presented in Figure 3.46 indicates a bismuth impurity phase is present.

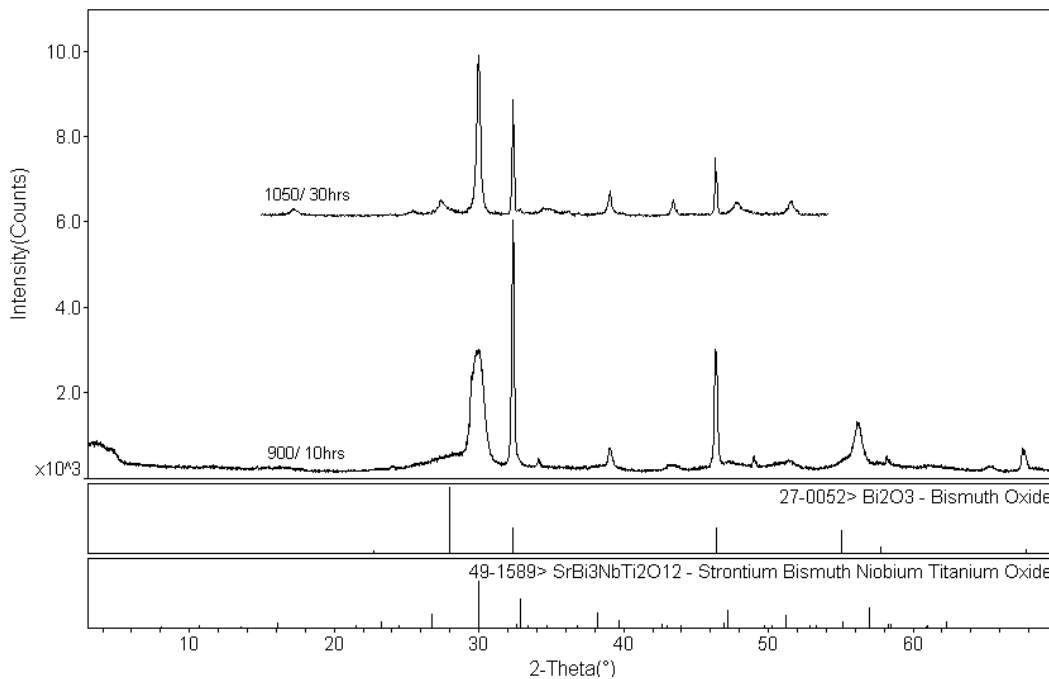


Figure 3.46. XRD patterns for $\text{Bi}_{0.8}\text{Pb}_{1.2}\text{Sr}_2\text{Nb}_2\text{TiO}_{12-\delta}$ after calcination and sintering. The sticks in the bottom of the figure represent the peak placement of the corresponding PDF cards.

3.4.7 Synthesis of $\text{Bi}_{(2-y)}\text{Pb}_y\text{Sr}_2\text{Nb}_2\text{Ti}_{(1-z)}\text{Al}_z\text{O}_{12-\delta}$ ($y=0.4, z=0.02, 0.25, 1$)

Compositions of the family $\text{Bi}_{(2-y)}\text{Pb}_y\text{Sr}_2\text{Nb}_2\text{Ti}_{(1-z)}\text{Al}_z\text{O}_{12-\delta}$ ($y=0.4, Z=0.2, 0.25, 1$) (Table XI) were synthesized as described in Section 2.1.2. The lead and aluminum substituted sample ($\text{Bi}_{1.6}\text{Pb}_{0.4}\text{Sr}_2\text{Nb}_2\text{Ti}_{0.8}\text{Al}_{0.2}\text{O}_{11.7}$) was synthesized to confirm results obtained by Luisi.⁴⁶ Some of the original (incorrect)³¹ work completed on Aurivillius phases by Kendall⁸⁻¹¹ utilized aluminum substitutions. The goal was to make a rough attempt at determining the amount of aluminum that could be successfully incorporated into the structure. Phase purity was monitored with x-ray diffraction after calcination at 900°C for 10 hours and after sintering pellets at 1050°C for 30 hours (Table XI). Only the sample with both lead and aluminum in the structure, $\text{Bi}_{1.6}\text{Pb}_{0.4}\text{Sr}_2\text{Nb}_2\text{Ti}_{0.8}\text{Al}_{0.2}\text{O}_{12-\delta}$ (Figure 3.47) was able to achieve phase purity. The $\text{Bi}_2\text{Sr}_2\text{Nb}_2\text{Ti}_{0.75}\text{Al}_{0.25}\text{O}_{12-\delta}$ composition had a large bismuth impurity phase (Figure 3.48), and $\text{Bi}_2\text{Sr}_2\text{Nb}_2\text{AlO}_{12-\delta}$ had a small bismuth oxide impurity phase as shown in Figure 3.49.

Table XI: Phase Purity Results for Lead and Aluminum Substitution.

Composition	Phase pure 900°C/10hr	Phase Pure 1050°C/30hr
$\text{Bi}_2\text{Sr}_2\text{Nb}_2\text{Ti}_{0.75}\text{Al}_{0.25}\text{O}_{11.5}$	No	No
$\text{Bi}_{1.6}\text{Pb}_{0.4}\text{Sr}_2\text{Nb}_2\text{Ti}_{0.8}\text{Al}_{0.2}\text{O}_{11.7}$	No	Yes
$\text{Bi}_2\text{Sr}_2\text{Nb}_2\text{AlO}_{11.5}$	No	No

3.4.7.1 X-ray Diffraction of $\text{Bi}_{(2-y)}\text{Pb}_y\text{Sr}_2\text{Nb}_2\text{Ti}_{(1-z)}\text{Al}_z\text{O}_{12-\delta}$ ($y=0.4$, $z=0.025, 0.4, 1$)

Diffraction patterns were collected on a Phillips 3100 x-ray diffractometer, with a step size of 0.04° and a count time of 8 seconds. The only sample that was phase pure was $\text{Bi}_{1.6}\text{Pb}_{0.4}\text{Sr}_2\text{Nb}_2\text{Ti}_{0.8}\text{Al}_{0.2}\text{O}_{12-\delta}$. There was a bismuth oxide phase present after calcination that was not present upon sintering, shown in Figure 3.47.

As is evident in Figure 3.49, after calcination $\text{Bi}_2\text{Sr}_2\text{Nb}_2\text{Ti}_{0.75}\text{Al}_{0.25}\text{O}_{12-\delta}$ had a very large bismuth oxide impurity phase. $\text{Bi}_2\text{Sr}_2\text{Nb}_2\text{AlO}_{12-\delta}$ also contained a bismuth oxide impurity phase, shown in Figure 3.48.

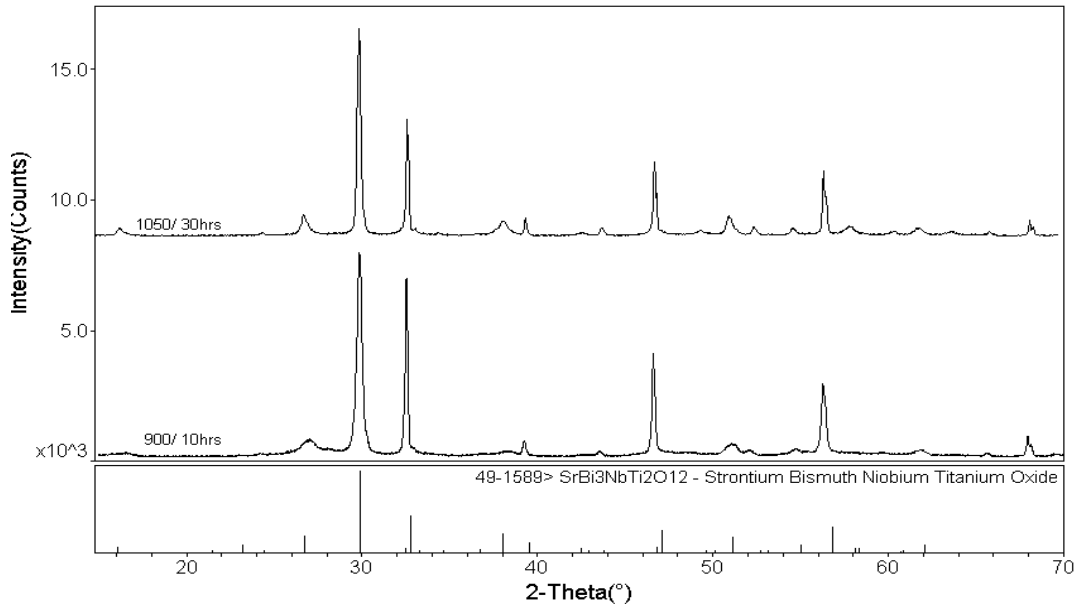


Figure 3.47. XRD patterns for $\text{Bi}_{1.6}\text{Pb}_{0.4}\text{Sr}_2\text{Nb}_2\text{Ti}_{0.8}\text{Al}_{0.2}\text{O}_{12-\delta}$ after calcination and sintering. The sticks in the bottom of the figure represent the peak placement of the corresponding PDF cards.

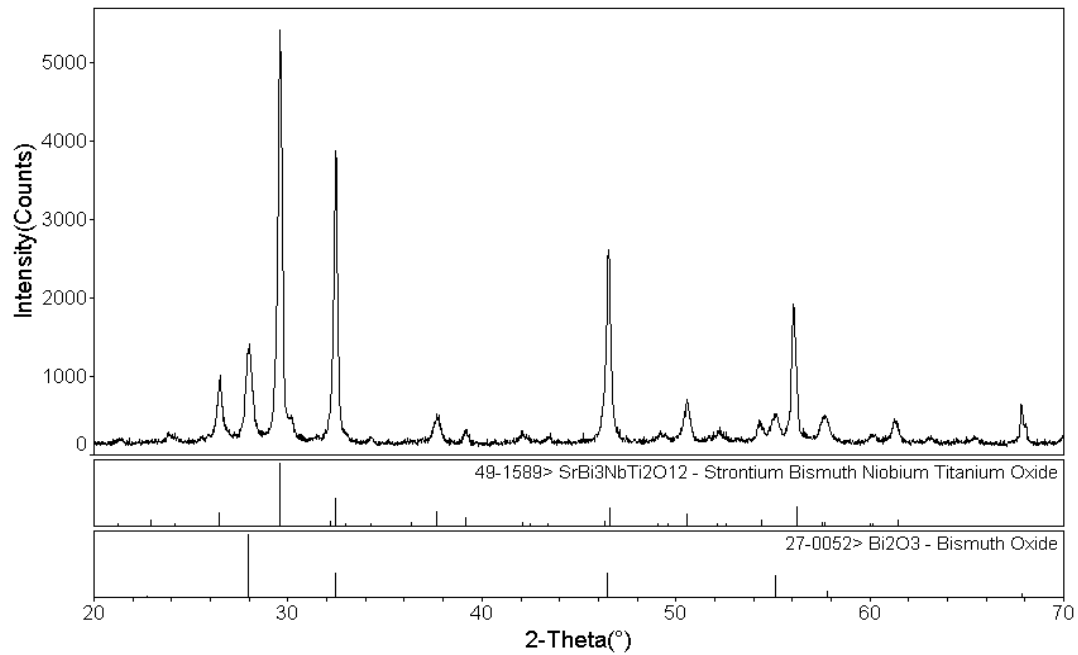


Figure 3.48. XRD pattern for $\text{Bi}_2\text{Sr}_2\text{Nb}_2\text{Ti}_{0.75}\text{Al}_{0.25}\text{O}_{12-\delta}$ after calcination at $900^\circ\text{C}/10\text{hrs}$. The sticks in the bottom of the figure represent the peak placement of the corresponding PDF cards.

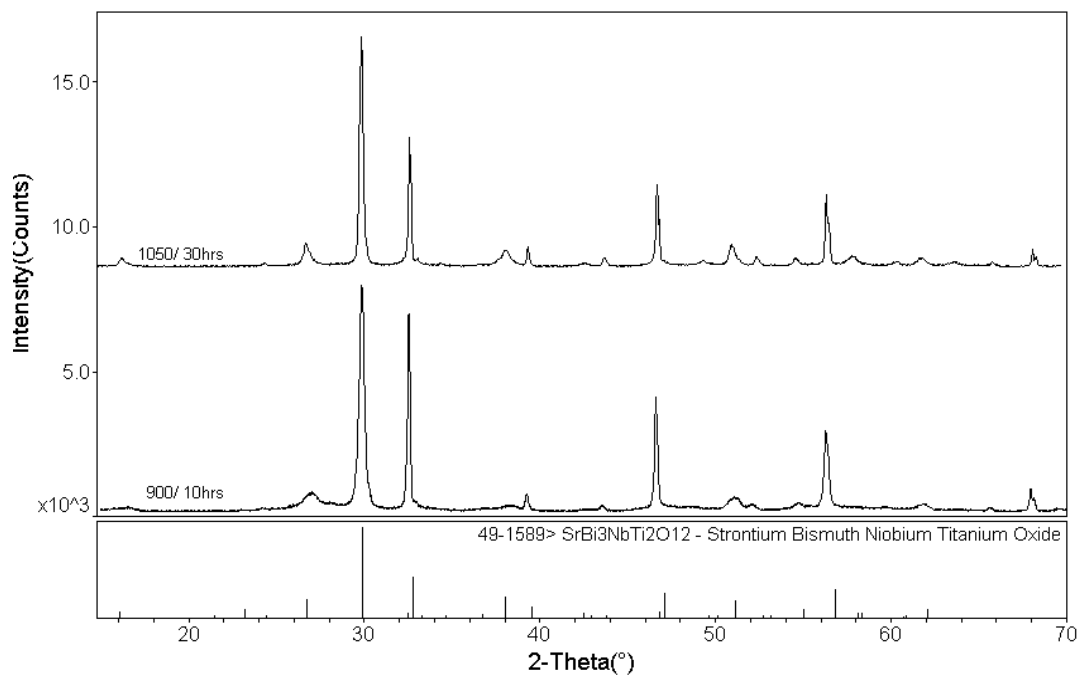


Figure 3.49. XRD patterns for $\text{Bi}_2\text{Sr}_2\text{Nb}_2\text{AlO}_{12-\delta}$ after calcination and sintering. The sticks in the bottom of the figure represent the peak placement of the corresponding PDF cards.

3.4.7.2 AC Conductivity of $\text{Bi}_{1.6}\text{Pb}_{0.4}\text{Sr}_2\text{Nb}_2\text{Ti}_{0.8}\text{Al}_{0.2}\text{O}_{12-\delta}$

The AC conductivity of $\text{Bi}_{1.6}\text{Pb}_{0.4}\text{Sr}_2\text{Nb}_2\text{Ti}_{0.8}\text{Al}_{0.2}\text{O}_{12-\delta}$ was measured as described in Section 2.1.7.1. Table XII, Figure 3.50 shows the conductivity data, compared to the parent phase ($\text{Bi}_2\text{Sr}_2\text{Nb}_2\text{TiO}_{12}$) and a solely lead substituted sample ($\text{Bi}_{1.6}\text{Pb}_{0.4}\text{Sr}_2\text{Nb}_2\text{TiO}_{12-\delta}$).

Table XII: Conductivity Data for $\text{Bi}_{1.6}\text{Pb}_{0.4}\text{Sr}_2\text{Nb}_2\text{Ti}_{0.8}\text{Al}_{0.2}\text{O}_{12-\delta}$ and Similar Samples.

$\text{Bi}_{(2-y)}\text{Pb}_y\text{Sr}_2\text{Nb}_2\text{Ti}_{(1-z)}\text{Al}_z\text{O}_{12-\delta}$					
y, z	Conductivity @ 950°C (S/cm)	E_{a_2} (400- 1000°C) eV	E_{a_1} <400°C	Theoretical Density (g/cm ³)	% Theoretical Density
0	-3.10	0.9	0.2	6.731	52.6
0.4	-3.39	1	0.6	6.726	50.8
0.4, 0.2	-3.36	1	0.6	6.699	61.9

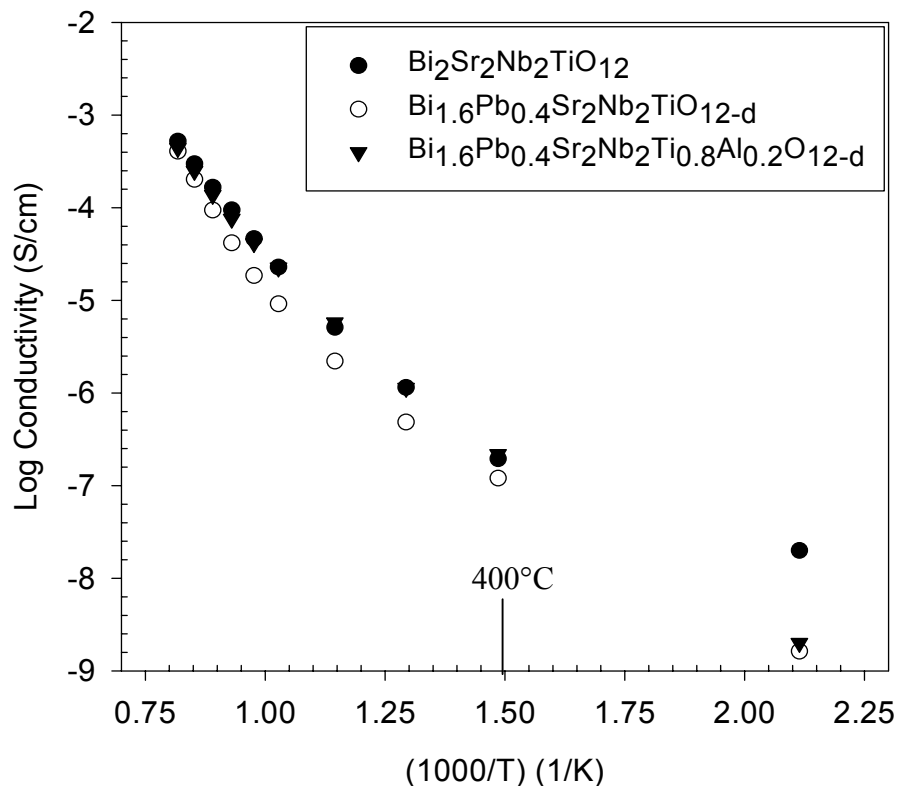
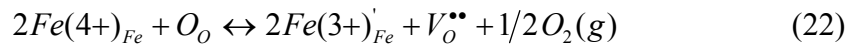


Figure 3.50. AC conductivity for $\text{Bi}_{1.6}\text{Pb}_{0.4}\text{Sr}_2\text{Nb}_2\text{Ti}_{0.8}\text{Al}_{0.2}\text{O}_{12-d}$ and related unsubstituted and Pb,Al substituted compositions. The error is approximately 10%.

It is clear that the conductivity is not improved by substituting aluminum for titanium. It is assumed that the aluminum substitution creates oxygen vacancies within the perovskite block. It is speculated that the oxygen vacancies in the structure are not very mobile, therefore one cannot see the increase in conductivity associated with more vacancies.³⁷ It is possible that the conduction mechanism within the parent phase is polaron conduction associated with the titanium atoms, and oxygen vacancies are not very mobile in the structure.³⁷ If this is the case one would expect the conductivity to decrease as we remove titanium from the structure. This analysis is complicated by the simultaneous lead substitutions, where the decrease of conductivity due to lead substitutions was outlined in Section 3.4.5. The difference in the low temperature activation energy must also be noted, as the slope in this extrinsic region is triple what it is for the parent phase $\text{Bi}_2\text{Sr}_2\text{Nb}_2\text{TiO}_{12}$.

3.5 Controlled Atmosphere Conductivity

Controlled atmosphere conductivity was measured for several samples. The charge carriers for conduction are dependent on the external environment, therefore if the partial pressure of oxygen in the atmosphere is changed, the sample responds to reach equilibrium with the environment, which can affect the electrical properties. The typical response for a material under a reducing environment is shown in Equation 19. The other possibilities, assuming polaron conduction involving the three reducible cations used in Aurivillius materials are shown in Equation 20-22:



If the conductivity at a specific temperature is plotted against $\log(PO_2)$ this may provide information on the type of carrier from the slope. A slope of $-1/4$ is attributed to electronic conduction; and a slope of $-1/6$ indicates the oxygen vacancy concentration is changing as a function of PO_2 ; a slope of zero is typically attributed to ionic conduction.⁶⁶ The utility of such measurements were limited because only a small range of PO_2 was utilized. This is because it was previously determined the Aurivillius structure degrades at PO_2 of 10^{-3} atm at 1050°C , so the lowest PO_2 used was 0.005.

3.5.1 *Bi₂Sr₂Nb₂TiO₁₂*

A conductivity bar with a 0.13 cm^2 cross section and 1.65cm length was utilized for four point DC conductivity. The conductivity vs. temperature results for each atmosphere are shown in Figure 3.51.

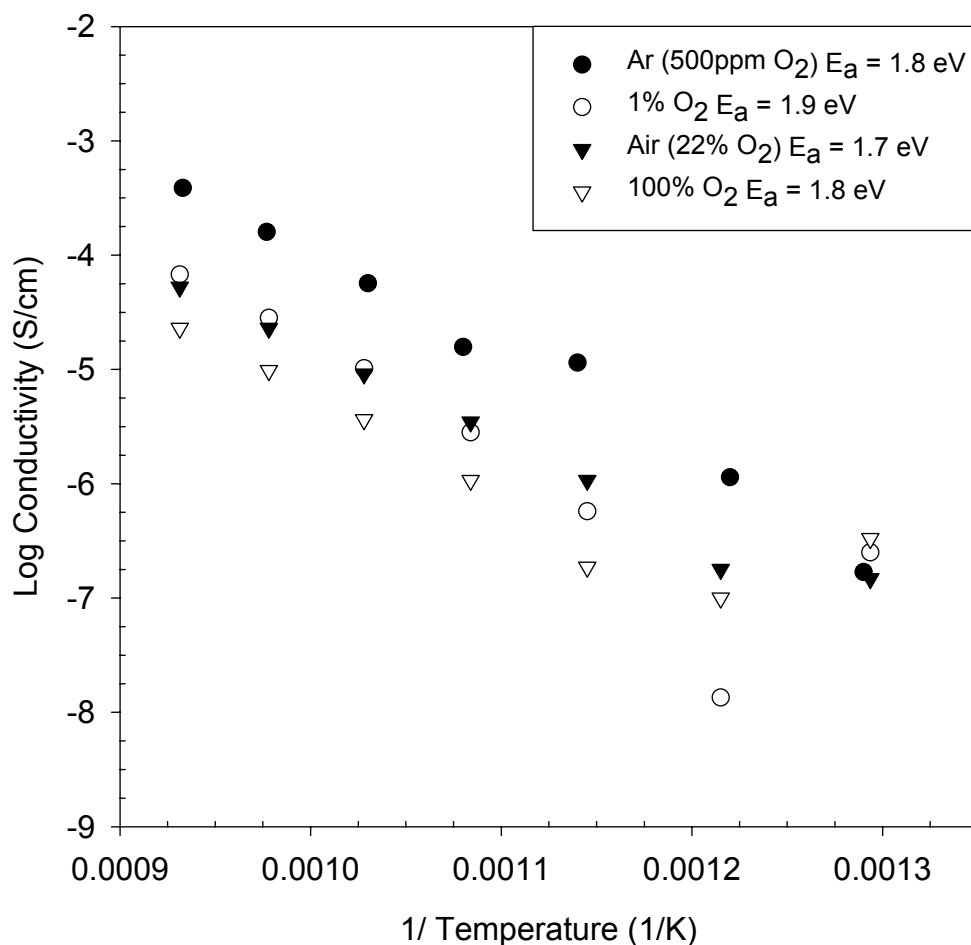


Figure 3.51. Controlled atmosphere 4-point DC conductivity of $\text{Bi}_2\text{Sr}_2\text{Nb}_2\text{TiO}_{12}$ up to 800°C . The open triangles are for oxygen atmosphere, the closed triangles are for air atmosphere, open circles are for 1% oxygen atmosphere, and closed circles are for argon atmosphere.

As is evident from Figure 3.51, the conductivity increases as the amount of oxygen in the environment decreases, an indication of electronic conductivity. Haluska stated that the mechanism for conduction in $\text{Bi}_2\text{Sr}_2\text{Nb}_2\text{TiO}_{12}$ is small polaron conduction between the titanium ions.³⁷ If this is the case, one would expect the conduction to increase as the oxygen is removed from the environment and more of the titanium ions reduce from 4^+ to 3^+ . The conductivity as a function of PO_2 is presented in Figure 3.52.

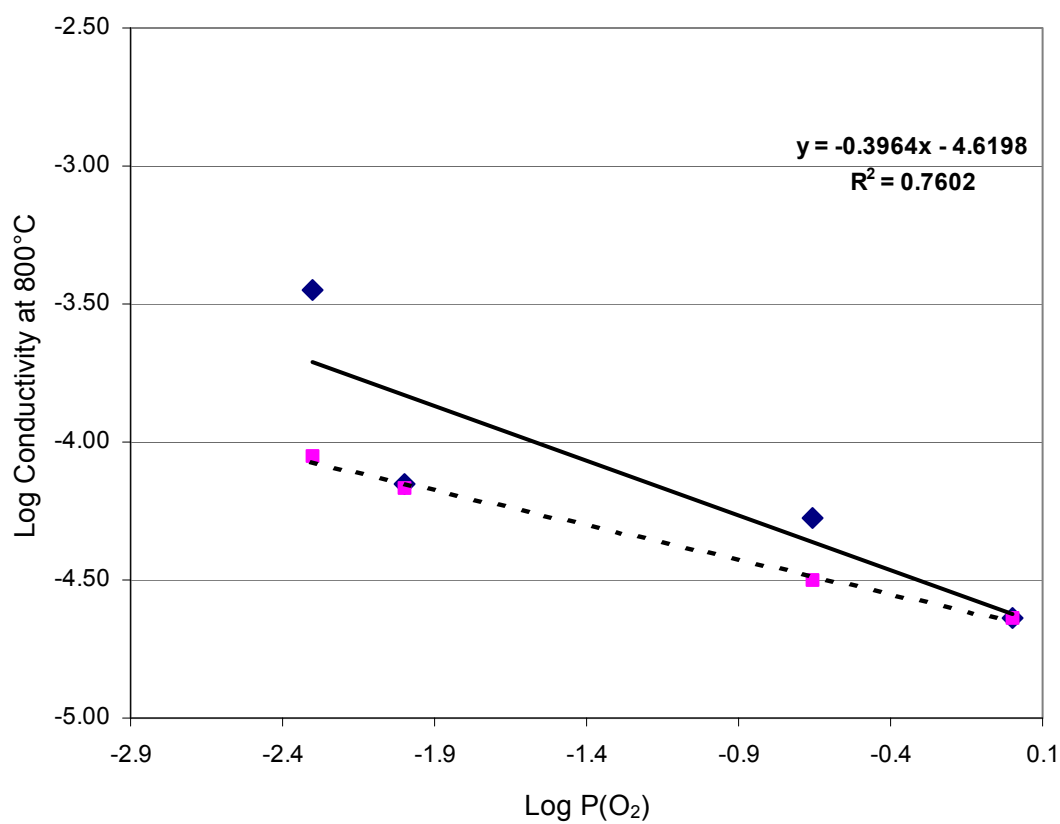


Figure 3.52. Log conductivity (measured using 4 point DC) vs. log PO₂ for Bi₂Sr₂Nb₂TiO₁₂ at 800°C. The dotted line and square data points represent a slope of $-1/4$.

As stated previously a slope of $-1/4$ in the log PO₂ vs. log conductivity plot correlates to electronic conductivity. However in this case a slope of -0.4 does not correlate well to this, this could be in part due to the relatively large amount of error between the measurements. The point for the Ar run (log PO₂ = -2.4) seems too high, making the linear trend line fit poorly. If this point is lowered or removed, the slope is very close to the expected $-1/4$. Although it may not be clear from Figure 3.52 it is speculated that the conduction in Bi₂Sr₂Nb₂TiO₁₂ is electronic, most likely a small polaron conduction mechanism involving the titanium or niobium ions.

An analogous study was conducted on the two-layer Aurivillius material Bi₂SrNb₂O₉ over a much wider PO₂ range.⁶⁷ The authors were able to use a wider PO₂ range because measurements were taken at lower temperatures ($\sim 700^\circ\text{C}$). The authors

found the material to be an electronic conductor for $-6 \leq \log P(\text{O}_2) \leq 0$, which overlaps the range studied here. They also hypothesized the mechanism of conduction to be polaron conduction of the niobium ions within the perovskite layer. This supports the speculation made earlier that the conduction mechanism in the $\text{Bi}_2\text{Sr}_2\text{Nb}_2\text{TiO}_{12}$ phase is electronic.⁶⁷

3.5.2 $\text{Bi}_2\text{Sr}_2\text{Nb}_2\text{Ti}_{0.8}\text{Fe}_{0.2}\text{O}_{12-\delta}$

A conductivity bar with approximately a 0.12 cm^2 cross section and 1.9 cm length was utilized for 4-point controlled atmosphere conductivity. The conductivity results for each atmosphere are shown below in Figure 3.53.

It is clear from Figure 3.53 that the conductivity does not change significantly as the PO_2 changes. This is further emphasized by the log conductivity vs PO_2 plot in Figure 3.54. Once again the slope does not correlate to the $-1/6$ or $-1/4$ conduction mechanism indicators. The slope in this case is close to zero, indicating little change in conductivity with atmospheric changes. Typically, this is an indication of ionic conductivity. Although this was not expected, it is entirely possible that if the iron substitutes into $\text{Bi}_2\text{Sr}_2\text{Nb}_2\text{Ti}_{0.8}\text{Fe}_{0.2}\text{O}_{12}$ as Fe^{3+} then the compensating defect could be an oxygen vacancy, not a hole. Therefore although only a small range of PO_2 was studied, the data indicates $\text{Bi}_2\text{Sr}_2\text{Nb}_2\text{Ti}_{0.8}\text{Fe}_{0.2}\text{O}_{12}$ is an ionic conductor.

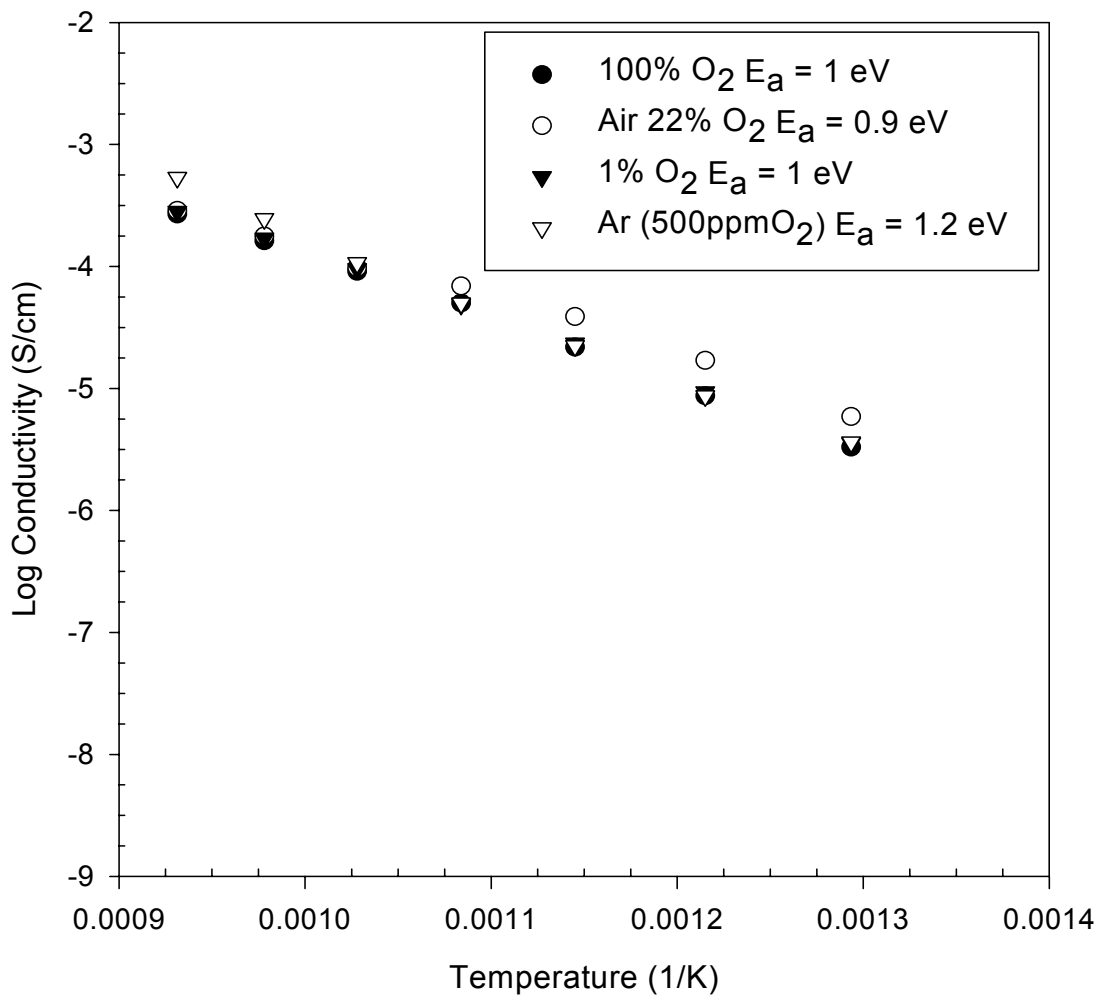


Figure 3.53. Controlled atmosphere conductivity of $\text{Bi}_2\text{Sr}_2\text{Nb}_2\text{Ti}_{0.8}\text{Fe}_{0.2}\text{O}_{12}$ up to 800°C . The closed circles are for oxygen atmosphere, the open circles are for air atmosphere, closed triangles are for 1% oxygen atmosphere, and closed diamonds are for argon atmosphere. All measurements from 4 point DC conductivity.

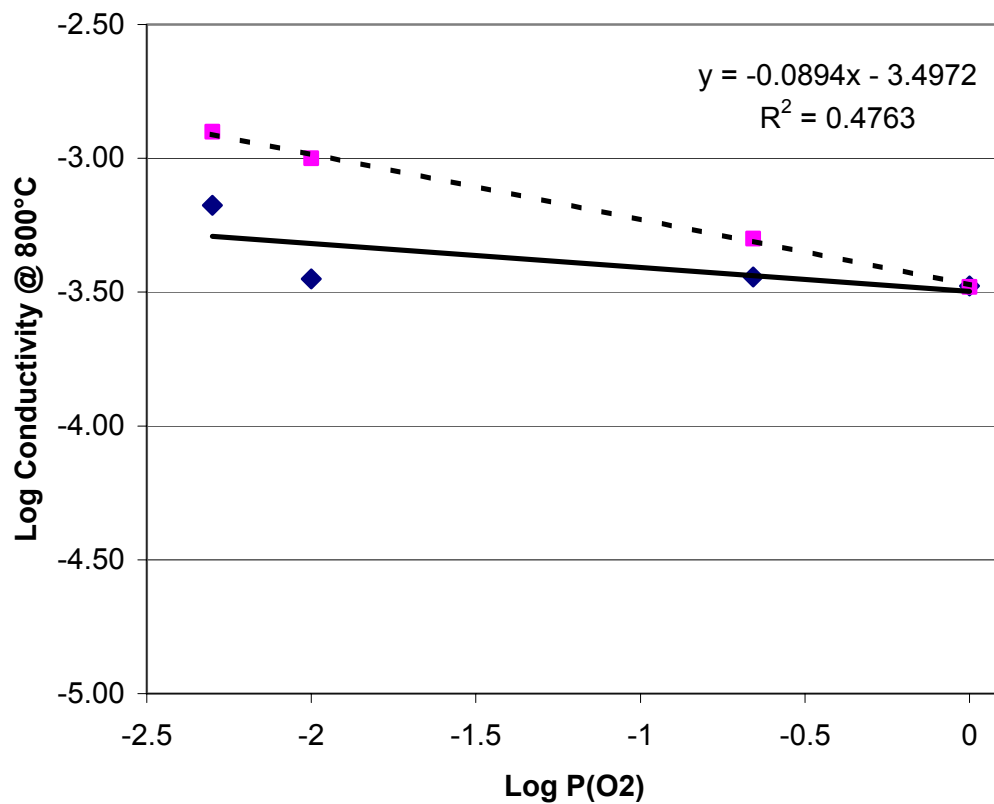


Figure 3.54. Log conductivity vs log PO₂ for Bi₂Sr₂Nb₂Ti_{0.8}Fe_{0.2}O₁₂ at 800°C measured using 4 point DC conductivity. The dotted line and square data points represent a slope of $-1/4$.

4 SUMMARY AND CONCLUSIONS

The polymerized complex method was successful in consistently producing homogeneous, phase pure powders in a shorter time than that required for solid-state synthesis. Therefore, it is considered that chemical synthesis is a reliable option of synthesis for this family of Aurivillius materials unless ease of process is the most important concern. The densities of the sintered samples were not high (50-70% theoretical), and high densities could not be achieved without the aid of hot pressing, which reached about 90% theoretical density. Hot pressed samples did not have improved electrical performance over non hot pressed samples.

Samples prepared with substitutions of transition metals (Fe, Cr, Co) for titanium in $\text{Bi}_2\text{Sr}_2\text{Nb}_2\text{TiO}_{12}$ achieved phase purity up to 50 atom% substitution. This was determined from the diffraction patterns and SEM analysis. The size of the transition metal substitutions is dependent upon the valence, and the phase purity trends seen in the series suggest that the transition metal substitutions enter the structure as isovalent substituents.

Two-point impedance spectroscopy was used to monitor the conductivity of the samples. The conductivity of all samples substituted with transition metals were identical within experimental error, and all were only slightly more conductive than the parent phase $\text{Bi}_2\text{Sr}_2\text{Nb}_2\text{TiO}_{12}$. This indicates two possible conclusions:

1. The charge carriers created could be of lower mobility than those inherent in the parent phase. The mobility could have been equal if the small change in conductivity was caused by a small increase in the number of carriers upon substitution.
2. The transition metal substitutions did not create charge carriers. This latter conclusion is supported by the synthesis trends, which suggest that the transition metals enter the structure in the 4^+ valence state, therefore resisting the formation of charge carriers.

Samples prepared substituting lead for bismuth in the parent phase $\text{Bi}_2\text{Sr}_2\text{Nb}_2\text{TiO}_{12}$ achieved phase purity up to 50 atom% lead substitution. At the level of $y=0.3$ in $\text{Bi}_{(2-y)}\text{Pb}_y\text{Sr}_2\text{Nb}_2\text{TiO}_{12}$, phase purity is assured. From $y=0$ to $y=1$, a broadening of all peaks with c-axis character (i.e. (hkl) (0,0,X) when $X \neq 0$) is observed. Also for the composition $\text{Bi}_{(2-y)}\text{Pb}_y\text{Sr}_2\text{Nb}_2\text{TiO}_{12}$ in the range $y=0.3-1$ the possibility of secondary bismuth oxide or lead oxide phase was noted, but not confirmed. The broadening of the XRD peaks with the series $\text{Bi}_{(2-y)}\text{Pb}_y\text{Sr}_2\text{Nb}_2\text{TiO}_{12-\delta}$ is isotropic, and therefore is not considered to be due to stacking faults. The crystallite size and crystallite strain effects cannot clearly be separated via traditional analysis of XRD peak widths. However, the particle shape after calcination of powder at 900°C for 10 hours suggests a crystallite size effect because of the thin, platy particles.

Substitutions of lead for bismuth in small amounts ($y=0.2$) increased the conductivity over the parent phase ($\text{Bi}_2\text{Sr}_2\text{Nb}_2\text{TiO}_{12}$) slightly; however at higher levels of substitution the conductivity noticeably decreased. This suggests two conclusions;

1. Conduction in the lead-substituted samples occurs in the bismuth oxide sheet. If the conductivity occurs in the bismuth oxide sheet, the conduction mechanism is most likely vacancies.
2. The decreased conductivity can be attributed to either low mobility vacancies being created by the substitution, or vacancy association at high levels of substitution, while a combination of the two likely occurs.

Attempts to determine the charge carrier in the parent phase $\text{Bi}_2\text{Sr}_2\text{Nb}_2\text{TiO}_{12}$, and the presumed electronic conductor, $\text{Bi}_2\text{Sr}_2\text{Nb}_2\text{Ti}_{0.8}\text{Fe}_{0.2}\text{O}_{12-\delta}$, were not successful. The limited range of PO_2 studied inhibited obtaining a definitive answer on the charge carrier. The data indicated that $\text{Bi}_2\text{Sr}_2\text{Nb}_2\text{TiO}_{12}$ is an electronic conductor, while $\text{Bi}_2\text{Sr}_2\text{Nb}_2\text{Ti}_{0.8}\text{Fe}_{0.2}\text{O}_{12}$ is an ionic conductor.

For the parent phase $\text{Bi}_2\text{Sr}_2\text{Nb}_2\text{TiO}_{12}$ the conductivity increased as the oxygen was removed from the atmosphere, an indication of electronic conduction. It has been suggested by others^{37,67} that the conduction mechanism in $\text{Bi}_2\text{Sr}_2\text{Nb}_2\text{TiO}_{12}$ is the small polaron mechanism, resulting from the reduction of niobium or titanium. For the

presumed electronic conductor $\text{Bi}_2\text{Sr}_2\text{Nb}_2\text{Ti}_{0.8}\text{Fe}_{0.2}\text{O}_{12}$ the conductivity did not change significantly over the PO_2 range studied.

5 FUTURE WORK

Controlled atmosphere conductivity measurements need to be performed over a much wider range of PO_2 (10^1 - 10^{-10} PO_2) at lower temperatures (500-600°C). This will provide some more conclusive information on what the charge carrier in the materials are. High resolution TEM should be conducted on samples within the lead substituted series in order to determine conclusively that it is indeed not a stacking fault problem that is causing the peak broadening, as well as to confirm the purity of the high lead substituted samples.

REFERENCES

1. T. Brylewski, M. Nanko, T. Maruyama, and K. Przybylski, "Application of Fe-16Cr Ferritic Alloy to Interconnector for a Solid Oxide Fuel Cell," *Solid State Ionics*, **143** [2] 131-50 (2001).
2. S.P.S. Badwal and K. Foger, "Solid Oxide Electrolyte Fuel Cell Review," *Ceram. Int.*, **22** [2] 257-65 (1995).
3. S.C. Singhal, "Advances in Solid Oxide Fuel Cell Technology," *Solid State Ionics*, **135** [1-4] 305-13 (2000).
4. B.C.H. Steele, "Materials for IT-SOFC Stacks: 35 Years R&D: The Inevitability of Gradualness," *Solid State Ionics*, **134** [1-2] 3-20 (2000).
5. N. Minh, "Ceramic Fuel Cells," *J. Am. Ceram. Soc.*, **76** [3] 563-88 (1993).
6. G. Petot-Ervas, C. Petot, D. Zientara, and J. Kusinski, "Microstructure and Transport Properties of Y-Substituted Zirconia and Gd-Substituted Ceria," *Mater. Chem. Phys.*, **81** [2-3] 305-7 (2003).
7. E. Wanzenberg, F. Tietz, D. Kek, P. Panjan, and D. Stover, "Influence of Electrode Contacts on Conductivity Measurements of Thin YSZ Electrolyte Films and The Impact on Solid Oxide Fuel Cells," *Solid State Ionics*, **164** [3-4] 121-9 (2003).
8. K.R. Kendall, C. Navas, J.K. Thomas, and H.-C. zur Loye, "Recent Developments in Perovskite-Based Oxide Ion Conductors," *Solid State Ionics*, **82** [3-4] 215-23 (1995).
9. K.R. Kendall, C. Navas, J.K. Thomas, and H.-C. zur Loye, "Recent Developments in Oxide Ion Conductors: Aurivillius Phases," *Chem. Mater.*, **8** [3] 642-9 (1996).
10. K.R. Kendall, J.K. Thomas, and H.-C. zur Loye, "Oxygen Ion Conductivity in a New Class of Layered Bismuth Oxides," *Solid State Ionics*, **70-71** [1] 221-4 (1994).
11. K.R. Kendall, J.K. Thomas, and H.-C. zur Loye, "Synthesis and Ionic Conductivity of a New Series of Modified Aurivillius Phases," *Chem. Mater.*, **7** [1] 50-7 (1995).
12. C. Miranda, M.E.V. Costa, M. Avdeev, A.L. Kholkin, and J.L. Baptista, "Relaxor Properties of Ba-Based Layered Perovskites," *J. Eur. Ceram. Soc.*, **21** [10-11] 1303-6 (2001).

13. L. Nibou, A. Aftati, M.E. Farissi, and J.-P. Mercurio, "Chemical Fabrication SrBi₄Ti₄O₁₅ Thin Films," *J. Eur. Ceram. Soc.*, **19** [6-7] 1383-6 (1999).
14. P.J. Klar and T. Rentschler, "Variation of the Soft Modes with Composition in the Raman Spectra of Charge-Compensated Series of n=2 and 3 Aurivillius Phases," *Solid State Commun.*, **103** [6] 341-5 (1997).
15. J.L. Pineda-Flores, E. Chavira, and A. Huanosta-Tera, "Ferroelectric Characteristics in Aurivillius Solid Solutions: Bi_{4-x}Ln_xTi₃O₁₂ (Ln=Gd, Dy), 0x<0.8," *Phys.C. (Amsterdam, Neth.)*, **364-365** 674-7 (2001).
16. C.O. Paiva-Santos, T. Mazon, M.A. Zaghete, A.L. Campos, J.A. Varela, and C.R. Foschini, "Crystal Structure of BaBi₂Ta₂O₉," *Powder Diffraction*, **15** [2] 134-8 (2000).
17. C.H. Hervoches, A. Snedden, R. Riggs, S.H. Kilcoyne, P. Manuel, and P. Lightfoot, "Structural Behavior of the Four-Layer Aurivillius-Phase Ferroelectrics SrBi₄Ti₄O₁₅ and Bi₅Ti₃FeO₁₅," *J. Solid State Chem.*, **166** [2] 449 (2002).
18. D. Xie and W. Pan, "Study on BaBi₄Ti₄O₁₅ Nanoscaled Powders Prepared by Sol-Gel Method," *Mater. Lett.*, (in press).
19. P. Boullay, G. Trolliard, D. Mercurio, J.M. Perez-Mato, and L. Elcoro, "Toward a Unified Approach to the Crystal Chemistry of Aurivillius-Type Compounds: I. The Structural Model," *J. Solid State Chem.*, **164** [2] 252-60 (2002).
20. P. Boullay, G. Trolliard, D. Mercurio, J.M. Perez-Mato, and L. Elcoro, "Toward a Unified Approach to the Crystal Chemistry of Aurivillius-Type Compounds: II. Bi₇Ti₄NbO₂₁, a Case Study," *J. Solid State Chem.*, **164** [2] 261-71 (2002).
21. F.E. Longoria Rodriguez and A. Martinez-de la Cruz, "Electrochemical Study of the Reaction of Lithium with Aurivillius and Related Phases," *Mater. Res. Bull.*, **36** [7-8] 1195-204 (2001).
22. C. Pirovano, M.S. Islam, R.-N. Vannier, G. Nowogrocki, and G. Mairesse, "Modelling the Crystal Structures of Aurivillius Phases," *Solid State Ionics*, **140** [1-2] 115-23 (2001).
23. S. Borg, G. Svensson, and J.-O. Bovin, "Structure Study of Bi_{2.5}Na_{0.5}Ta₂O₉ and Bi_{2.5}Na_{m-1.5}Nb_mO_{3m+3} (m=2-4) by Neutron Powder Diffraction and Electron Microscopy," *J. Solid State Chem.*, **167** [1] 86-96 (2002).
24. N. Yasuda, M. Miyayama, and T. Kudo, "Oxide Ion Conductivity of Bismuth Layer-Structured Bi₂K_(1-x)Nb₂O_(8.5-delta)," *Solid State Ionics*, **133** [3-4] 273-8 (2000).

25. T. Rentschler, "Substitution of Lead into the Bismuth Oxide Layers of the n=2 and n=3 Aurivillius Phases," *Mater. Res. Bull.*, **32** [3] 351-69 (1997).
26. M.T. Montero, P. Millan, P. Duran-Martin, B. Jimenez, and A. Castro, "Solid Solutions of Lead-Substituted Bismuth Oxide Layer of Aurivillius n=2 and n=3 Oxides: Structural and Dielectric Characterization," *Mater. Res. Bull.*, **33** [7] 1103-15 (1998).
27. S.A. Speakman, "The Crystal Chemistry of Brownmillerite and n=3 Aurivillius Type Ceramic Conductors for Fuel Cell Applications"; Ph.D. Thesis, Alfred University, Alfred, NY, 2002.
28. B. Aurivillius, "Mixed Bismuth Oxides with Layer Lattices: I. The Structure Type of $\text{CaNb}_2\text{Bi}_2\text{O}_9$," *Ark. Kemi*, **1** [54] 463-80 (1949).
29. B. Aurivillius, "Mixed Bismuth Oxides with Layer Lattices: II. Structure of $\text{Bi}_4\text{Ti}_3\text{O}_{12}$," *Ark. Kemi*, **1** [58] 499-512 (1949).
30. B. Aurivillius, "Mixed Oxides with Layer Lattices: III. Structure of $\text{BaBi}_4\text{Ti}_4\text{O}_{15}$," *Ark. Kemi*, **2** [37] 519-27 (1950).
31. P. Lightfoot, A. Snedden, and S.M. Blake, "Oxide Ion Conductivity in Ga-Substituted Aurivillious Phases -- A Reappraisal," *Solid State Ionics*, **156** [3-4] 439-45 (2003).
32. N.M. Sammes, G.A. Tompsett, H. Nafe, and F. Aldinger, "Bismuth Based Oxide Electrolytes - Structure and Ionic Conductivity," *J. Eur. Ceram. Soc.*, **19** [10] 1801-26 (1999).
33. T. Takahashi, H. Iwahara, and T. Esaka, "High Oxide Ion Conduction in Sintered Oxide of the System $\text{Bi}_2\text{O}_3\text{-M}_2\text{O}_5$," *J. Electrochem. Soc.*, **124** [7] 1563-9 (1977).
34. T. Takahashi and H. Iwahara, "Oxide Ion Conductivity of Bismuthsesquioxide," *Mater. Res. Bull.*, **13** [12] 1447-53 (1978).
35. C. Say, "Electrical and Compositional Study of n=3 Aurivillius Structures for Oxygen Conducting Devices"; M.S. Thesis, Alfred University, Alfred, NY, 2002.
36. V.B. Modi, "Electrical and Microstructural Characterization of n=3 Type Aurivillius Phases"; M.S. Thesis, Alfred University, Alfred, NY, 2002.
37. M.S. Haluska, "Synthesis and Structural Characterization of Aurivillius Ceramics"; Ph. D. Thesis, Alfred University, Alfred, NY, 2003.
38. J.R. Macdonald, *Impedance Spectroscopy: Emphasizing Solid Materials and Systems*; pp. 2-25. John Wiley & Sons, New York, 1987.

39. G. Hsieh, S.J. Ford, T.O. Mason, and L.R. Pederson, "Experimental Limitations in Impedance Spectroscopy: Part VI. Four-Point Measurements of Solid Materials Systems," *Solid State Ionics*, **100** [3-4] 297-311 (1997).
40. D.D. Edwards, J.H. Hwang, S.J. Ford, and T.O. Mason, "Experimental Limitations in Impedance Spectroscopy: Part V Apparatus Contributions and Corrections," *Solid State Ionics*, **99** [1-2] 85-93 (1997).
41. A.R. West, D.C. Sinclair, and N. Hirose, "Characterization of Electrical Materials, Especially Ferroelectrics, by Impedance Spectroscopy," *J. Electroceram.*, **1** [1] 65-71 (1997).
42. D.C. Sinclair and A.R. West, "Impedance Spectroscopy of Semiconducting BaTiO₃ Showing Positive Temperature Coefficient of Resistance," *J. Appl. Phys.*, **66** [8] 3850-6 (1989).
43. N. Hirose and A.R. West, "Impedance Spectroscopy of Unsubstituted BaTiO₃ Ceramics," *J. Am. Ceram. Soc.*, **79** [6] 1633-41 (1996).
44. J.-H. Hwang, K.S. Kirkpatrick, T.O. Mason, and E.J. Garboczi, "Experimental Limitations in Impedance Spectroscopy: Part IV. Electrode Contact Effects," *Solid State Ionics*, **98** [1-2] 93-104 (1997).
45. T.A. Ramanarayanan, S.C. Singhal, and E.D. Wachsman, "High Temperature Ion Conducting Ceramics," *Electrochem. Soc. Interface*, **10** [2] 22-7 (2001).
46. B.S. Luisi, "Chemical Synthesis and Characterization of 3-Layer Bi_(2-y)Pb_ySr₂Nb₂Ti_(1-x)Al_xO_{12-d} Aurivillius Ionic Conductors and LaSrO₃ Cathode Ceramics"; M.S. Thesis, Alfred University, Alfred, NY, 2003.
47. H.U. Anderson, "Polymeric Synthesis of Lead Magnesium Niobate Powders," *Adv. Ceram.*, **21** [1] 91-8 (1987).
48. A. Hardy, K. Van Werde, G. Vanhoyland, M.K. Van Bael, J. Mullens, and L.C. Van Poucke, "Study of the Decomposition of an Aqueous Metal-Chelate Gel Precursor for (Bi,La)₄Ti₃O₁₂ by Means of TGA-FTIR, TGA-MS and HT-DRIFT," *Thermochim. Acta*, **397** [1-2] 143-53 (2003).
49. Dr. Scott Mixture, Alfred University, October, 2003, Private Communication.
50. R.D. Shannon, "Revised Effective Ionic Radii and Systematic Studies of Interatomic Distances in Halides and Chalcogenides," *Acta Crystallogr.*, **A32** [5] 751-67 (1976).
51. W.J. Yu, Y.I. Kim, D.H. Ha, J.H. Lee, Y.K. Park, S. Seong, and N.H. Hur, "A New Manganese Oxide with the Aurivillius Structure: Bi₂Sr₂Nb₂Mn_(12-delta)," *Solid State Ionics*, **111** [12, 14] 705-9 (1999).

52. H.-F. Yu and K.-C. Huang, "Preparation and Characterization of Ester-Derived BaFe₁₂O₁₉ Powder," *J. Mater. Res.*, **17** [1] 199-203 (2001).
53. K. Yoshimura, "Synthesis and Characteristics of Complex Multicomponent Oxides Prepared by Polymerized Complex Method," *Bull. Chem. Soc. Jpn.*, **172** [7] 1427-43 (1999).
54. . "Standard Test Methods for Apparent Porosity, Water Absorption, Apparent Specific Gravity, and Bulk Density of Burned Refractory brick and Shapes by Boiling Water," ASTM Designation C 20-97. American Society for Testing and Materials, West Conshohocken, PA.
55. W. Kruase and G. Nolze, Powdercell 2.4 [Computer Program]. Federal Institute for Materials Research and Testing, Berlin, Germany, 2000.
56. Zview 3.0 [Computer Program]. Scribner Associates, Southern Pines, NC, 1999.
57. M. Peterson, "Synthesis Optimization of Aurivillius Phases"; M.S. Thesis, Alfred University, Alfred, NY, 2003.
58. W. Dmowski, M.K. Akbas, P.K. Davies, and T. Egami, "Local Structure of Pb(Sc_{1/2},Ta_{1/2})O₃ and Related Compounds," *J. Phys. Chem. Solids*, **61** [2] 229-37 (2000).
59. Y. Ding, J.S. Liu, J.S. ZHU, and Y.N. Wang, "Stacking Faults and Their Effects on Ferroelectric Properties in Strontium Bismuth Tantalate," *J. Appl. Phys.*, **91** [4] 2255-61 (2002).
60. D.C. Yoo, J.Y. Lee, I.S. Kim, and Y.T. Kim, "Nucleation and Grain Growth of SrBi₂Nb₂O₉ Thin Films," *J. Cryst. Growth*, **259** [1-2] 79-84 (2003).
61. A. Boule, C. Legrand, P. Thomas, R. Guinebretiere, J.P. Mercurio, and A. Dager, "Stacking Disorder in Aurivillius Compounds Studied by X-Ray Diffraction Line Profile Analysis," *Mater. Sci. Forum*, **378-391** [1] 753-8 (2001).
62. R. Jenkins and R.L. Snyder, Monographs on Analytical Chemistry and Its Applications, Vol. 138, *Introduction to X-ray Powder Diffractometry*. John Wiley and Sons, New York, 1996.
63. S.M. Blake, M.J. Falconer, M. McCreedy, and P. Lightfoot, "Cation Disorder in Ferroelectric Aurivillius Phases of the Type Bi₂ANb₂O₉ (A=Ba, Sr, Ca)," *J. Mater. Chem.*, **7** [8] 1609-13 (1997).
64. Ismunandar, B.A. Hunter, and B.J. Kennedy, "Cation Disorder in the Ferroelectric Aurivillius Phase PbBi₂Nb₂O₉: An Anomalous Dispersion X-ray Diffraction Study," *Solid State Ionics*, **112** [3-4] 281-9 (1998).

65. C.H. Hervoches and P. Lightfoot, "Cation Disorder in Three-Layer Aurivillius Phases: Structural Studies of $\text{Bi}_{(2-x)}\text{Sr}_{(2+x)}\text{Ti}_{(1-x)}\text{Nb}_{(2+x)}\text{O}_{12}$ ($0 < x < 0.8$) and $\text{Bi}_{(4-x)}\text{La}_{(x)}\text{Ti}_3\text{O}_{12}$ ($x=1$ and 2)," *J. Solid State Chem.*, **153** [1] 66-73 (2000).
66. N.M. Tallan, *Electrical Conductivity in Ceramics and Glass (Part A)*; Ch. 4. Marcel Dekker, New York, 1974.
67. C.A. Palanduz and D.M. Smyth, "The Effect of Cation Place Exchange on The Electrical Conductivity of $\text{SrBi}_2\text{M}_2\text{O}_9$ ($\text{M}=\text{Ta}, \text{Nb}$)," *J. Eur. Ceram. Soc.*, **19** [6-7] 731-5 (1999).

APPENDIX

TEM was utilized to investigate the lead composition $\text{BiPbSr}_2\text{Nb}_2\text{TiO}_{12-\delta}$, to add to the explanation of the lead series $\text{Bi}_{(2-x)}\text{Pb}_x\text{Sr}_2\text{Nb}_2\text{TiO}_{12-\delta}$ ($x=0-1$) and the observed anomalous diffraction behavior presented in Section 3.4.2. A sample of calcined powder ($900^\circ\text{C}/10\text{hrs}$) was ground in an alumina mortar and pestle and placed in a bottle of acetone. The acetone bottle was then placed in an ultrasonic cleaner for one minute to disperse particles into suspension, into which a copper grid was dipped. The TEM at Alfred University was utilized at an acceleration voltage of 200kV and a current of 130 microamps.

The TEM investigation yielded much more credibility to the crystallite size argument. Almost all particles seen were square-like in nature (and very thin), and yet unlike the SEM images obtained, the size was on the order of the lattice parameters. Some of the particles appeared needle-like, which could be attributed to the long c-axis of the Aurivillius structure. However, if the sample stage was rotated, it was revealed time and again that this was merely a square particle that was tilted so it appeared needle-like. This is observed in Figure 5.1

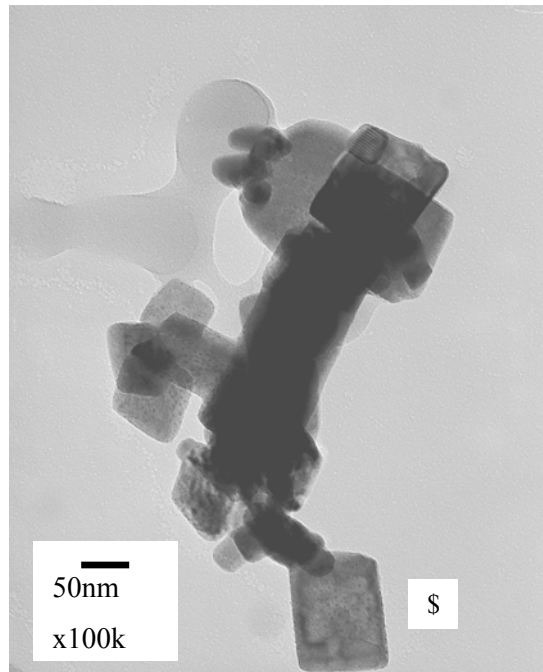


Figure 5.1. TEM image of $\text{BiPbSr}_2\text{Nb}_2\text{TiO}_{12-\delta}$ calcined powder. The EDS spectrum of the particle marked with the \$ sign is presented in Figure 5.2. The clear material is the membrane coating.

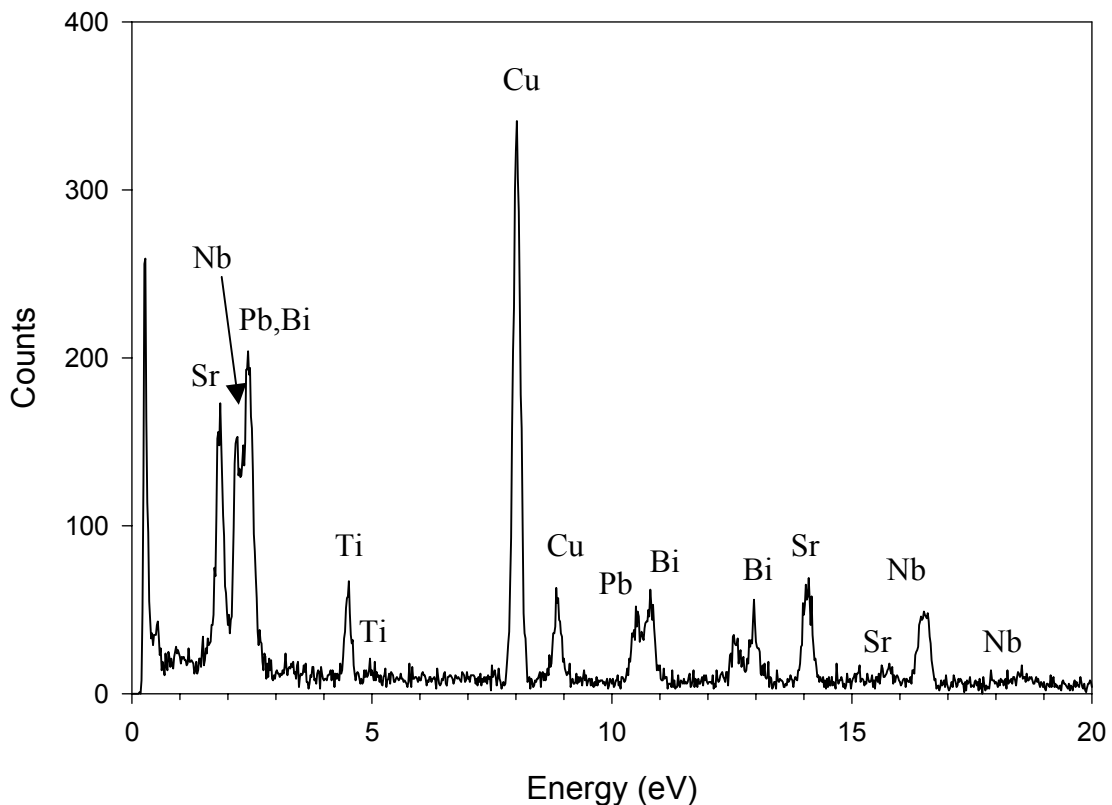


Figure 5.2. EDS spectrum of particle indicated in Figure 5.1 with the dollar sign. All of the constituents are present, and copper is present from the TEM grid supporting the particles.

The thickness of the particle “platelets” also added more credibility to the crystallite size broadening argument. It appears that the crystals are very platy in nature, as they are only about 10-20nm thick and several-hundred nm wide. As was previously noted, this broadening is minimized after sintering, where at the high times and temperatures the longer c-axis would have more time to grow in the crystals. This is strongly indicated by the images presented in Figure 5.3. The diffraction pattern in B appears generally like a cubic pattern, as the lattice points are all spaced the same amount, an indication the crystals are oriented parallel to the c-axis of the unit cell.

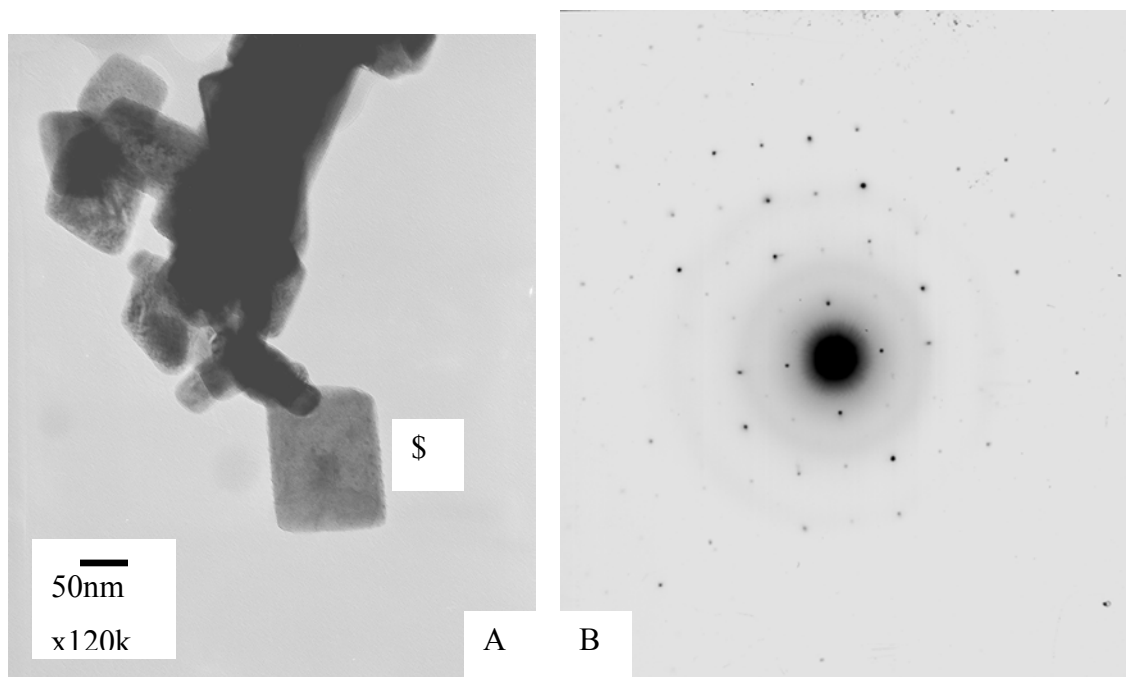


Figure 5.3 TEM images of $\text{BiPbSr}_2\text{Nb}_2\text{TiO}_{12-\delta}$ A) bright field image at x120k, and B) is the diffraction pattern for the particle marked with the \$ sign in A.

The second possible explanation to the observed diffraction effects that was given support via TEM analysis is compositional inhomogenities on a unit cell to unit cell scale. If the lead substitutions are not evenly dispersed through the entire bulk sample, several crystals of the sample might have more of the lead substitutions than another. This would correlate to differences in the lattice parameters (because lead is a larger ion than bismuth) and result in broadened peaks. One of the diffraction patterns observed in the TEM analysis was an indication of this. This pattern was for multiple crystals, and several of the dots had other “surrounding dots” of very similar spacing. This is not a typical observation and is a direct indication that the crystals all had slightly different lattice parameters, likely from different amounts of the lead substitution.

This observation is further supported by the images seen in Figure 5.4 and Figure 5.5. The EDS spectra of the two grains appear to be the same upon first glance; however, upon closer inspection the ratios of the lead and bismuth peaks is different for the two grains. This supports the idea of chemical inhomogenities on a very small scale. If the lead and bismuth ratio varied from grain to grain, one would see a

diffraction pattern without very clear d-spacings for different planes, as was observed and described previously.

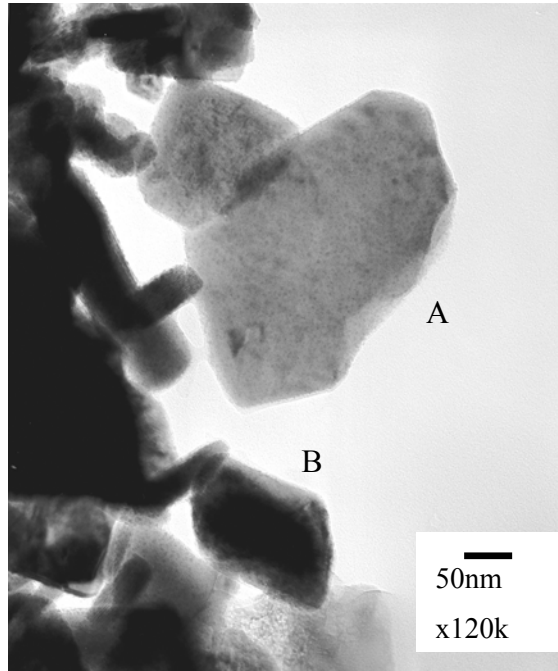


Figure 5.4. TEM image of TEM image of $\text{BiPbSr}_2\text{Nb}_2\text{TiO}_{12-\delta}$ calcined powder, the grains A and B are identified for the EDS analysis presented in Figure 5.4.

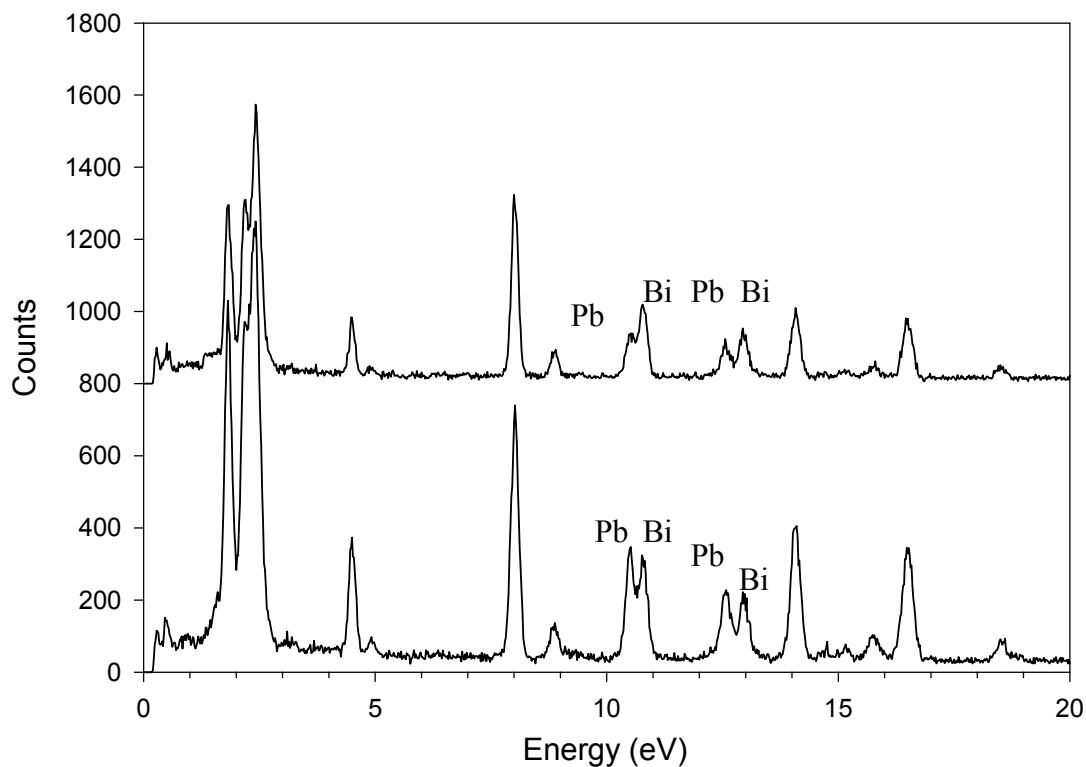


Figure 5.5. EDS spectra of $\text{BiPbSr}_2\text{Nb}_2\text{TiO}_{12-\delta}$ shown in Figure 5.4. The bottom pattern is from grain marked A in Figure 5.4 and the top pattern is for grain marked B in Figure 5.4. Notice slightly different lead to bismuth ratios for the grains.

In conclusion, the TEM analysis was not successful in identifying any clear bismuth oxide impurity phases, the possibility of which was outlined in Section 3.4.3. The crystals showed platelet-like nature, which is further indication that the anomalous diffraction patterns of the lead series could be linked to a crystallite size effect. Also the possibility of small scale compositional inhomogenities was noted.